DEPARTMENT OF PHYSICS
UNIVERSITY OF JYVÄSKYLÄ
RESEARCH REPORT No. 4/2012

MANY-PARTICLE THEORY FOR TIME-DEPENDENT QUANTUM TRANSPORT IN NANOSTRUCTURES

BY
PETRI MYÖHÄNEN

Academic Dissertation
for the Degree of
Doctor of Philosophy

To be presented, by permission of the
Faculty of Mathematics and Natural Sciences
of the University of Jyväskylä,
for public examination in Auditorium FYS-1 of the
University of Jyväskylä on June 8th, 2012
at 12 o'clock noon

Jyväskylä, Finland
June 2012

Preface

The work of this thesis was carried out at the Department of Physics and Nanoscience Center in the University of Jyväskylä during the years 2007 and 2012.

First of all, I want to thank my supervisor, professor Robert van Leeuwen for his patient steering and help throughout my doctoral studies and research work. I also wish to address my gratitude for all the wonderful people with whom I have spend time and worked with during these years. I wish to thank our close collaborator Gianluca Stefanucci for his positive feedback, dedication and careful revisioning of our research articles and Vesa Apaja for his competent technical support and seamless teamwork during the programming courses. I also wish to thank Jenni Andersin, Thomas Kühn, Anna-Maija Uimonen, Adrian Stan, Esa Räsänen, Niko Säkkinen, Riitta-Liisa Kuittinen, Tahnie Barboza, Claudia Rocha, Klaas Giezberts, Michael Ruggenthaler, Topi Korhonen, Riku Tuovinen, Tero Isotalo, Oleg Kit, Olga Lopez-Acevedo, Xi Chen and Lauri Lehtovaara with whom I have had many interesting conversations and very cheerful moments during the years. I am also grateful for Eero Hulkko, Lauri Nykänen, Ville Kotimäki and the group leaders Hannu Häkkinen, Matti Manninen, Karoliina Honkala, Pekka Koskinen and Ilari Maasilta for our random casual discussions.

I want to show a special gratitude to my family, relatives and friends who have encouraged me and helped me to keep in mind the important things of life. Finally, I thank my beloved fiancé Marja for her endless love, patience and understanding.

Jyväskylä, May 2012

Petri Myöhänen

Abstract

During the recent decades, molecular electronics has established its place as one of the promising fields in the nanoscience. The possibility to manufacture and control molecular junctions where single molecules are squeezed between the conducing electrodes has opened up new possibilities to develop nanoscale devices which could be employed as building blocks for future nanoelectronic applications. The driving force for this new branch of physics has been the experimental advances but also theoretical methods have been under intensive study and many theoretical tools have been developed to understand the electron transport processes in the nanoscale systems. This thesis focuses on developing a formalism that helps to understand the role of electron-electron interactions and the physical principles behind the time-dependent electron transport in such systems.

The formalism presented in this thesis is based on the theory of non-equilibrium Green functions (NEGF) and, more specifically on the real-time propagation of the embedded Kadanoff-Baym (KB) equations which are quantum-kinetic equations for the one-particle propagator. This formalism allows for studying ultrafast dynamical processes with femtosecond (fs) time resolution and have several advantages compared to other methods. The Kadanoff-Baym formalism can be applied to both open and closed systems. It allows for non-perturbative treatment of the external driving fields, suitable preparation of the initial state, inclusion of the initial correlation effect during time-propagation and, in addition, can deal with the electronic interactions via self-energy terms which guarantee that the conservation laws are obeyed. All these properties are vital for treating open and correlated systems associated to the physical phenomena such as electron transport.

In this thesis, we apply the Kadanoff-Baym formalism to study time-dependent non-equilibrium processes of simple correlated molecular-like systems connected to electron reservoirs. We have found that the electron-electron interactions can have a major impact on the time-dependent and steady-state transport properties as well as on the spectral properties of the molecular device. The Coulomb interactions, when restricted to the scattering region only, can lead to a significant renormalization of the molecular gap in non-equilibrium conditions and can change the transient current flow considerably. Furthermore, the electronic self-energies, when treated on different levels of sophistication, can lead to very different temporal properties especially under the resonance conditions. As one of the essential results, we have also found that the initial correlation effects and initial state dependence, when accounted properly, can influence considerably on the transient dynamics.

As one of the other main topics regarding the time-dependent transport, we also investigated the role of the Coulomb interactions between the molecular scattering region and the electron reservoirs. Our findings suggest that these interactions can have big impact on the dynamics of the molecular junction when driven out of equilibrium with a bias

voltage. We found that the Coulomb interactions between the subsystems can also lead to strong renormalization of the resonances and change the transient and steady-state properties dramatically. In the mean-field level, however, the treatment of these lead interactions can give rise to current blockade and undamped post-transient dynamics where the system does not relax towards a steady-state. These peculiar effects can be cured with inclusion of the electron correlations which provide substantial damping to the transients and account for the important image-charge effects via polarization diagrams. Our results show that the lead interactions in general and the image charge effect can modify the current–voltage characteristics prominently and that these interactions can restrain the bias dependent quasiparticle broadening under non-equilibrium conditions.

Author's address Petri Myöhänen
Department of Physics
University of Jyväskylä
Finland

Supervisors Professor Robert van Leeuwen
Department of Physics
University of Jyväskylä
Finland

Reviewers Associate Professor Kristian Thygesen
Center for Atomic-scale Materials Design (CAMD)
Department of Physics
Technical University of Denmark
Denmark

Professor Antti-Pekka Jauho
Department of Micro- and Nanotechnology
Technical University of Denmark
Denmark

Opponent Associate Professor Claudio Verdozzi
Department of Physics
University of Lund
Sweden

List of Publications

I P. Myöhänen, A. Stan, G. Stefanucci and R. van Leeuwen, *A many-body approach to quantum transport dynamics: Initial correlations and memory effects* EuroPhysics Letters **84** 67001 (2008)[1]

II P. Myöhänen, A. Stan, G. Stefanucci and R. van Leeuwen, *Kadanoff-Baym approach to quantum transport through interacting nanoscale systems: From the transient to the steady-state regime* Phys. Rev. B **80**, 115107 (2009) [2]

III P. Myöhänen, T. Korhonen, R. Tuovinen, G. Stefanucci and R. van Leeuwen, *Image charge dynamics in time-dependent quantum transport* Phys. Rev. B **85** 075105 (2012) [3]

IV P. Myöhänen, A. Stan, G. Stefanucci and R. van Leeuwen, *Kadanoff-Baym approach to time-dependent quantum transport in AC and DC fields* J. Phys.: Conf. Ser. **220** 012017 (2010) [4]

The author has done all of the numerical calculations and written the first drafts of articles **I**, **II**, **III** and **IV**. He has implemented the transport part and lead density part of the Kadanoff-Baym code to enable the study of transport phenomena in open and interacting systems within the Kadanoff-Baym approach. The numerical method has then been applied in the publications **I**, **II**, **III** and **IV**.

Contents

Notation

In this thesis all the matrix and vector symbols are written in boldface notation. Furthermore, all the essential, important and new concepts are introduced with *emphasized* style.

List of frequently used symbols

General symbols

$\hat{H}$	Hamiltonian operator
$\sigma = \uparrow, \downarrow$	Spin quantum number
$\mathbf{x} \equiv (\mathbf{r}, \sigma)$	Position-spin Coordinate
$1 \equiv (\mathbf{x}_1 z_1)$	Position-spin-time coordinate
Z_k	(Effective) Charge of a nucleus k
$\delta(x)$, $\delta(x,y)$, δ_{ij}	Delta functions
$\theta(x)$, $\theta(x,y)$	Step functions
z	General time-index on the Keldysh contour
t	Time-index on the real time track of the Keldysh contour
τ	Time-index on the imaginary time track of the Keldysh contour
$\hat{U}(z_2, z_1)$	(Contour) Time-evolution operator
$\hat{A}_H(1)$	Heisenberg picture representation of operator $\hat{A}$: $\hat{A}_H(1) = \hat{U}(t_0, t_1)\hat{A}(\mathbf{x}_1)\hat{U}(t_1, t_0)$
$\mathscr{T}_C[\cdots]$	(Contour) Time-ordering operator
$\beta = \frac{1}{k_B T}$	Inverse temperature (with k_B the Boltzmann constant)
μ	Chemical potential
$\hat{\rho} = \frac{1}{\mathscr{Z}} e^{-\beta(\hat{H} - \mu\hat{N})}$	Grand canonical density operator
$\langle \hat{O} \rangle$	Expectation value of operator $\hat{O}$
$f(\epsilon) = \frac{1}{e^{\beta(\epsilon-\mu)}+1}$	Fermi-Dirac distribution function

Many-Particle theory

$\hat{\psi}^\dagger(\mathbf{x})$	Creation operator in position-spin representation
$\hat{\psi}(\mathbf{x})$	Annihilation operator in position-spin representation
$h(1)$	One-body part of the Hamiltonian
$w(1,2)$	Interparticle interaction
$\hat{n}(\mathbf{x}) = \hat{\psi}^\dagger(\mathbf{x})\hat{\psi}(\mathbf{x})$	Density operator in position-spin representation

$G(1,2)$	Interacting one-particle Green function
$F^{\lessgtr,\rceil,\lceil,R,A,M}$	Lesser ($<$), Greater ($>$), Mixed ($\rceil$, $\lceil$), Retarded (R), Advanced (A) and Matsubara (M) projections of F on Keldysh contour
$g_{(0)}(1,2)$	Noninteracting one-particle Green function
$A(\omega)$	Spectral function
$G_2(1,2;2',1')$	Two-particle Green function
$\Sigma^{\mathrm{MB}}(1,2)$	Many-Body self-energy
$\Sigma_{\mathrm{xc}}(1,2)$	Exchange-correlation part of the many-body self-energy
$P(1,2)$	Polarization function
$W(1,2)$	Screened interaction
$\Lambda(1)$	Gauge function
$\Phi[G]$	Gauge invariant generating functional for the self-energy

Transport theory

$\varphi_{k\bar{\sigma}}(\mathbf{r}\sigma)$	Spin orbital at site k with spin-projection $\bar{\sigma}$, $\varphi_{k\bar{\sigma}}(\mathbf{r}\sigma) = \langle \mathbf{r}\sigma \vert k\bar{\sigma}\rangle = \delta_{\sigma\bar{\sigma}}\varphi_k(\mathbf{r})$
$\hat{c}^\dagger_{i\sigma}$, $\hat{a}^\dagger_{i\sigma}$, $\hat{d}^\dagger_{i\sigma}$	Creation operators in basis representation
$\hat{c}_{i\sigma}$, $\hat{a}_{i\sigma}$, $\hat{d}_{i\sigma}$	Annihilation operators in basis representation
$\hat{n}_{i\sigma} = \hat{c}^\dagger_{i\sigma}\hat{c}_{i\sigma}$	Density operator in lattice representation
$\mathbf{\Sigma}_{\mathrm{em}}$	Embedding self-energy
$\mathbf{\Sigma}_{\mathrm{in}}$	Inbedding self-energy
$\mathbf{\Gamma}_\alpha(\omega)$	Linewidth function for lead α
$\mathbf{\Lambda}_\alpha(\omega)$	Hilbert transform of the linewidth function
$\mathbf{h}_{C\alpha}, V_{i,k\alpha}$	Coupling matrix elements between central region (i) and lead α (k)
$W^\alpha(t)$	Bias voltage for terminal α
$f_\alpha(\omega) = f(\omega + W^\alpha)$	Biased Fermi-Dirac distribution function
R_α	Number of rows in the terminal α
$I_\alpha(t)$	Time-dependent current for the terminal α
a_α	On-site potential term for lead α
b^λ_α	Longitudinal hopping term for lead α
b^τ_α	Transverse hopping term for lead α
$w_{ii} = U_0$	Hubbard interaction term
w_{ij}	Off-diagonal interaction terms

1 Introduction

About 50 years has already passed since one of the path-breaking physicist of our time, Richard P. Feynman, gave his classic talk at the annual meeting of American Physical Society. His talk, entitled "There's plenty of room at the bottom" [5], crystallized new ideas which had been around in the physics community for a while, namely the visions of manufacturing and controlling nanometer-scale devices which could be utilized in broad range of science and in several technological applications. The idea of possibility of improving the resolution of imaging devices and minituarizing the electrical circuits until the inevitable limit, namely the size of an atom, would be reached opened up a completely new area in the field of physics. Back then, these ideas were just visions and no practical or technological solutions or methods were available to actually build these kind of devices.

Today, few decades later, many of these ideas have already realized: Manufacturing computer chips with 30nm technique has become routine and even single molecules were squeezed between conducting electrodes. The scanning tunneling microscope was developed in 1981 which made possible for the first time to actually see individual atoms and manipulate their positions. As the size of the electronic systems decreases, many of their physical properties also change on the way. In the single atom or molecule scale, the electrical and transport properties are determined by quantum mechanics and the classical descriptions can rarely be applied. This is due to the fact that in such a small scale, the quantization of charge and individual electronic states take the leading role for the physical properties. In that case, even small changes, such as single electron tunneling events can make the difference to the observed physics. A typical example of such a behavior is Coulomb blockade where the conductance of the nanojunction is decreased due to the increase in the charging energy which blocks the current flow. Coulomb blockade effect can be observed in, *e.g.*, tunnel junctions and single electron transistors (SET) [6, 7].

The theoretical methods become increasingly important as we go into the nanoworld. There can be no understanding without proper theoretical description, especially when the observed phenomena are quantum mechanical in their nature. Simulations provide useful way to find qualitative and quantitative trends for observables and other quantities of interest by changing the system parameters: changing few parameters in simulation is much easier that changing the whole test subject in experiment! With the theoretical methods we can also make predictions of new phenomena, which might not yet be within reach by the experimental techniques at the moment. So there is still

plenty of room for theoretical work also.

1.1 Quantum transport – a quick overview

But why to be so enthusiastic about the charge transport? What makes it so special? The electron transport, especially the phenomena of *quantum transport* has become a hot topic since the first experiments on conductivity properties of single molecules [8, 9, 10]. Charge transport processes are elementary processes which have a fundamental role in almost every phenomenon in physics, chemistry and biology. One of the ultimate goals of nanophysics is to manufacture and control nanometer-scale systems which could potentially be used as building blocks for future electronic devices. Every measurement or attempt to control or manipulate a system with such a small size leads inevitably to electron transport phenomenon and, more precisely, to *ultrafast time-dependent* charge transfer where the quantum effects can play very important role. The fact that the quantum transport phenomenon involves *open* and *interacting* systems driven *out of equilibrium* where ultrafast time-dependent processes are present, can open up the door for completely new physical phenomena. It is therefore exceedingly important to understand these fundamental processes from first principles.

Lot of effort has already been invested to understand both steady-state and time-dependent transport phenomenon in nanostructures with many different approaches. The early transport models based on the celebrated kinetic Boltzmann equation describes the particles with probability distributions $f(\mathbf{r}, \mathbf{p}, t)$ the dynamics of which is dependent on the external forces and inter-particle collisions [11, 12]. This formulation, however, often relies on phenomenological arguments about the microscopic nature of the scattering processes but usually provides a relatively good starting point for classical and semi-classical description of electron transport. The extensions of this formalism, such as the theories based on Wigner functions [13] provide a similar framework and have been widely used for studying both quantum and semi-classical transport regime [14, 15, 16, 17, 18]. For investigating the truly quantum-mechanical and ultrafast charge transfer processes with a systematic treatment of the inter-particle interaction, rigorous microscopic theories are needed. While the detailed microscopical models, such as Time-Evolving Block Decimation (TEBD) method [19], Density matrix Renormalization Group (DMRG) method and its time-dependent version (tDMRG) [20, 21, 22, 23] provide a numerically exact approach for studying interacting quantum systems in and out of equilibrium, these models are often limited to finite and strongly correlated systems with short-range interactions neglecting the long-range nature of the Coulomb interaction. However, these models provide invaluable data for benchmarking the accuracy of other methods [24, 25]. Among the theoretical tools mentioned above, also the non-equilibrium dynamical mean-field theory (DMFT) has been applied to study transient properties of strongly correlated systems [26].

By far the leading formalism for treating larger interacting systems is the Density Functional Theory (DFT) [27, 28, 29]. Density functional formalism maps the problem of interacting particles into problem of effectively noninteracting particles while keeping the resulting density profiles the same. The density functional method and its time-dependent counterpart, Time-Dependent DFT (TDDFT) [30, 31] rely on the effective one-particle potential called *exchange-correlation potential* to capture the electronic exchange and correlation effects and has to be approximated. The density functional method, being very successful for variety of ground-state systems, however has still severe limitations in the time domain. The proper description of correlation effects and history- and initial state dependency, important for processes such as charge transport, excitation and ionization, demands time-nonlocal effective potentials which are still under intensive development. For application of TDDFT approach in quantum transport the reader is advised to see for example the references [32, 33, 34, 35, 36, 37].

In comparison to the density functional method, the non-equilibrium Green function (NEGF) method [38, 39, 11] has become an increasingly popular tool to simulate both steady-state [40, 41, 42, 43, 44, 45, 46, 47, 48, 49], transient [50, 51, 52, 53, 54, 55, 56, 57, 58], and AC dynamics [59, 60, 61]. NEGF formalism provides a systematic, perturbative approach to handle electron-electron interactions on a different levels of sophistication via the non-local self-energy operator, comparable to the exchange-correlation potential in DFT. In NEGF method the self-energy accounts for the Coulombic interactions to infinite order via the pre-determined selection or class of the self-energy *skeleton diagrams*, *i.e.* the Feynman diagrams for the elementary interaction processes. The focus in this method is then the proper selection of these diagrams. The NEGF method in combination with the density functional theory has also gained a lot of interest in modeling realistic and complex transport systems [62, 63, 64, 65]. The NEGF formalism, and especially the real-time Kadanoff-Baym approach, has also been applied to study many-body effects in correlated clusters and quantum dots[66, 67, 68, 69, 70] and both real [71, 72, 73] and artificial [74] atoms and molecules. Although the general formulation of Kadanoff-Baym method allows for its application to strongly correlated systems, the recent time-dependent simulations for these systems have also pointed out shortcomings of this method such as the possible existence of artificial damping in finite clusters in response to relatively strong perturbations [66].

1.2 This work

The work of this thesis is focused on theoretical and numerical modeling of time-dependent quantum transport in correlated metal-nanostructure-metal junctions using a real-time NEGF method. This means that we are simulating the real-time dynamical processes that happen as the electrons flow through and interact in a small and cor-

related nanostructure after the switch-on of the bias voltage. These processes are, for example, the development of the transient and steady-state current, charging effects, excitation effects, polarization effects and so on. As a platform for modeling these processes we use a transport setups, where a nanostructure (say, a quantum dot, quantum wire or molecule etc.) is squeezed between two macroscopic and metallic electrodes. The nanostructure is in physical contact with the electrodes so the electrons can pass through it. The word correlation in this context refers to the electron-electron interactions, but it is as frequently used to refer to the electron-electron interactions beyond the mean-field level. In particular, the part of the interaction which cannot be treated using effectively non-interacting single-particle equations.

In the simulations, we use the Keldysh-Kadanoff-Baym formalism [38] and its extension to open quantum systems to model transient response dynamics. This method is a time-resolved NEGF method and is capable of dealing with electron-electron interactions, memory effects, initial correlation and embedding effects, inhomogeneous external fields and open systems. It offers a natural framework to model ultrafast time-dependent quantum transport phenomena and to extract essential information out from it via the basic quantity, the one-particle Green function. Instead of modeling the transport phenomenon quantitatively with a detailed and atomistic description of lead band structures, central regions and hybridization links, in this work I focus on qualitative transport properties described by model Hamiltonians, with an emphasis on the time-dependence and electron correlations. How do the electron correlations and initial correlation effect influence the transient currents flowing through the system? How does the dynamics of the lead regions behave and how does the image-charge effects influence the transport properties? These are some of the fundamental questions that are investigated in the work of this thesis.

This thesis is organized as follows. In chapter 2 I first describe the theoretical foundations of the non-equilibrium Green functions and Kadanoff-Baym formalism. In the chapter 3 the Kadanoff-Baym method is then extended to open systems where the main subject of interest is the modeling of two-terminal quantum transport. In section 4 I show the numerical solutions of the embedded Kadanoff-Baym equations for various cases of transport. The Section 5 is then dedicated for conclusions and outlook.

2 Theory

In this chapter, the theoretical foundations of many-particle systems and quantum field theory are reviewed. The purpose of this section is to give an overall description of the non-equilibrium Green function theory and Keldysh formalism. For more detailed and extensive review of the non-equilibrium Green functions and Kadanoff-Baym equations, the reader is advised to look into Refs. [38, 39, 75, 76].

2.1 Many-particle systems

In quantum theory of many interacting particles, the system of interest is modeled with a Hermitian Hamiltonian operator $\hat{H}$ operating in a linear space called Hilbert space. Consider a system of N particles subjected to an external field u and interacting with each other and with a positive background via a long-range interaction w. The Hamiltonian operator describing this interacting many-particle system is given by

$$\hat{H}(t) = -\frac{1}{2}\sum_{i=1}^{N}\nabla_i^2 + \sum_{i=1}^{N}\sum_{j=1}^{N_n} Z_j w(\mathbf{r}_i, \mathbf{R}_j) + \sum_{i=1}^{N} u(\mathbf{r}_i, t) + \frac{1}{2}\sum_{i\neq j}^{N} w(\mathbf{r}_i, \mathbf{r}_j). \tag{2.1}$$

The first part describes the kinetic energy of the individual particles, the second part represents the interactions of each particle with the positive background formed by N_n fixed nucleus with each having the charge Z_j placed at $\mathbf{R}_j$, $j = 1...N_n$. The third term $u(\mathbf{r}_i, t)$ is the external potential for the electron at $\mathbf{r}_i$ and it can be generally time-dependent. Finally, the last term describes the long-range interaction between the particles, where the one half multiplier takes care that the interactions are not calculated twice. We also assume that the interaction term is symmetric in the spatial coordinates, so we have that $w(\mathbf{r}_i, \mathbf{r}_j) = w(\mathbf{r}_j, \mathbf{r}_i)$. We have also adopted atomic units for the Hamiltonian, *i.e.*, we have set $e = \hbar = m_e = 1$ to simplify the quantities.

Let us first assume that the external field is time-independent. According to the time-independent Schrödinger equation, the Hamiltonian $\hat{H}$ operated on the *wave function* $\Psi_k(\mathbf{x}_1, ..., \mathbf{x}_N)$ (which we assume to be the eigenstate of the Hamiltonian) returns the corresponding energy, E_k, of that state: $\hat{H}\Psi_k(\mathbf{x}_1, ..., \mathbf{x}_N) = E_k\Psi_k(\mathbf{x}_1, ..., \mathbf{x}_N)$. Here I have denoted $\mathbf{x}_i \equiv (\mathbf{r}_i, \sigma_i)$, where σ_i is the spin quantum number of particle i. The eigenstates $\Psi_k(\mathbf{x}_1, ..., \mathbf{x}_N)$ then contain all the information about the ground state ($k = 0$)

and excited states of the physical system. For Bosonic systems, the wave function is symmetric with respect to an interchange of two particles whereas for Fermionic systems, such as electronic systems, the wave functions are antisymmetric with respect to an interchange of two particles, *i.e.*,

$$\Psi(\mathbf{x}_1,...,\mathbf{x}_i,...,\mathbf{x}_j,...,\mathbf{x}_N) = \pm\Psi(\mathbf{x}_1,...,\mathbf{x}_j,...,\mathbf{x}_i,...,\mathbf{x}_N), \tag{2.2}$$

where the upper sign $(+)$ refers to Bosons and lower sign $(-)$ to Fermions. This symmetry property for Fermions is known as the Pauli principle and it states that no two particles with equal quantum numbers can occupy the same quantum state.

If the system is then subjected to a time-dependent perturbation, its dynamical behavior is governed by the time-dependent Schrödinger equation, $(i\partial_t - \hat{H}(t))\Psi(t) = 0$ with a suitable initial condition provided by the solution of the time-independent problem. The knowledge of the stationary or time-dependent N-particle wave function would allow us to calculate all the ground state properties and dynamical quantities such as currents, densities, dipole moments, excitation and ionization energies and other observables of great interest with guaranteed satisfaction of conservation laws. The exact solution of the Schrödinger equation becomes, however, increasingly complex as the size of the system increases: The general N-particle wave function is dependent on $3N$ spatial coordinates and if each coordinate has p entries the wave function is dependent on p^{3N} data entries which increases dramatically as the particle number N is increased. This then renders any practical exact methods inapplicable and other, approximative methods must be employed to treat equilibrium and non-equilibrium many-particle systems.

2.2 Second quantization

For the description of non-equilibrium processes, it is preferable to switch from the wave function -based framework, often referred as the first quantization, to operator -based framework where the particles can be added to the system and removed from the system via *creation* and *annihilation operators*. This framework is called second quantization and it is the starting point for the perturbation theory and theory of non-equilibrium Green functions. Let us go through the essential points of this formalism and restrict our study to concern only *Fermionic* systems.

The creation operator, $\hat{\psi}^\dagger(\mathbf{x})$, operated on an N-particle state vector $|\mathbf{x}_1,...,\mathbf{x}_N\rangle$ of N-particle Hilbert space $\mathscr{H}_N$ creates a particle to the system to position-spin coordinate $\mathbf{x}$ whereas the annihilation operator $\hat{\psi}(\mathbf{x})$ removes a particle from the system from position-spin coordinate $\mathbf{x}$. Explicitly, we have the following relations defining the ac-

tions of these Fermionic field operators on the N-particle state

$$\psi^\dagger(\mathbf{x})|\mathbf{x}_1,...,\mathbf{x}_N\rangle = |\mathbf{x}_1,...,\mathbf{x}_N,\mathbf{x}\rangle, \tag{2.3}$$

$$\psi(\mathbf{x})|\mathbf{x}_1,...,\mathbf{x}_N\rangle = \sum_{k=1}^{N}(-1)^{N-k}\delta(\mathbf{x}-\mathbf{x}_k)|\mathbf{x}_1,...,\mathbf{x}_{k-1},\mathbf{x}_{k+1},...,\mathbf{x}_N\rangle. \tag{2.4}$$

Here, the N-particle state $|\mathbf{x}_1,...,\mathbf{x}_N\rangle \in \mathscr{H}_N$ is transformed into $N+1$-particle state $|\mathbf{x}_1,...,\mathbf{x}_N,\mathbf{x}\rangle \in \mathscr{H}_{N+1}$ via the creation operator whereas the annihilation operator transforms it into linear combination of $N-1$-particle states ($\in \mathscr{H}_{N-1}$). Thus, the creation and annihilation operators provide mappings between the Hilbert spaces of different number of particles. Let us denote the collection of different particle number Hilbert spaces as *Fock space* $\mathscr{F} = \{\mathscr{H}_0, \mathscr{H}_1, ..., \mathscr{H}_N, ..\}$. Then, any N-particle state $|\mathbf{x}_1,...,\mathbf{x}_N\rangle \in \mathscr{H}_N$ can be obtained by consecutive application of creation operator on the empty 0-particle state $|0\rangle \in \mathscr{H}_0$

$$|\mathbf{x}_1,...,\mathbf{x}_N\rangle = \psi^\dagger(\mathbf{x}_N)...\psi^\dagger(\mathbf{x}_1)|0\rangle. \tag{2.5}$$

By the definition of the creation and annihilation operators (2.3) and (2.4), all the many-body properties and also the symmetry properties (2.2) of the N-particle wave function $\Psi(\mathbf{x}_1,...,\mathbf{x}_N) = \langle \mathbf{x}_N,...,\mathbf{x}_1|\Psi\rangle$, $|\Psi\rangle \in \mathscr{H}_N$ will be automatically built in to the properties of $\psi^\dagger(\mathbf{x})$ and $\psi(\mathbf{x})$. Explicitly, in the case of Fermions, the antisymmetry of the wave function is mapped into the anti-commutation rules for the Fermionic field operators

$$\begin{aligned} \left\{\hat{\psi}^\dagger(\mathbf{x}), \hat{\psi}(\mathbf{x}')\right\} &= \delta(\mathbf{x}-\mathbf{x}'), \\ \left\{\hat{\psi}^{(\dagger)}(\mathbf{x}), \hat{\psi}^{(\dagger)}(\mathbf{x}')\right\} &= 0, \end{aligned} \tag{2.6}$$

as can be easily checked from the definitions (2.3) and (2.4). Within the second quantization, any one- and two-body operators can be written in terms of the field operators. The action of a general one-body operator $\hat{O}$ of N-particle Hamiltonian can be written as

$$\begin{aligned} \hat{O}|\mathbf{x}_1,\cdots,\mathbf{x}_N\rangle &= \sum_{i=1}^{N} o(\mathbf{x}_i)|\mathbf{x}_1,\cdots,\mathbf{x}_N\rangle \\ &= \int d\mathbf{x}\hat{\psi}^\dagger(\mathbf{x})o(\mathbf{x})\hat{\psi}(\mathbf{x})|\mathbf{x}_1,\cdots,\mathbf{x}_N\rangle, \end{aligned} \tag{2.7}$$

where the integral denotes the integration over the position coordinate and summation over the spin degree of freedom: $\int d\mathbf{x} = \sum_\sigma \int d\mathbf{r}$. A special and very useful one-body operator is the density operator $\hat{n}(\mathbf{x})$ which is defined as

$$\begin{aligned} \hat{n}(\mathbf{x})|\mathbf{x}_1,\cdots,\mathbf{x}_N\rangle &= \hat{\psi}^\dagger(\mathbf{x})\hat{\psi}(\mathbf{x})|\mathbf{x}_1,\cdots,\mathbf{x}_N\rangle \\ &= \sum_{i=1}^{N}\delta(\mathbf{x}-\mathbf{x}_i)|\mathbf{x}_1,\cdots,\mathbf{x}_i,\cdots,\mathbf{x}_N\rangle. \end{aligned} \tag{2.8}$$

Now, by employing this expression for the density operator together with the anti-commutation rules (2.6), we can also write the two-body operator $\hat{W}$ as

$$\begin{aligned}\hat{W}|\mathbf{x}_1,\cdots,\mathbf{x}_N\rangle &= \frac{1}{2}\sum_{i\neq j}^{N} w(\mathbf{x}_i,\mathbf{x}_j)|\mathbf{x}_1,\cdots,\mathbf{x}_i,\cdots,\mathbf{x}_j,\cdots,\mathbf{x}_N\rangle \\ &= \frac{1}{2}\int d\mathbf{x}d\mathbf{y}\, w(\mathbf{x},\mathbf{y})\hat{\psi}^\dagger(\mathbf{x})\hat{\psi}^\dagger(\mathbf{y})\hat{\psi}(\mathbf{y})\hat{\psi}(\mathbf{x})|\mathbf{x}_1,\cdots,\mathbf{x}_N\rangle. \quad (2.9)\end{aligned}$$

The full many-body Hamiltonian (2.1) is then given by

$$\hat{H}(t) = \int d\mathbf{x}\,\hat{\psi}^\dagger(\mathbf{x})h(\mathbf{x},t)\hat{\psi}(\mathbf{x}) + \frac{1}{2}\int d\mathbf{x}d\mathbf{y}\, w(\mathbf{x},\mathbf{y})\hat{\psi}^\dagger(\mathbf{x})\hat{\psi}^\dagger(\mathbf{y})\hat{\psi}(\mathbf{y})\hat{\psi}(\mathbf{x}), \quad (2.10)$$

where the one-body part contains the external field and the background potential,

$$h(\mathbf{x},t) = -\frac{1}{2}\nabla^2 - \sum_{j=1}^{N_n} Z_j w(\mathbf{r},\mathbf{R}_j) + u(\mathbf{r},t), \quad (2.11)$$

and the long-range interaction for Coulombic systems has the behavior $w(\mathbf{x},\mathbf{y}) \sim 1/|\mathbf{r}_x - \mathbf{r}_y|$. Equation (2.10) is nothing more than a reformulation of the original Hamiltonian operator in terms of field operators in coordinate representation. Let us next turn our attention to non-equilibrium dynamics and review some useful definitions from time-dependent quantum mechanics and statistical physics. We shall later use them to introduce the main statistical quantity of the NEGF formalism, the Green function.

2.3 Nonequilibrium dynamics

2.3.1 Evolution of many-body states

Consider a normalized N-particle wave function $|\Psi(t)\rangle \in \mathscr{H}_N$ which satisfies the time-dependent Schrödinger equation $[i\partial_t - \hat{H}(t)]|\Psi(t)\rangle = 0$. The time-evolution of the state $|\Psi(t)\rangle$ from its initial configuration $|\Psi(t=t_0)\rangle = |\Psi_0\rangle$ can be characterized by introducing a *time-evolution operator* $\hat{U}(t,t_0)$

$$|\Psi(t)\rangle = \hat{U}(t,t_0)|\Psi(t_0)\rangle. \quad (2.12)$$

Since the wave function $|\Psi(t)\rangle$ satisfies the Schrödinger equation, it can be easily shown that the evolution operator obeys the following equations

$$\begin{aligned} i\partial_t\hat{U}(t,t') &= \hat{H}(t)\hat{U}(t,t'), \\ i\partial_{t'}\hat{U}(t,t') &= -\hat{U}(t,t')\hat{H}(t'), \end{aligned} \quad (2.13)$$

with the boundary condition $\hat{U}(t,t)=1$. If we now integrate the first equation of (2.13) from t' to t ($t>t'$) and iterate the resulting equation, the time-evolution operator acquires the form known as *Dyson series*

$$\hat{U}(t,t')=1+\sum_{n=1}^{\infty}\frac{(-i)^n}{n!}\int_{t'}^{t}dt_1\int_{t'}^{t}dt_2\cdots\int_{t'}^{t}dt_n\,\mathscr{T}\left[\hat{H}(t_1)\hat{H}(t_2)\cdots\hat{H}(t_n)\right], \quad (2.14)$$

which can be written compactly as

$$\hat{U}(t,t')=\mathscr{T}\left\{e^{-i\int_{t'}^{t}d\bar{t}\,\hat{H}(\bar{t})}\right\}\ (t>t'). \quad (2.15)$$

In the Eq. (2.14) we introduced so called *time-ordering operator* $\mathscr{T}$ which in its general form reads

$$\begin{aligned}&\mathscr{T}\left[\hat{A}_1(t_1)\hat{A}_2(t_2)\cdots\hat{A}_n(t_n)\right]\\&=\sum_P(-1)^{F_P}\theta(t_{P(1)},t_{P(2)})\theta(t_{P(2)},t_{P(3)})\cdots\theta(t_{P(n-1)},t_{P(n)})\\&\qquad\times\hat{A}_{P(1)}(t_{P(1)})\hat{A}_{P(2)}(t_{P(2)})\cdots\hat{A}_{P(n)}(t_{P(n)}),\end{aligned} \quad (2.16)$$

with $\theta(t,t')=1$ if $t>t'$ and zero otherwise. The time-ordering operator simply constructs all the possible chronological products from the operators $\hat{A}_1,\hat{A}_1,\cdots\hat{A}_n$ where the operators with later times are located to the left. It should be kept in mind that the Hamiltonian operator $\hat{H}$ is a Bosonic operator since it contains an even number of Fermionic field operators. In case that some of the operators $\hat{A}_k(t_k)$ are Fermionic, the parameter F_P denotes the number of interchanges between the Fermionic operators during the construction of desired ordering. For example, for two Fermionic operators $\hat{A}_1(\mathbf{x}_1t_1)$ and $\hat{A}_2(\mathbf{x}_2t_2)$ with $t_1\neq t_2$ we have

$$\begin{aligned}\mathscr{T}\left[\hat{A}_1(\mathbf{x}_1t_1)\hat{A}_2(\mathbf{x}_2t_2)\right] &= \theta(t_1,t_2)\hat{A}_1(\mathbf{x}_1t_1)\hat{A}_2(\mathbf{x}_2t_2)-\theta(t_2,t_1)\hat{A}_2(\mathbf{x}_2t_2)\hat{A}_1(\mathbf{x}_1t_1),\\&= -\mathscr{T}\left[\hat{A}_2(\mathbf{x}_2t_2)\hat{A}_1(\mathbf{x}_1t_1)\right].\end{aligned} \quad (2.17)$$

In the limit of equal times, we define that the time-ordering operator leaves the ordering untouched, *i.e.*, we have that

$$\mathscr{T}\left[\hat{A}_1(\mathbf{x}_1t)\hat{A}_2(\mathbf{x}_2t)\right]=\hat{A}_1(\mathbf{x}_1t)\hat{A}_2(\mathbf{x}_2t) \quad (2.18)$$

The time-ordering operator should not be confused with regular Hilbert space operators, since it does not operate on wave functions or state vectors. A similar derivation can be performed also for the case where $t<t'$ which gives

$$\hat{U}(t,t')=\tilde{\mathscr{T}}\left\{e^{-i\int_{t'}^{t}d\bar{t}\,\hat{H}(\bar{t})}\right\}\ (t<t'), \quad (2.19)$$

and describes the backward time-propagation of a state from later time t' to earlier time point t. Furthermore, the time-ordering operator is replaced with the *anti-chronological time-ordering operator* $\tilde{\mathcal{T}}$

$$\begin{aligned}&\tilde{\mathcal{T}}\left[\hat{A}_1(t_1)\hat{A}_2(t_2)\cdots\hat{A}_n(t_n)\right]\\&=\sum_P(-1)^{F_P}\theta(t_{P(1)}-t_{P(2)})\theta(t_{P(2)}-t_{P(3)})\cdots\theta(t_{P(n-1)}-t_{P(n)})\\&\qquad\times\hat{A}_{P(n)}(t_{P(n)})\hat{A}_{P(n-1)}(t_{P(n-1)})\cdots\hat{A}_{P(1)}(t_{P(1)}),\end{aligned}\tag{2.20}$$

ordering the operators with earliest times to the left.

Since the norm of the time-dependent wave function $\langle\Psi(t)|\Psi(t)\rangle$ must be conserved in the time-propagation, it follows that $\hat{U}$ is unitary: $\hat{U}^\dagger(t,t_0)=\hat{U}^{-1}(t,t_0)=\hat{U}(t_0,t)$. Moreover, $\hat{U}$ also satisfies the group property $\hat{U}(t,t')=\hat{U}(t,\bar{t})\hat{U}(\bar{t},t')$, *i.e.* the propagation over a specified time-interval can be performed in a piecewise-continuous manner.

2.3.2 Statistical averages and time-dependence

Let us next consider statistical averages of operators and the time-evolution of ensembles when they are subjected to time-dependent perturbations. An ensemble is a collection of identical and isolated systems where each of these systems is in a unique, normalized state characterized by $|\Psi_i\rangle$. Upon a measurement, the corresponding probability to find the system in a state $|\Psi_i\rangle$ is given by p_i with the constraint $\sum_i p_i=1$. The *ensemble average* of an operator $\hat{O}$ is then defined in the following way

$$\langle\hat{O}\rangle=\sum_i p_i\langle\Psi_i|\hat{O}|\Psi_i\rangle,\tag{2.21}$$

which is simply a weighted sum of the quantum averages with respect to the individual states of the ensemble. A useful way to characterize the ensemble of systems is the so called statistical density operator $\hat{\rho}=\sum_i p_i|\Psi_i\rangle\langle\Psi_i|$, which allows us to write the ensemble average of the operator $\hat{O}$ as

$$\begin{aligned}\langle\hat{O}\rangle&=\sum_i p_i\langle\Psi_i|\hat{O}|\Psi_i\rangle,\\&=\sum_{i,k}p_i\langle\Psi_i|\Phi_k\rangle\langle\Phi_k|\hat{O}|\Psi_i\rangle,\\&=\mathrm{Tr}\left\{\hat{\rho}\hat{O}\right\}.\end{aligned}\tag{2.22}$$

Here the trace $\mathrm{Tr}\{\hat{A}\}$ denotes the expectation values of an operator $\hat{A}$ with respect to the many-particle states $|\Phi_k\rangle$ of the ensemble.

It is our interest to study processes where a system is initially ($t = 0$) in equilibrium and we then switch on the external field to drive the system out of equilibrium. For this purpose, we need to consider canonical averages which are able to describe systems in thermal equilibrium with the environment. We know from the statistical physics that there exists a density operator, which considers the ensemble in contact with a heat/particle bath thus allowing heat and particle exchange between the bath and the ensemble. Such a system-bath configuration has a well defined and unique chemical potential μ and in the equilibrium condition they are at the same temperature T. The density operator for this *Grand canonical ensemble* is given by

$$\begin{aligned} \hat{\rho} &= \frac{1}{\mathscr{Z}} e^{-\beta(\hat{H}-\mu\hat{N})}, \\ &= \sum_{N=0}^{\infty}\sum_{i=1}^{\infty} p_{N_i} |\Psi_{N_i}\rangle\langle\Psi_{N_i}| \quad ; \quad p_{N_i} = \frac{1}{\mathscr{Z}} e^{-\beta(E_{N_i}-\mu N)} \end{aligned} \tag{2.23}$$

where $\mathscr{Z} = \mathrm{Tr}\{e^{-\beta(\hat{H}-\mu\hat{N})}\}$ is the partition function, $\beta = 1/(k_B T)$ is the inverse temperature with k_B the Boltzmann constant[1] and μ is the chemical potential coupled to the density operator $\hat{N}$ of the system. The p_{N_i} gives the probability for the system to have N particles and to be in the state $|\Psi_{N_i}\rangle$ from all the possible individual N-particle ensemble states. The energy corresponding to the N-particle state $|\Psi_{N_i}\rangle$ is then given by E_{N_i}. Now, according to equation (2.22) the equilibrium expectation value of the operator $\hat{O}$ in the Grand canonical ensemble becomes

$$\begin{aligned} \langle\hat{O}\rangle &= \frac{1}{\mathscr{Z}} \mathrm{Tr}\left\{e^{-\beta(\hat{H}-\mu\hat{N})}\hat{O}\right\}, \\ &= \frac{1}{\mathscr{Z}} \sum_{N=0}^{\infty}\sum_{i=1}^{\infty} e^{-\beta(E_{N_i}-\mu N)} \langle\Psi_{N_i}|\hat{O}|\Psi_{N_i}\rangle, \\ &= \frac{\sum_k e^{-\beta\tilde{E}_k}\langle\Psi_k|\hat{O}|\Psi_k\rangle}{\sum_k e^{-\beta\tilde{E}_k}}, \end{aligned} \tag{2.24}$$

where in the last step the summation is performed over the multi-index $k \equiv (N, i)$ characterizing the many-particle states in the Fock space and the energies $\tilde{E}_k = E_{N_i} - \mu N$ are associated to the grand canonical equilibrium Hamiltonian $\hat{H}_0 \equiv \hat{H} - \mu\hat{N}$ for $t < t_0$.

If we now switch on a time-dependent perturbation at $t = t_0$, each of the individual states of the ensemble, $|\Psi_k\rangle$, will evolve in time according to $|\Psi_k(t)\rangle = \hat{U}(t, t_0)|\Psi_k\rangle$. The expectation value of the operator $\hat{O}$, *i.e.* the equation (2.22) together with (2.24),

[1] From now on we set $k_B = 1$

can then be extended to time-domain as

$$\begin{aligned}\langle\hat{O}(t)\rangle &= \sum_k p_k\langle\Psi_k(t)|\hat{O}|\Psi_k(t)\rangle,\\ &= \frac{1}{\mathscr{Z}}\sum_k e^{-\beta\tilde{E}_k}\langle\Psi_k|\hat{U}(t_0,t)\hat{O}\hat{U}(t,t_0)|\Psi_k\rangle,\\ &= \frac{1}{\mathscr{Z}}\sum_k e^{-\beta\tilde{E}_k}\langle\Psi_k|\hat{O}_H(t)|\Psi_k\rangle,\\ &= \mathrm{Tr}\left\{\hat{\rho}\hat{O}_H(t)\right\}, \end{aligned} \tag{2.25}$$

with the statistical density operator

$$\hat{\rho} = \frac{e^{-\beta\hat{H}_0}}{\mathrm{Tr}\left\{e^{-\beta\hat{H}_0}\right\}}. \tag{2.26}$$

In equation (2.25) we defined a *Heisenberg picture representation* of the operator $\hat{O}$:

$$\hat{O}_H(t) = \hat{U}(t_0,t)\hat{O}\hat{U}(t,t_0), \tag{2.27}$$

which captures the time-dependence from the many-particle states into the operators themselves. In the Heisenberg picture, the operators satisfy the Heisenberg equation

$$i\frac{\partial}{\partial t}\hat{O}_H(t) = \left[\hat{O}_H(t),\hat{H}_H(t)\right] + i\left(\frac{\partial}{\partial t}\hat{O}(t)\right)_H, \tag{2.28}$$

which follows directly from the equations (2.13). This allows us to track the time-evolution of the expectation values as

$$i\partial_t\left\langle\hat{O}(t)\right\rangle = \left\langle\left[\hat{O}_H(t),\hat{H}_H(t)\right]\right\rangle + i\left\langle\left(\partial_t\hat{O}(t)\right)_H\right\rangle. \tag{2.29}$$

2.3.3 Keldysh contour

The equations (2.25) and (2.26) provide now an abstract way to evaluate the time-dependent expectation values of operators using the forward and backward time propagators and then evaluating the statistical average in the grand canonical ensemble. However, this equation can be made more general by extending the definition of the time-evolution operator and the time-ordering operator. If we look at the definition of the forward time-evolution operator (2.15) and the statistical density operator (2.26) it can be noticed that the Boltzmann factor $e^{-\beta\hat{H}_0}$ appearing in (2.26) can be written in terms of the evolution operator as

$$e^{-\beta\hat{H}_0} = \hat{U}(t_0 - i\beta, t_0). \tag{2.30}$$

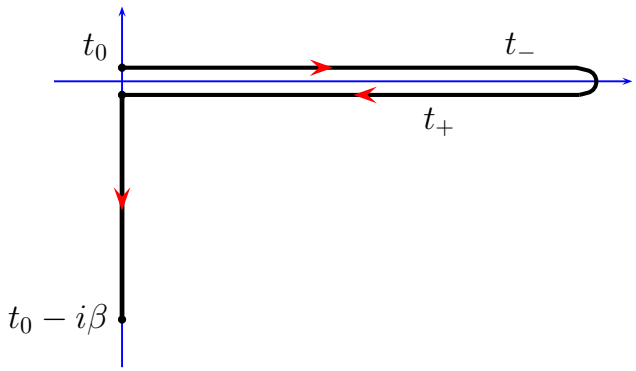

Figure 2.1: Keldysh contour consisting of forward (t_-) and backward (t_+) real-time branches and the thermal imaginary track ranging from t_0 to $t_0 - i\beta$.

This now corresponds to an imaginary time-propagation from t_0 to $t_0 - i\beta$ with the Hamiltonian $\hat{H}_0$. The expectation value (2.25) then attains the form

$$\langle \hat{O}(t) \rangle = \frac{\mathrm{Tr}\left\{ \hat{U}(t_0 - i\beta, t_0)\hat{U}(t_0, t)\hat{O}(t)\hat{U}(t, t_0) \right\}}{\mathrm{Tr}\left\{ \hat{U}(t_0 - i\beta, t_0) \right\}}. \tag{2.31}$$

Equation (2.31) can be interpreted as forward time-evolution of the system from t_0 to t where the operator $\hat{O}(t)$ acts and then backward propagation from t back to t_0 followed by the imaginary time-propagation from t_0 to $t_0 - i\beta$. By the introduction of the imaginary time-propagation (2.30), it is then natural to extend the meaning of time-argument from purely real times t to complex times z where the complex time argument z belongs to the time contour depicted in Fig. 2.1. This contour, consisting of forward (t_-) and backward (t_+) real-time branches and the imaginary equilibrium branch, is called the *extended Keldysh contour* which we from now on simply call the Keldysh contour.

In fact, the piecewise time-propagation procedure of equation (2.31) can be thought of as a forward time-propagation *along the Keldysh contour*. Since each time-evolution operator is known on the different branches of the contour, we may write the expectation value (2.31) compactly as

$$\langle \hat{O}(z) \rangle = \frac{\mathrm{Tr}\left\{ \mathscr{T}_C \left[e^{-i\int_C d\bar{z}\hat{H}(\bar{z})} \hat{O}(z) \right] \right\}}{\mathrm{Tr}\left\{ \mathscr{T}_C \left[e^{-i\int_C d\bar{z}\hat{H}(\bar{z})} \right] \right\}}, \tag{2.32}$$

where $\mathscr{T}_C$ is now the *contour time-ordering operator*, the same as in the equation (2.20) but the time-indices on the Keldysh contour C.

To conclude this subsection, we have derived the equation (2.32), which describes the time-evolution of the expectation value of operator $\hat{O}$ in response to the external time-dependent perturbation. The equation (2.32) takes into account correctly the initial

state before the time-dependent field is switched on and this initial state describes the system in thermal equilibrium with a heat/particle bath. It should be noted that the time-evolution is, however, performed for the system which is disconnected from the heat/particle bath, *i.e.*, the heat bath is used only to prepare the initial state for the system under investigation.

This expectation value can be extended to more than one operator and it opens up a way to define *correlation functions*. For example, consider the operators $\hat{O}_1(1)$, $\hat{O}_2(2)$,..., $\hat{O}_N(N)$, where $1 \equiv (\mathbf{x}_1 t_1), 2 \equiv (\mathbf{x}_2 t_2), ..., N \equiv (\mathbf{x}_N t_N)$ are the collective indices for position-spin and time coordinates. Then we can define a general N-point correlation function $C(1,...,N)$ on the Keldysh contour as

$$\begin{aligned} C(1,...,N) &= \left\langle \mathscr{T}_C \left[\hat{O}_{1,H}(1)\hat{O}_{2,H}(2)...\hat{O}_{N,H}(N) \right] \right\rangle \\ &= \frac{\mathrm{Tr}\left\{ \hat{U}(t_0 - i\beta, t_0)\mathscr{T}_C \left[\hat{O}_{1,H}(1)\hat{O}_{2,H}(2)...\hat{O}_{N,H}(N) \right] \right\}}{\mathrm{Tr}\left\{ \mathscr{T}_C \left[e^{-i\int_C dz \hat{H}(z)} \right] \right\}}. \end{aligned} \tag{2.33}$$

Usually, in the context of quantum field theory, the operators $\hat{O}_k(k)$ are replaced by the field operators and these correlation functions are then called Green functions. In the next chapter we take a deeper look into this concept and define the main tool of NEGF formalism, the one-particle Green function. We also inspect the properties of this correlation function and derive the equations of motion for the one-particle Green function on the Keldysh contour.

2.4 Nonequilibrium Green functions

In the following discussion, we shall restrict ourselves to Fermionic, such as electronic systems only.

2.4.1 One-particle Green function

The basic quantity in the theory of non-equilibrium Green functions is the one-particle Green function $G(1,2)$ which is defined as the expectation value of contour-ordered product of creation and annihilation operators in the following way:

$$\begin{aligned} G(1,2) &= -i\frac{\mathrm{Tr}\left\{\mathscr{T}_C\left[e^{-i\int_C \hat{H}(\bar{z})d\bar{z}}\,\hat{\psi}(1)\hat{\psi}^\dagger(2)\right]\right\}}{\mathrm{Tr}\left\{\hat{U}(t_0-i\beta,t_0)\right\}}, && (2.34)\\ &= -i\frac{\mathrm{Tr}\left\{\hat{U}(t_0-i\beta,t_0)\mathscr{T}_C\left[\hat{\psi}_H(1)\hat{\psi}^\dagger_H(2)\right]\right\}}{\mathrm{Tr}\left\{\hat{U}(t_0-i\beta,t_0)\right\}}, && (2.35)\\ &:= -i\left\langle\mathscr{T}_C\left[\hat{\psi}_H(1)\hat{\psi}^\dagger_H(2)\right]\right\rangle. && (2.36)\end{aligned}$$

This definition describes a process where a particle is created to the system at $(\mathbf{x}_2 t_2) = 2$ and the $N+1$-particle system is then evolved in time until a particle is removed from the system at $(\mathbf{x}_1 t_1) = 1$. Depending on the relative time-ordering of the field operators, the same procedure can be performed for *holes*, *i.e.*, for particle removal process. In that case, a particle is removed from the system at $(\mathbf{x}_1 t_1) = 1$ and the ionized $N-1$ -particle system is evolving in time until a particle is added back to the system at $(\mathbf{x}_2 t_2) = 2$. In other words, the Green function gives the probability amplitude for a process where a particle or hole is created into the system at some position and then removed later from a different position. This process is often visualized as a particle/hole propagation in the system. It is easy to check from the definition that the Green function satisfies important boundary conditions, the so called *Kubo-Martin-Schwinger* boundary conditions, which are given by

$$\begin{aligned} G(\mathbf{x}_1 t_0 - i\beta, 2) &= -G(\mathbf{x}_1 t_0, 2), && (2.37)\\ G(1, \mathbf{x}_2 t_0 - i\beta) &= -G(1, \mathbf{x}_2 t_0). && (2.38)\end{aligned}$$

These boundary conditions are fundamental properties of all the Fermionic Green functions defined by (2.35) and they are valid for higher order Green functions as well. The KMS boundary conditions are used to determine unique solutions for the equations of motion as we shall see later.

Let us now look explicitly into the different time-orderings of the creation and annihilation operators on the Keldysh contour. We can write the Green function in two

pieces:

$$G(1,2) = \theta(z_1,z_2)G^{>}(1,2) + \theta(z_2,z_1)G^{<}(1,2), \tag{2.39}$$

where $\theta(z_1,z_2)$ is the contour step function

$$\theta(z_1,z_2) = \begin{cases} 1 & z_1 \text{ later on the contour than } z_2 \\ 0 & z_1 \text{ earlier on the contour than } z_2 \end{cases} \tag{2.40}$$

Here we introduced the *greater* ($G^{>}$) and *lesser* ($G^{<}$) Green functions

$$G^{>}(1,2) = -i\left\langle \hat{\psi}_H(1)\hat{\psi}_H^{\dagger}(2)\right\rangle, \tag{2.41}$$

$$G^{<}(1,2) = +i\left\langle \hat{\psi}_H^{\dagger}(2)\hat{\psi}_H(1)\right\rangle. \tag{2.42}$$

In the definition of the lesser Green function, an extra $-$ sign is introduced due to the interchange of the Fermionic operators by the contour ordering operator. The greater and lesser Green functions are now the particle and hole propagators and they contain the information about the dynamics of $N+1$-particle system (electron affinities) and $N-1$-particle system (ionization) correspondingly. Furthermore, it can also be easily checked that the greater and lesser Green functions obey very useful symmetry relations

$$\left[G^{\lessgtr}(1,2)\right]^{*} = -G^{\lessgtr}(2,1), \tag{2.43}$$

$$\left[G^{>}(\mathbf{x}_1 t,\mathbf{x}_2 t) - G^{<}(\mathbf{x}_1 t,\mathbf{x}_2 t)\right] = -i\delta(\mathbf{x}_1-\mathbf{x}_2). \tag{2.44}$$

From the lesser and greater Green functions we can derive so called *Retarded* (G^R) and *Advanced* (G^A) real-time Green functions

$$\begin{aligned} G^R(1,2) &= \theta(t_1,t_2)\Big[G^{>}(1,2) - G^{<}(1,2)\Big], \\ &:= -i\theta(t_1,t_2)A(1,2), \end{aligned} \tag{2.45}$$

$$\begin{aligned} G^A(1,2) &= -\theta(t_2,t_1)\Big[G^{>}(1,2) - G^{<}(1,2)\Big], \\ &:= i\theta(t_2,t_1)A(1,2), \end{aligned} \tag{2.46}$$

where we also defined the *spectral function* $A(1,2)$ as

$$\begin{aligned} A(1,2) &= i\Big[G^{>}(1,2) - G^{<}(1,2)\Big], \\ &= \left\langle\left\{\hat{\psi}_H(1),\hat{\psi}_H^{\dagger}(2)\right\}\right\rangle. \end{aligned} \tag{2.47}$$

The retarded and advanced Green functions encapsulate both the ionization and electron addition processes into one correlation function with a restricted action in the time-domain. It can be checked effortlessly that the retarded and advanced Green functions

are related to each other and to lesser and greater Green functions via the following relations

$$G^R(1,2) - G^A(1,2) = G^>(1,2) - G^<(1,2), \tag{2.48}$$
$$\left[G^R(1,2)\right]^* = G^A(2,1). \tag{2.49}$$

The lesser and greater Green functions (2.41) gives also rise to two *mixed time-variable* Green functions

$$G^\rceil(1,2) = G^<(\mathbf{x_1}t_1, \mathbf{x_2}t_0 - i\tau_2), \tag{2.50}$$
$$G^\lceil(1,2) = G^>(\mathbf{x_1}t_0 - i\tau_1, \mathbf{x_2}t_2), \tag{2.51}$$

where the other time-argument lies on the real-time axis ($t_{1,2}$) and the other one is on the imaginary track ($\tau_{1,2}$) of the Keldysh contour, $\tau_{1,2} \in [0, \beta]$. By construction, these components will play a role in accounting the initial correlations and initial state dependence from the vertical track of the time-contour. Finally, apart from the mixed Green functions, we can define the equilibrium, or *Matsubara* Green function G^M where both of the time-arguments lie on the imaginary track of the contour:

$$\begin{aligned} G^M(1,2) &= G(\mathbf{x}_1 t_0 - i\tau_1, \mathbf{x}_2 t_0 - i\tau_2), \\ &= \theta(\tau_1,\tau_2)G^>(\mathbf{x}_1 t_0 - i\tau_1, \mathbf{x}_2 t_0 - i\tau_2) + \theta(\tau_2,\tau_1)G^<(\mathbf{x}_1 t_0 - i\tau_1, \mathbf{x}_2 t_0 - i\tau_2). \end{aligned} \tag{2.52}$$

This Green function, being completely real-time independent, corresponds to the ground state and also the initial state for the system under investigation.

2.4.2 Connection to observables

The Green function provides a direct access to several interesting properties of the system. For example, the equal-time limit gives directly the particle spin density at space-time point $1 = \mathbf{x}_1 t_1$

$$\langle \hat{n}(1) \rangle = \left\langle \hat{\psi}_H^\dagger(1)\hat{\psi}_H(1) \right\rangle = -iG^<(1,1^+), \tag{2.53}$$

and the total number of particles at time t_1 can be obtained by integrating particle density over spatial coordinates

$$N_{\text{tot}}(t_1) = -i \int d\mathbf{x}_1 G^<(\mathbf{x}_1 t_1, \mathbf{x}_1 t_1^+) \tag{2.54}$$

Furthermore, the expectation value of any one-body operator $\hat{O}$ can be obtained via the equal-time lesser Green function

$$\left\langle \hat{O}(t) \right\rangle = -i \int d\mathbf{x} \left\{ o(\mathbf{x}', t) G^{<}(\mathbf{x}t, \mathbf{x}'t^{+}) \right\}_{\mathbf{x}'=\mathbf{x}}, \tag{2.55}$$

which can be extended to include the interaction energy as well and thus obtain the total energies of the interacting quantum systems, such as atoms and molecules [72] via the Galitskii-Migdal formula [77, 39]

$$\begin{aligned} E(t_1) &= \left\langle \hat{H}(t_1) \right\rangle \\ &= -\frac{i}{2} \int d\mathbf{x_1} \left\{ \left[i\partial_{t_1} + h(1) \right] G^{<}(1,2) \right\}_{1=2}. \end{aligned} \tag{2.56}$$

2.4.3 Spectral properties from the Green function

As already mentioned, the Green function contains the information on the induced dynamics of a particle/hole propagation in the system. In fact, with a simple derivation of so called *Lehmann representation*, following directly from the definition (2.35) of the Green function, it can be seen that the frequency space lesser and greater Green functions are peaked at the removal and addition energies of the system. For unperturbed and isolated system at zero temperature the real-time expressions of these functions are given by

$$G^{<}(1,2) = +i \sum_k e^{-i\epsilon_k^{N-1}(t_1-t_2)} g_{N-1}^k(\mathbf{x}_1) g_{N-1}^{k*}(\mathbf{x}_2), \tag{2.57}$$

$$G^{>}(1,2) = -i \sum_k e^{-i\epsilon_k^{N+1}(t_1-t_2)} g_{N+1}^k(\mathbf{x}_1) g_{N+1}^{k*}(\mathbf{x}_2), \tag{2.58}$$

where $\epsilon_k^{N-1} = E_{0,N} - E_{k,N-1}$ and $\epsilon_k^{N+1} = E_{k,N+1} - E_{0,N}$ with $E_{0,N}$, $E_{k,N\pm1}$ the ground state energy of N-particle system and k'th energy of $N \pm 1$-particle system correspondingly. Moreover, $g_{N-1}^k(\mathbf{x}_1) = \langle \Phi_{k,N-1} | \hat{\psi}(\mathbf{x}_1) | \Psi_{0,N} \rangle$ and $g_{N+1}^k(\mathbf{x}_1) = \langle \Psi_{0,N} | \hat{\psi}(\mathbf{x}_1) | \Phi_{k,N+1} \rangle$ are the amplitudes corresponding to the phase factors $\epsilon_k^{N\pm1}$ where the states $|\Psi_{0,N}\rangle$ and $|\Phi_{k,N\pm1}\rangle$ are associated to the energies $E_{0,N}$ and $E_{k,N\pm1}$. The functions (2.57) and (2.58) oscillate in relative time $t = t_1 - t_2$ with the energies ϵ_k^{N-1} and ϵ_k^{N+1} which equal the ionization potentials (removal energy of an electron) and electron affinities (addition energy of an electron) of the system. If we then Fourier transform the real-time Green functions (2.57) and (2.58) to frequency space according to

$$G^{\lessgtr}(\mathbf{x}_1, \mathbf{x}_2, \omega) = \int \frac{dt}{2\pi} e^{i\omega t} G^{\lessgtr}(\mathbf{x}_1, \mathbf{x}_2, t), \tag{2.59}$$

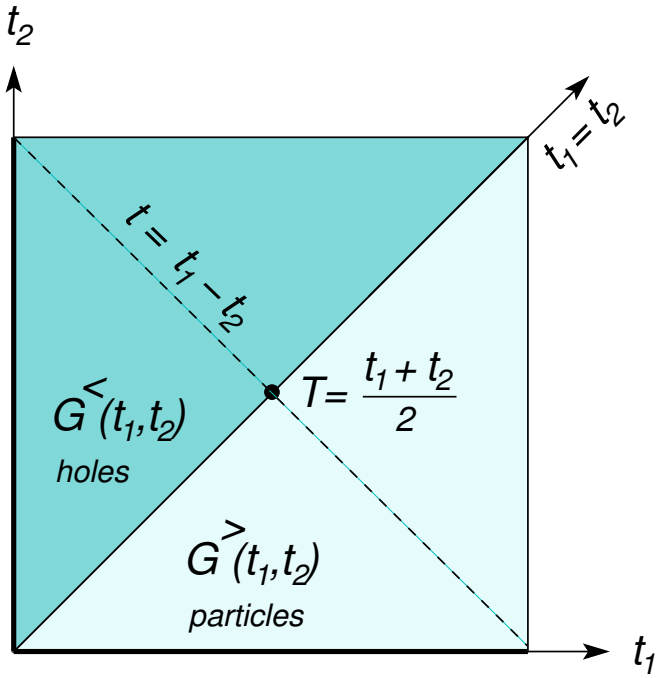

Figure 2.2: The double-time plane cartoon of the Green functions $G^{\lessgtr}(t,t')$.

and use the spectral representation for the delta function

$$\delta(\omega) \;=\; \int \frac{dt}{2\pi} e^{i\omega t}, \tag{2.60}$$

we obtain the frequency space formula for the particle and hole propagators

$$G^{\lessgtr}(\mathbf{x}_1,\mathbf{x}_2,\omega) = \pm i \sum_k g^k_{N\mp1}(\mathbf{x}_1)\, g^{k*}_{N\mp1}(\mathbf{x}_2)\, \delta(\omega - \epsilon^{N\mp1}_k), \tag{2.61}$$

with a characteristic delta-peak structure.

In the similar fashion we can construct more general non-equilibrium spectral function (2.47) in ω-space by transforming it with respect to the relative time coordinate $t = t_1 - t_2$ for a given center-of-time coordinate $T = (t_1 + t_2)/2$:

$$A(\mathbf{x}_1,\mathbf{x}_2,T,\omega) \;=\; i \int \frac{dt}{2\pi}\, e^{i\omega t} \left[G^> - G^<\right](\mathbf{x}_1 T + \frac{t}{2}, \mathbf{x}_2 T - \frac{t}{2}), \tag{2.62}$$

which reduces to normal Fourier transform when the system reaches time-translational invariance. The figure 2.2 demonstrates the Green function components in double-time plane together with the time-axis t.

The spectral function is closely related to the density of states (DOS) which can be obtained by simply taking the trace (integrating) over the spatial degrees of freedom.

Furthermore, for finite temperatures, the Green function and the spectral function are related to each other via *fluctuation-dissipation* theorem

$$G^{<}(\omega) = if(\omega)A(\omega), \tag{2.63}$$
$$G^{>}(\omega) = -i[1-f(\omega)]A(\omega), \tag{2.64}$$

which relates the fluctuations contained in the particle and hole Green functions $G(\omega)$ to the dissipative effects described by the spectral function $A(\omega)$ via the Fermi distribution function $f(\omega)$ [11]

$$f(\omega) = \frac{1}{e^{\beta(\omega-\mu)}+1}. \tag{2.65}$$

For infinite or embedded and correlated systems the level structure described by the series of delta-functions (see Eq. (2.61)) broadens and the well-defined single-particle spectrum transforms into a *quasiparticle spectrum* with a finite lifetime specified by the broadening. As we shall see later, the electronic correlations and embedding effects can give rise to substantial broadening and damping to the Green function which reflects to the spectral properties and physical observables.

2.4.4 Equation of motion and the self-energy

Now, as we have defined the one-particle Green function, we can derive the equation of motion for it. Let us first consider the Heisenberg equation (2.28) for the creation and annihilation operators. By applying equation (2.28) to $\hat{\psi}_H(1)$ and $\hat{\psi}^\dagger_H(1)$ with the Hamiltonian (2.10), we get with a simple derivation

$$\begin{aligned} i\partial_{z_1}\hat{\psi}_H(1) &= \left[\hat{\psi}_H(1), \hat{H}_H(z_1)\right], \\ &= h(1)\hat{\psi}_H(1) + \int d2\, w(1,2)\hat{\psi}^\dagger_H(2)\hat{\psi}_H(2)\hat{\psi}_H(1), \end{aligned} \tag{2.66}$$

$$\begin{aligned} i\partial_{z_1}\hat{\psi}^\dagger_H(1) &= \left[\hat{\psi}^\dagger_H(1), \hat{H}_H(z_1)\right], \\ &= -h(1)\hat{\psi}^\dagger_H(1) - \int d2\, w(1,2)\hat{\psi}^\dagger_H(1)\hat{\psi}^\dagger_H(2)\hat{\psi}_H(2). \end{aligned} \tag{2.67}$$

Here we introduced a shorthand notation $1 \equiv (\mathbf{x}_1 z_1)$ and the integration is performed over the space, spin and over the time contour: $\int d2 = \int d\mathbf{x}_2 \int_C dz_2$. Furthermore, the two-body term is written compactly as $w(1,2) = \delta(z_1,z_2)w(\mathbf{x}_1,\mathbf{x}_2)$, where the $\delta(z_1,z_2)$ is the contour delta-function.

If we now take a partial time derivatives from the Green function (2.39) and use (2.41) with the above equations for the field operators we obtain

$$i\partial_{z_1}G(1,2) = \delta(1,2)+h(1)G(1,2)-i\int d3\, w(1,3)\, G_2(1,3;2,3^+), \quad (2.68)$$

$$-i\partial_{z_2}G(1,2) = \delta(1,2)+h(2)G(1,2)-i\int d3\, w(2,3)\, G_2(1,3^-;2,3), \quad (2.69)$$

where we denoted $\delta(1,2)=\delta(\mathbf{x}_1,\mathbf{x}_2)\delta(z_1,z_2)$ and defined the *two-particle Green function* $G_2(1,3;2,3^+)$:

$$\begin{aligned} G_2(1,3;2,3^+) &= +\left\langle \mathscr{T}_C\left[\hat{\psi}_H(1)\hat{n}_H(3)\hat{\psi}^\dagger_H(2)\right]\right\rangle \\ &= -\left\langle \mathscr{T}_C\left[\hat{\psi}_H(1)\hat{\psi}_H(3)\hat{\psi}^\dagger_H(3^+)\hat{\psi}^\dagger_H(2)\right]\right\rangle \end{aligned} \quad (2.70)$$

Here $n^\pm$ ($n=1,2,\cdots$) means that the time-argument is taken infinitesimally later (+) or earlier (−) on the contour, *i.e.*, $n^\pm=\lim_{\eta\to 0}\{\mathbf{x}_n,z_n\pm\eta\}$ and the limit is taken *after* the time-ordering to keep the field operators in the correct order. The two-particle Green function contains two creation and annihilation operators and it then describes the propagation of two particles, two holes, or a particle and a hole in the system depending again on the relative time-orderings of the field operators. The two-particle Green function arises now from the commutator of the field operator with the two-body interaction term which actually describes the scattering of particles in an interacting system. Therefore, to be able to determine the time-dependence of the one-particle Green function, we should have knowledge on the time-dependent two-particle Green function which we know only by solving the kinetic equations for G_2. However, as we have already seen, due to the interaction term in the Hamiltonian, our kinetic equations for G_2 will be dependent again on the three-particle Green function G_3. In fact, this hierarchy between the Green functions continues and the determination of a general n-particle Green function

$$G_n(1,\cdots,n;1',\cdots,n') = (-i)^n\left\langle \mathscr{T}_C\left[\hat{\psi}_H(1)\cdots\hat{\psi}_H(n)\hat{\psi}^\dagger_H(n')\cdots\hat{\psi}^\dagger_H(1')\right]\right\rangle, \quad (2.71)$$

demands the knowledge of $n+1$ -particle Green function. These higher order Green functions describe the processes that may occur as an additional interacting particle is propagating in the system, *i.e.*, they contain the information of all the higher order scattering processes induced by the propagating particle.

A general strategy to continue from here is to cut the hierarchy for the Green functions and to close the equations of motion by introducing electronic *self-energy* operators Σ^{MB} and $\tilde{\Sigma}^{\mathrm{MB}}$ in the following way:

$$-i\int d3\, w(1,3)G_2(1,3;2,3^+) = \int d3\, \Sigma^{\mathrm{MB}}(1,3)G(3,2), \quad (2.72)$$

$$-i\int d3\, w(2,3)G_2(1,3^-;2,3) = \int d3\, G(1,3)\tilde{\Sigma}^{\mathrm{MB}}(3,2). \quad (2.73)$$

It is not difficult to show that the self-energies are actually the same, $\Sigma^{\mathrm{MB}} = \tilde{\Sigma}^{\mathrm{MB}}$. Now, by closing the equation of motion for the Green function, we encapsulate all the complicated electron-electron interaction processes into the self-energy and the remaining problem is then to find suitable approximations for this quantity.

The self-energy insertion can be thought of as a scattering potential where the particle propagates and the sophistication of the self-energy determines the mechanisms how the electrons are interacting with each other. This will have a major influence on the physical properties that the Green function is able to capture from the system. With the introduction of the self-energy, the equations of motion can then be written compactly as

$$\left\{i\partial_{z_1} - h(1)\right\}G(1,2) = \delta(1,2) + \int d3\,\Sigma^{\mathrm{MB}}(1,3)G(3,2), \tag{2.74}$$

$$\left\{-i\partial_{z_2} - h(2)\right\}G(1,2) = \delta(1,2) + \int d3\,G(1,3)\Sigma^{\mathrm{MB}}(3,2). \tag{2.75}$$

The simplest solution to the equations of motion (2.74) and (2.75) can be obtained by simply switching off the long-range interactions, $w = 0$. The equations of motion for the resulting noninteracting Green function g_0 then simply reads

$$\left\{i\partial_{z_1} - h(1)\right\}g_0(1,2) = \delta(1,2), \tag{2.76}$$

$$\left\{-i\partial_{z_2} - h(2)\right\}g_0(1,2) = \delta(1,2), \tag{2.77}$$

which have the solutions

$$g_0^{\lessgtr}(1,2) = \vec{U}(z_1,z_0)g_0^{\lessgtr}(\mathbf{x}_1 z_0, \mathbf{x}_2 z_0)\overleftarrow{U}(z_0,z_2), \tag{2.78}$$

where $\overleftarrow{U}$ and $\vec{U}$ are the time-evolution operators operating into the direction specified by the arrow. Moreover, the quantities $g_0^{\lessgtr}(\mathbf{x}_1 z_0, \mathbf{x}_2 z_0)$ are the initial density matrices

$$g_0^{<}(\mathbf{x}_1 z_0, \mathbf{x}_2 z_0) = +i\frac{\mathrm{Tr}\left\{e^{-\beta\hat{h}_0}\hat{\psi}^\dagger(\mathbf{x}_2)\hat{\psi}(\mathbf{x}_1)\right\}}{\mathrm{Tr}\left\{e^{-\beta\hat{h}_0}\right\}}, \tag{2.79}$$

$$g_0^{>}(\mathbf{x}_1 z_0, \mathbf{x}_2 z_0) = -i\frac{\mathrm{Tr}\left\{e^{-\beta\hat{h}_0}\hat{\psi}(\mathbf{x}_1)\hat{\psi}^\dagger(\mathbf{x}_2)\right\}}{\mathrm{Tr}\left\{e^{-\beta\hat{h}_0}\right\}}, \tag{2.80}$$

with $\hat{h}_0$ the noninteracting Hamiltonian on the vertical track of the Keldysh contour.

The noninteracting Green function can also be used to transform the integro-differential

equations of motion (2.74) and (2.75) to equivalent integral equations[1]

$$\begin{aligned} G(1,2) &= g_0(1,2) + \int d3\, d4\, g_0(1,3)\Sigma^{\mathrm{MB}}(3,4)G(4,2), \\ &= g_0(1,2) + \int d3\, d4\, G(1,3)\Sigma^{\mathrm{MB}}(3,4)g_0(4,2), \end{aligned} \tag{2.81}$$

and the KMS boundary conditions guarantee the uniqueness on this solution. In fact, the boundary conditions for g_0 automatically provides the correct boundary conditions also for the full Green function G. Equation (2.81) is generally known as the *Dyson equation* and it provides a way to obtain iterative solution to the full interacting Green function starting from a noninteracting or mean-field[2] g_0 and a selection for the self-energy. Let us next derive self-consistent and conserving many-body approximations for the electronic self-energy, which is the key quantity in including the electron correlation effects into the dynamics of the Green function.

2.5 Self-energy approximations and conservation laws

2.5.1 Hartree-Fock and 2nd Born approximations

The self-consistent self-energy approximations can be obtained by expanding the full interacting Green function (2.35) in powers of the two-body interaction w and this perturbation expansion of G is probably the most popular way to introduce self-energy operator and to construct higher order approximations for it. This method will also lead to the Dyson equation (2.81) with an irreducible electronic self-energy insertion Σ^{MB} [39, 75]. However, an alternative approach based on variational derivatives can be used in determining Σ for different level of sophistication. The basic idea of this method is to investigate how the variations in the external potential v affect the one-particle Green function, *i.e.*, we are interested in the quantity $\delta G(1,2)/\delta v(3)$. For this purpose let us calculate the functional derivative directly from the definition of the Green function (2.35)

[1] One can obtain this by simply multiplying the first (second) equation of motion with $g_0(1',1)$ ($g_0(2,1')$), partial integrating over the 1 (2) variable and using the KMS boundary conditions together with the fact that the Green functions go to zero when the separation of the spatial variables becomes large.

[2] We will see this in the next subsection, where we consider different many-body approximations for the self-energy.

$$\frac{\delta G(1,2)}{\delta v(3)} = \frac{\delta}{\delta v(3)}\left\{-i\frac{\mathrm{Tr}\left\{\mathscr{T}_C\left[e^{-i\int_C \hat{H}(\bar{z})d\bar{z}}\,\hat{\psi}(1)\hat{\psi}^\dagger(2)\right]\right\}}{\mathrm{Tr}\left\{\mathscr{T}_C\left[e^{-i\int_C \hat{H}(\bar{z})d\bar{z}}\right]\right\}}\right\},$$

$$= -i\frac{\mathrm{Tr}\left\{\mathscr{T}_C\left[\frac{\delta}{\delta v(3)}\left[e^{-i\int_C \hat{H}(\bar{z})d\bar{z}}\right]\,\hat{\psi}(1)\hat{\psi}^\dagger(2)\right]\right\}}{\mathrm{Tr}\left\{\mathscr{T}_C\left[e^{-i\int_C \hat{H}(\bar{z})d\bar{z}}\right]\right\}}$$
$$+i\frac{\mathrm{Tr}\left\{\mathscr{T}_C\left[\frac{\delta}{\delta v(3)}\left[e^{-i\int_C \hat{H}(\bar{z})d\bar{z}}\right]\right]\right\}\mathrm{Tr}\left\{\mathscr{T}_C\left[e^{-i\int_C \hat{H}(\bar{z})d\bar{z}}\,\hat{\psi}(1)\hat{\psi}^\dagger(2)\right]\right\}}{\mathrm{Tr}\left\{\mathscr{T}_C\left[e^{-i\int_C \hat{H}(\bar{z})d\bar{z}}\right]\right\}\mathrm{Tr}\left\{\mathscr{T}_C\left[e^{-i\int_C \hat{H}(\bar{z})d\bar{z}}\right]\right\}}. \tag{2.82}$$

This equation simplifies when we insert the explicit functional derivative of the contour evolution operator

$$\mathscr{T}_C\left\{\frac{\delta}{\delta v(3)}\left[e^{-i\int_C \hat{H}(\bar{z})d\bar{z}}\right]\right\} = \mathscr{T}_C\left\{e^{-i\int_C \hat{H}(\bar{z})d\bar{z}}\times\left\{-i\int_C \frac{\delta\hat{H}(\bar{z})}{\delta v(3)}d\bar{z}\right\}\right\},$$
$$= \mathscr{T}_C\left\{-i\,e^{-i\int_C \hat{H}(\bar{z})d\bar{z}}\,\hat{n}(3)\right\}, \tag{2.83}$$

since

$$\delta\hat{H}(z) = \int d\mathbf{x}\,\delta v(\mathbf{x}z)\hat{n}(\mathbf{x}). \tag{2.84}$$

In the last step of equation (2.83) we have inserted a contour time-argument t_3 into the density operator $\hat{n}(3) = \hat{n}(\mathbf{x}_3 t_3)$ to take into account the different time-orderings by the contour time-ordering operator. The equation (2.82) now becomes

$$\frac{\delta G(1,2)}{\delta v(3)} = -G_2(1,3;2,3^+) + i\langle\hat{n}(3)\rangle G(1,2), \tag{2.85}$$
$$= -G_2(1,3^-;2,3) + i\langle\hat{n}(3)\rangle G(1,2), \tag{2.86}$$

where $G_2(1,3;2,3^+)$ ($G_2(1,3^-;2,3)$) is again the two-particle Green function (2.70). It is worth stressing that, since the one- and two-particle Green functions satisfy the KMS boundary conditions, also the $\delta G(1,2)/\delta v(3)$ satisfies the same boundary conditions. Solving the equation (2.85) for $-iG_2$ and inserting it back into the equations of motion

(2.68) and (2.69), we get

$$\begin{aligned}\Big\{i\partial_{z_1}-h(1)\Big\}G(1,2) &= \delta(1,2)+G(1,2)\int d3\,w(1,3)\langle\hat{n}(3)\rangle \\ &\quad + i\int d3\,w(1,3)\frac{\delta G(1,2)}{\delta v(3)}, \qquad (2.87)\\ \Big\{-i\partial_{z_2}-h(2)\Big\}G(1,2) &= \delta(1,2)+G(1,2)\int d3\,w(2,3)\langle\hat{n}(3)\rangle. \\ &\quad + i\int d3\,w(2,3)\frac{\delta G(1,2)}{\delta v(3)} \qquad (2.88)\end{aligned}$$

Let us next find an explicit expression for $\delta G(1,2)/\delta v(3)$ by calculating the variation of equations (2.74) and (2.75)

$$\begin{aligned}\Big\{i\partial_{z_1}-h(1)\Big\}\frac{\delta G(1,2)}{\delta v(3)} &= \delta(1,3)G(1,2)+\int d4\,\frac{\delta\Sigma(1,4)}{\delta v(3)}G(4,2) \\ &\quad +\int d4\,\Sigma(1,4)\frac{\delta G(4,2)}{\delta v(3)}, \qquad (2.89)\\ \Big\{-i\partial_{z_2}-h(2)\Big\}\frac{\delta G(1,2)}{\delta v(3)} &= \delta(2,3)G(1,2)+\int d4\,\frac{\delta G(1,4)}{\delta v(3)}\Sigma(4,2) \\ &\quad +\int d4\,G(1,4)\frac{\delta\Sigma(4,2)}{\delta v(3)}. \qquad (2.90)\end{aligned}$$

These equations can now be solved for $\delta G(1,2)/\delta v(3)$. For example, by multiplying (2.89) with $G(1',1)$ and partial integrating over the space-time variable 1 we obtain

$$\begin{aligned}\int d1\,G(1',1)\Big\{i\partial_{z_1}-h(1)\Big\}\frac{\delta G(1,2)}{\delta v(3)} &\overset{\text{KMS}}{=} \int d1\,\Big\{\Big\{-i\partial_{z_1}-h(1)\Big\}G(1',1)\Big\}\frac{\delta G(1,2)}{\delta v(3)} \\ &\overset{\text{EOM}}{=} \frac{\delta G(1',2)}{\delta v(3)}+\int d1d4\,G(1',4)\Sigma(4,1)\frac{\delta G(1,2)}{\delta v(3)}, \qquad (2.91)\end{aligned}$$

where in the first step we used the KMS boundary conditions (2.37) for G and $\delta G/\delta v$ and in the second step the equations of motion (2.75). This gives directly the expression for $\delta G(1,2)/\delta v(3)$

$$\frac{\delta G(1,2)}{\delta v(3)} = G(1,3)G(3,2)+\int d4\,d5\,G(1,4)\frac{\delta\Sigma(4,5)}{\delta v(3)}G(5,2). \qquad (2.92)$$

A similar procedure can be also done for the adjoint equation (2.90). Let us now define a so called vertex function $\Gamma(12;3)$

$$\Gamma(12;3)=\delta(1,2)\delta(2,3)+\frac{\delta\Sigma(1,2)}{\delta v(3)}, \qquad (2.93)$$

and write the equation for $\delta G(1,2)/\delta v(3)$ as

$$\frac{\delta G(1,2)}{\delta v(3)} = \int d4\, d5\, G(1,4)\Gamma(45,3)G(5,2). \tag{2.94}$$

By inserting this back into the equations (2.87) and (2.88) we get

$$\begin{aligned}\left\{i\partial_{z_1} - h(1)\right\}G(1,2) &= \delta(1,2) + G(1,2)\int d3\, w(1,3)\langle\hat{n}(3)\rangle \\ &\quad + i\int d3\, d4\, d5\, w(1,3)G(1,4)\Gamma(45,3)G(5,2), \\ &= \delta(1,2) + \int d3\, \Sigma(1,3)G(3,2),\end{aligned} \tag{2.95}$$

and similarly for the adjoint equation

$$\begin{aligned}\left\{-i\partial_{z_2} - h(2)\right\}G(1,2) &= \delta(1,2) + G(1,2)\int d3\, w(2,3)\langle\hat{n}(3)\rangle \\ &\quad + i\int d3\, d4\, d5\, w(2,3)G(1,4)\Gamma(45,3)G(5,2), \\ &= \delta(1,2) + \int d3\, G(1,3)\Sigma(3,2).\end{aligned} \tag{2.96}$$

The self-energy can now be identified as

$$\begin{aligned}\Sigma(1,2) &= -i\delta(1,2)\int d3\, w(1,3)G(3,3^+) + i\int d3\, d4\, G(1,3)w(1,4)\Gamma(32,4), \\ &= -i\delta(1,2)\int d3\, w(1,3)G(3,3^+) + iG(1,2)w(1,2) \\ &\quad + i\int d3\, d4\, G(1,3)w(1,4)\frac{\delta\Sigma(3,2)}{\delta v(4)}, \\ &= \Sigma^{\mathrm{HF}}[G,w](1,2) + i\int d3\, d4\, G(1,3)w(1,4)\frac{\delta\Sigma(3,2)}{\delta v(4)},\end{aligned} \tag{2.97}$$

where $\langle\hat{n}(3)\rangle = -iG(3,3^+)$ and in the last step we denoted the first order terms in w by

$$\Sigma^{\mathrm{HF}}[G,w](1,2) = -i\delta(1,2)\int d3\, w(1,3)G(3,3^+) + iG(1,2)w(1,2). \tag{2.98}$$

These first order terms constitute a *Hartree-Fock* (HF) *approximation* for the electronic self-energy and due to the instantaneous nature of the two-body interaction, $w(1,2) =$

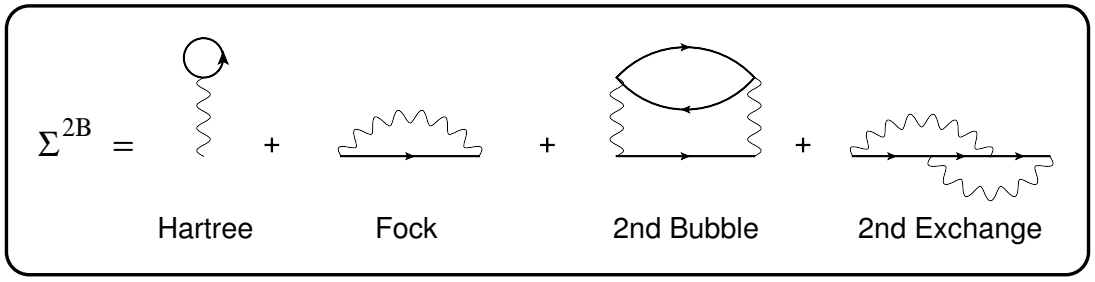

Figure 2.3: HF and 2B self-energy diagrams.

$\delta(t_1,t_2)w(\mathbf{x}_1,\mathbf{x}_2)$, it is a time-local approximation for the electron interactions. The first term describes the classical Hartree potential at 1 produced by the charge density throughout the space and the second term is the space-nonlocal exchange potential originating from the Pauli exclusion principle and the antisymmetry of the wave function. Equation (2.97) provides now an iterative framework to construct higher order approximations for the self-energy by simply evaluating the functional derivatives $\delta\Sigma(3,2)/\delta v(4)$ with the lower order self-energy terms.

The second-order expansion of the self-energy can then be obtained by evaluating $\delta\Sigma^{\rm HF}(1,2)/\delta v(3)$ and inserting it back to the equation (2.97). Keeping only the terms up to w^2 we have the *2nd Born* (2B) *approximation* for the self-energy:

$$\begin{aligned}\Sigma^{\rm 2B}[G,w](1,2) &= \Sigma^{\rm HF}[G,w](1,2) + G(1,2)\int d3\,d4\,w(1,3)w(2,4)G(4,3)G(3,4^+) \\ &\quad - \int d3\,d4\,G(1,3)w(1,4)G(3,4)G(4,2)w(3,2). \qquad (2.99)\end{aligned}$$

The terms appearing in the expansion can be visualized by using the Feynman diagrams as we show in Fig. (2.3). The first second order term in (2.99) corresponds to the bubble diagram and the other term corresponds to the second order exchange diagram. The bubble diagram can be physically interpreted as particle/hole propagation from 2 to 1 and during the propagation, it excites a particle-hole pair, *i.e.*, it polarizes the surrounding medium. The 2B approximation is the simplest approximation to account for correlation effects and it is nonlocal in both space and time variables.

2.5.2 GW approximation

The self-energy expansion (2.97) generates now the different electron interaction processes when the Green function is perturbed with an external potential v. How would the electronic self-energy look like if we would not only consider the changes in the external potential v but also in the Hartree potential produced by the surrounding

medium? To account for the changes in the surrounding charge density, let us consider an effective potential V as a sum of the external potential and the Hartree potential

$$V(1) = v(1) + \int d5\, w(1,5)\langle \hat{n}(5)\rangle. \tag{2.100}$$

We can now use the chain rule

$$\frac{\delta}{\delta v(3)} = \int d4 \frac{\delta V(4)}{\delta v(3)} \frac{\delta}{\delta V(4)}, \tag{2.101}$$

to calculate the change in the Green function due to the change in the total effective field V. The equation of motion (2.87) can then be written

$$\begin{aligned} \left\{ i\partial_{z_1} - h(1) \right\} G(1,2) &= \delta(1,2) + G(1,2) \int d3\, w(1,3)\langle \hat{n}(3)\rangle \\ &\quad + i \int d3\, d4\, w(1,3) \frac{\delta G(1,2)}{\delta V(4)} \frac{\delta V(4)}{\delta v(3)}, \end{aligned} \tag{2.102}$$

where the term $\delta G(1,2)/\delta V(4)$ can be obtained by using the equation (2.94)

$$\begin{aligned} \frac{\delta G(1,2)}{\delta V(4)} &= \int d5 \frac{\delta G(1,2)}{\delta v(5)} \frac{\delta v(5)}{\delta V(4)}, \\ &= \int d5 \left\{ \int d6\, d7\, G(1,6)\Gamma(67,5)G(7,2) \right\} \frac{\delta v(5)}{\delta V(4)}, \\ &= \int d6\, d7\, G(1,6)\tilde{\Gamma}(67,4)G(7,2), \end{aligned} \tag{2.103}$$

where we denoted

$$\tilde{\Gamma}(67,4) = \int d5\, \Gamma(67,5) \frac{\delta v(5)}{\delta V(4)}. \tag{2.104}$$

By inserting (2.103) back to (2.102) we get

$$\begin{aligned} \left\{ i\partial_{z_1} - h(1) \right\} G(1,2) &= \delta(1,2) + G(1,2) \int d3\, w(1,3)\langle \hat{n}(3)\rangle \\ &\quad + i \int d3\, d4\, d6\, d7\, w(1,3) G(1,6)\tilde{\Gamma}(67,4)G(7,2) \frac{\delta V(4)}{\delta v(3)}, \\ &= \delta(1,2) + \int d3\, \Sigma(1,3)G(3,2), \end{aligned} \tag{2.105}$$

where the self-energy can be identified as

$$\begin{aligned}\Sigma(1,2) &= \delta(1,2)\int d5\, w(1,5)\langle\hat{n}(5)\rangle + i\int d3\, d4\, d5\, G(1,5)w(1,3)\frac{\delta V(4)}{\delta v(3)}\tilde{\Gamma}(52,4),\\ &= \underbrace{\delta(1,2)\int d5\, w(1,5)\langle\hat{n}(5)\rangle}_{\Sigma_{\mathrm{H}}(1,2)} + \underbrace{i\int d4\, d5\, G(1,5)W(1,4)\tilde{\Gamma}(52,4)}_{\Sigma_{\mathrm{xc}}(1,2)},\\ &= \Sigma_{\mathrm{H}}(1,2)+\Sigma_{\mathrm{xc}}(1,2). \end{aligned} \tag{2.106}$$

The first term is again the classical Hartree potential (Σ_{H}) and the second part is the exchange-correlation (Σ_{xc}) part of the self-energy. Moreover, in equation (2.106) we also defined

$$W(1,4) = \int d3\, w(1,3)\frac{\delta V(4)}{\delta v(3)}, \tag{2.107}$$

This term is called *screened interaction* because it accounts for the polarization effects of the medium to the effective interaction between the particles as we will see later. Equation (2.107) can be written explicitly by inserting the functional derivative of the total effective field V

$$\begin{aligned} W(1,4) &= w(1,4)+\int d3\, d5\, w(1,3)w(4,5)\frac{\delta\langle\hat{n}(5)\rangle}{\delta v(3)},\\ &= w(1,4)+\int d3\, d5\, d6\, w(1,3)w(4,5)\frac{\delta\langle\hat{n}(5)\rangle}{\delta V(6)}\frac{\delta V(6)}{\delta v(3)},\\ &= w(1,4)+\int d5\, d6\, W(1,6)P(5,6)w(4,5), \end{aligned} \tag{2.108}$$

where we further defined

$$P(1,2)=\frac{\delta\langle\hat{n}(1)\rangle}{\delta V(2)}, \tag{2.109}$$

as the density response at 1 due to the change in the total effective field at 2. Furthermore, P can be related back to $\tilde{\Gamma}$ by employing the equation (2.103) with equal time-indices in the Green function

$$P(1,2)=-i\int d3\, d4\, G(1,3)\tilde{\Gamma}(34,2)G(4,1^{+}). \tag{2.110}$$

We have now obtained the self-energy expansion (2.106), which depends on the screened interaction W (2.108) and $\tilde{\Gamma}$ that can be written explicitly by using the equations (2.93),

(2.100), (2.106) and (2.103)

$$\begin{aligned}\tilde{\Gamma}(12,3) &= \delta(1,2)\delta(2,3)+\frac{\delta\Sigma_{\text{xc}}(1,2)}{\delta V(3)},\\ &= \delta(1,2)\delta(2,3)+\int d4\,d5\,\frac{\delta\Sigma_{\text{xc}}(1,2)}{\delta G(4,5)}\frac{\delta G(4,5)}{\delta V(3)},\\ &= \delta(1,2)\delta(2,3)+\int d4\,d5\,d6\,d7\,\frac{\delta\Sigma_{\text{xc}}(1,2)}{\delta G(4,5)}G(4,6)\tilde{\Gamma}(67,3)G(7,5).\end{aligned} \tag{2.111}$$

Furthermore, the Screened interaction is dependent on the polarization function P (2.110), which again relies on the vertex $\tilde{\Gamma}$ and the Green function. As we already know, the Green function depends on the self-energy through the Dyson equation (2.81) so this set of equations must be solved self-consistently. These equations simplify if we first approximate the the vertex function by first choosing $\Sigma_{\text{xc}}=0$. This gives $\tilde{\Gamma}(12,3)=\delta(1,2)\delta(2,3)$ and the self-consistent equations then become

$$\begin{aligned}\Sigma^{GW}(1,2) &= -i\delta(1,2)\int d3\,w(1,3)G(3,3^{+})+iG(1,2)W(1,2),\\ P(1,2) &= -iG(1,2)G(2,1^{+}),\\ W(1,2) &= w(1,2)+\int d3\,d4\,w(1,3)P(3,4)W(4,2),\\ &= \int d3\,\epsilon^{-1}(1,3)w(3,2),\end{aligned} \tag{2.112}$$

where

$$\epsilon(1,2)=\delta(1,2)+\int d3\,w(1,3)P(3,2),$$

is the *dielectric function*.

The set of equations (2.112) forms the GW approximation for the electronic self-energy and it was originally derived by Hedin [78]. Figure (2.4) illustrates the self-energy and the screened interaction W of GW approximation. The polarization processes described by P are captured by the dielectric function ϵ which modifies (=reduces) the interaction strength between the particles to yield the screened interaction W, much weaker than the bare interaction w. The polarization P describes an elementary process in formation of a Coulomb hole around the test particle by exciting/pushing the surrounding electrons. This particle together with the positively charged screening cloud forms an entity called *quasiparticle* and the interaction between these quasiparticles is described by the screened interaction W [79]. The concept of quasiparticle is valid for any approximation that accounts for nonlocal electron interaction processes, such as the 2B

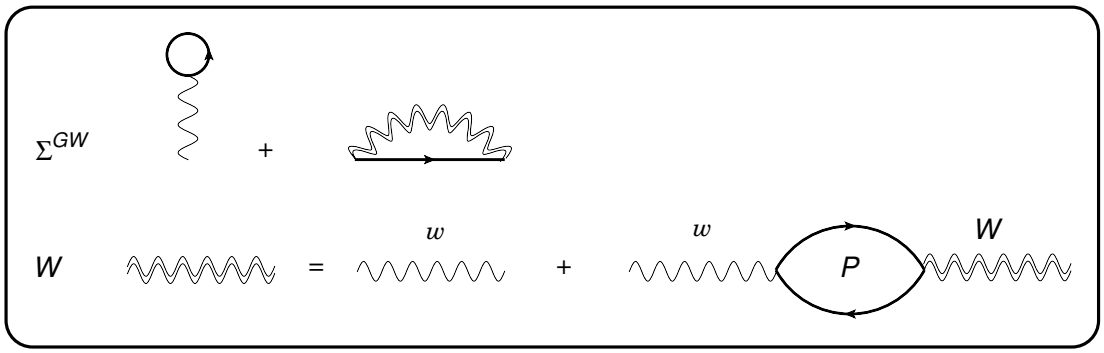

Figure 2.4: GW self-energy and screened interaction diagrams.

approximation. When the self-consistency of equations (2.112) is met, the self-energy then accounts for the mean-field HF diagrams but also an infinite sum of polarization processes provided by W. The GW approximation is often called as dynamically screened Hartree-Fock for their similar form for the self-energy.

2.5.3 Conservation laws and conditions for Σ

The introduction of the self-energy operator (2.72) together with the equations of motion (2.74), (2.75) and the self-consistent approximations (2.98), (2.99) and (2.106) for Σ motivates to look at the conditions that the approximate self-energy must fulfill in order to satisfy the important conservation laws. What are the requirements for the approximate Σ that the particle number, energy, momentum and the angular momentum are conserved as the equations of motion are solved? There is a simple answer to this question and it is provided by Baym [80]. It states that whenever the self-energy is obtained from an underlying gauge-invariant functional Φ as

$$\Sigma[G](1,2) = \frac{\delta\Phi[G]}{\delta G(2,1)}, \tag{2.113}$$

then the above conservation laws are fulfilled. To illustrate this, let us consider the particle number conservation law:

$$\frac{dn(1)}{dt_1} + \nabla_1 \cdot \mathbf{j}(1) = 0, \tag{2.114}$$

where

$$\begin{aligned} n(1) &= \langle \hat{n}(1) \rangle = -iG(1,1^+), \\ \mathbf{j}(1) &= \left\langle \hat{\mathbf{j}}(1) \right\rangle = -\frac{i}{2} \left\langle \left[\hat{\psi}_H^\dagger(1) \left(\nabla_1 \hat{\psi}_H(1) \right) - \left(\nabla_1 \hat{\psi}^\dagger(1) \right) \hat{\psi}(1) \right] \right\rangle, \\ &= -\frac{1}{2} \left\{ \left[\nabla_1 - \nabla_2 \right] G^<(1,2) \right\}_{2=1^+} \end{aligned} \tag{2.115}$$

are the density and current density correspondingly. If we now subtract the adjoint equation of motion (2.75) from (2.74) we obtain a relation

$$\left\{ i\partial_{z_1} + i\partial_{z_2} - h(1) + h(2) \right\} G(1,2) = \int d3 \left\{ \Sigma(1,3)G(3,2) - G(1,3)\Sigma(3.2) \right\}. \tag{2.116}$$

In the limit $2 \to 1^+$ the partial time-derivatives form a total derivative with respect to z_1 and the kinetic energy terms in the one-body Hamiltonians form a total divergence

$$\begin{aligned} \left[h(1) - h(2) \right] G(1,2) &= -\frac{1}{2} \left(\nabla_1 + \nabla_2 \right) \cdot \left(\nabla_1 - \nabla_2 \right) G(1,2), \\ &= \nabla_1 \cdot \left[\left\{ -\frac{1}{2} (\nabla_1 - \nabla_2) G(1,2) \right\}_{2=1^+} \right]. \end{aligned} \tag{2.117}$$

Inserting the equal-time Green function $-iG(1,1^+) = n(1)$ and multiplying both sides with -1 we get

$$\frac{dn(1)}{dt_1} + \nabla_1 \cdot \mathbf{j}(1) = \int d3 \left\{ G(1,3)\Sigma(3.1) - \Sigma(1,3)G(3,1) \right\}. \tag{2.118}$$

In order to satisfy the continuity equation, the right hand side of this equation must vanish. This is indeed true, when the self-energy is obtained from (2.113). To see this, let us first introduce a gauge transformation to the one-body part of the Hamiltonian (2.10)

$$h(1,\Lambda) = \frac{1}{2} \left\{ -i\nabla - \nabla\Lambda(1) \right\}^2 + u(1) - \frac{\partial \Lambda(1)}{\partial t_1}. \tag{2.119}$$

This corresponds to gauge invariance of the external electromagnetic field where the change $\nabla\Lambda(1)$ of the vector potential and simultaneous change $-\partial_{t_1}\Lambda(1)$ of the scalar potential keep the external electric and magnetic fields unchanged. It can be shown that the equations of motion for the field operators (2.66) and (2.67) are invariant in the gauge transformation if we also introduce a phase factor to the field operators, *i.e.*,

$$\begin{aligned} \hat{\psi}_H(1,\Lambda) &= \hat{\psi}_H(1) e^{i\Lambda(1)}, \\ \hat{\psi}_H^\dagger(1,\Lambda) &= \hat{\psi}_H^\dagger(1) e^{-i\Lambda(1)}, \end{aligned} \tag{2.120}$$

with $\Lambda(\mathbf{x}t_0) = \Lambda(\mathbf{x}t_0 - i\beta)$. The transformations (2.119) and (2.120) then yield a gauge transformation for the Green function

$$G(1,2;\Lambda) = e^{i\Lambda(1)}G(1,2)e^{-i\Lambda(2)}, \tag{2.121}$$

which follows directly from the definition of the Green function (2.35). From (2.97) and (2.112) we also see that the gauge transform of the Green function reflects to the self-energy as

$$\Sigma(1,2;\Lambda) = e^{i\Lambda(1)}\Sigma(1,2)e^{-i\Lambda(2)}, \tag{2.122}$$

since the phase factors at the internal vertices cancel in the self-energy. We can now employ the gauge invariance of the functional Φ: The variations of Φ with respect to the gauge field Λ must vanish since $\Phi[\Lambda] = \Phi$, so we have

$$\delta\Phi = \int d1\, d2\, \Sigma(1,2;\Lambda)\delta G(2,1;\Lambda) = 0, \tag{2.123}$$

where $\delta G(2,1;\Lambda)$ is obtained from (2.121) and is given by

$$\delta G(2,1;\Lambda) = i\Big\{\delta\Lambda(2) - \delta\Lambda(1)\Big\}G(2,1;\Lambda). \tag{2.124}$$

Inserting this back to the equation (2.123) and using the explicit forms (2.121) and (2.122) we obtain

$$\begin{aligned}
\delta\Phi &= i\int d1\, d2\, \Sigma(1,2)\Big\{\delta\Lambda(2) - \delta\Lambda(1)\Big\}G(2,1), \\
&= i\int d1\, d2\, \Big\{G(1,2)\Sigma(2,1) - \Sigma(1,2)G(2,1)\Big\}\delta\Lambda(1), \\
&= 0.
\end{aligned} \tag{2.125}$$

Now, since Λ is an arbitrary scalar function, it must be that

$$\int d2\, \Big\{G(1,2)\Sigma(2,1) - \Sigma(1,2)G(2,1)\Big\} = 0, \tag{2.126}$$

and we then recover the continuity equation from (2.118)

$$\frac{dn(1)}{dt_1} + \nabla_1 \cdot \mathbf{j}(1) = 0. \tag{2.127}$$

To conclude, the results of this analysis was that the particle number is conserved if the approximate self-energy is obtained from the gauge invariant functional Φ via the relation (2.113). It can be proved that by obtaining the self-energy from (2.113), also the other conservation laws are automatically fulfilled, which makes these self-energy approximation physically relevant. The self-energies (2.113) are then said to be Φ-*derivable* self-energies.

The gauge invariant Φ-functional can be obtained, as showed by Luttinger and Ward [81], by closing the irreducible self-energy diagrams with a Green function line and multiplying the closed diagram with suitable numerical constants to avoid multiple counting of resulting self-energy diagrams. The closing of the self-energy diagrams with a Green function makes the resulting object gauge invariant as each of the gauge factors will cancel at the vertices. The explicit form for the Φ-functional is given by

$$\Phi[G] = \sum_{n,k} \frac{1}{2n} \mathrm{tr}_C \left\{ \Sigma_k^{(n)} G \right\}, \tag{2.128}$$

where n denotes the number of interaction lines, k enumerates the different n'th order self-energy diagrams and the trace means integration of all the internal vertex variables over the Keldysh contour C.

3 NEGF Formalism In Time-Dependent Quantum Transport

In the previous section we derived the Kadanoff-Baym equations for the correlated and isolated systems. Let us now turn our attention to open quantum systems and generalize the Kadanoff-Baym equations to multi-terminal quantum transport setups. We first introduce the model Hamiltonians suitable for a quantitative analysis of transport through simple molecular systems. As a follow-up, the essential concepts such as lead self-energies are discussed and the essential equations related to the quantities of interest are demonstrated.

3.1 Pariser-Parr-Pople model Hamiltonian

The approximative numerical methods and models always demand assumptions on the underlying physical system. In this work we focus on qualitative description of the time-dependent quantum transport and the transport properties through simple atomic chains and molecular systems and for this purpose we need a suitable model description for the many-body Hamiltonian (2.10). One of the popular model descriptions is provided by the Pariser-Parr-Pople (PPP) model [82, 83], originally designed to provide accurate description of the low-energy properties of π-conjugated systems, such as polymers and other carbon-backboned molecules. In the PPP model it is assumed that the chemical and physical properties of the conjugated nanostructures are primarily determined by the delocalized π-orbitals. The π-orbitals are formed when the atomic $2p_z$ orbitals overlap and hybridize while the "core" formed by the $1s$ orbitals and the hybridized sp^2 orbitals (the σ-bonds) are kept frozen. This assumption motivates us to consider each atomic site k having one localized spin-orbital $\phi_{k\bar{\sigma}}(\mathbf{r}\sigma) = \delta_{\bar{\sigma}\sigma}\,\phi_k(\mathbf{r})$ with a small but finite overlap ε with the nearest neighbor orbitals [75]

$$\begin{aligned}[\mathbf{S}]_{kl} &= \int d\mathbf{x}\,\phi^*_{k\sigma}(\mathbf{x})\phi_{l\sigma}(\mathbf{x}), \\ &= \begin{cases} 1 & k = l \\ \varepsilon & k \text{ and } l \text{ nearest neighbours} := \langle k,l\rangle \end{cases}\end{aligned} \tag{3.1}$$

where $\mathbf{S} = \mathbf{1} + \boldsymbol{\varepsilon}$ is the overlap matrix. Even the functions $\phi_{k\bar{\sigma}}(\mathbf{x})$ do not form an orthogonal basis, we can construct one by using $\mathbf{S}$

$$\begin{aligned} \varphi_{k\bar{\sigma}}(\mathbf{x}) &= \sum_l \phi_{l\bar{\sigma}}(\mathbf{x})[\mathbf{S}]^{-1/2}_{lk}, \qquad (3.2) \\ &\approx \sum_l \phi_{l\bar{\sigma}}(\mathbf{x}) \left[\mathbf{1} - \frac{\boldsymbol{\varepsilon}}{2}\right]_{lk}, \\ &= \phi_{k\bar{\sigma}}(\mathbf{x}) - \frac{\varepsilon}{2}\phi_{k-1\bar{\sigma}}(\mathbf{x}) - \frac{\varepsilon}{2}\phi_{k+1\bar{\sigma}}(\mathbf{x}), \qquad (3.3) \end{aligned}$$

where in the second step we expanded $\mathbf{S}^{-1/2}$ into linear order in ε. It can be easily checked from (3.2) that the new orbitals $\varphi_{k\bar{\sigma}}(\mathbf{x})$ form an orthonormal basis which is still localized, but slightly spread out over the nearest neighbor sites.

We can now use this *finite* basis to expand the creation and annihilation operators in the following way

$$\begin{aligned} \hat{\psi}(\mathbf{x}) &= \sum_{k,\sigma'} \varphi_{k\sigma'}(\mathbf{x})\hat{a}_{k\sigma'}, \qquad (3.4) \\ \hat{\psi}^\dagger(\mathbf{x}) &= \sum_{k,\sigma'} \varphi^*_{k\sigma'}(\mathbf{x})\hat{a}^\dagger_{k\sigma'}, \qquad (3.5) \end{aligned}$$

where the $\hat{a}_{k\sigma}$ and $\hat{a}^\dagger_{k\sigma}$ annihilate and create electron to lattice site k with spin σ correspondingly and they obey the anti-commutation rules

$$\begin{aligned} \left\{\hat{a}^\dagger_{i\sigma}, \hat{a}_{j\sigma'}\right\} &= \delta_{ij}\delta_{\sigma\sigma'} \\ \left\{\hat{a}^{(\dagger)}_{i\sigma}, \hat{a}^{(\dagger)}_{j\sigma'}\right\} &= 0. \qquad (3.6) \end{aligned}$$

If we now focus on the spin compensated system with $\varphi_{k\sigma'}(\mathbf{x}) = \delta_{\sigma\sigma'}\varphi_k(\mathbf{r})$ and use the above expansions for the field operators, we can write the second quantized Hamiltonian (2.10) in a lattice basis as

$$\hat{H}(t) = \sum_{ij}\sum_{\sigma} h_{ij}(t)\,\hat{a}^\dagger_{i\sigma}\hat{a}_{j\sigma} + \frac{1}{2}\sum_{ijkl}\sum_{\sigma\sigma'} w_{ijkl}\,\hat{a}^\dagger_{i\sigma}\hat{a}^\dagger_{j\sigma'}\hat{a}_{k\sigma'}\hat{a}_{l\sigma}, \qquad (3.7)$$

where the matrix elements of the one and two-body parts in the general PPP basis $\varphi_i(\mathbf{r})$ are then given by

$$\begin{aligned} h_{ij}(t) &= \int d\mathbf{r}\,\varphi^*_i(\mathbf{r})h(\mathbf{r},t)\varphi_j(\mathbf{r}), \\ w_{ijkl} &= \int d\mathbf{r}\,d\mathbf{r}'\,\varphi^*_i(\mathbf{r})\varphi^*_j(\mathbf{r}')w(\mathbf{r},\mathbf{r}')\varphi_k(\mathbf{r}')\varphi_l(\mathbf{r}). \qquad (3.8) \end{aligned}$$

with $h(\mathbf{r},t)$ the *spin-independent* one-body part of the Hamiltonian

$$h(\mathbf{r},t) = -\frac{1}{2}\nabla^2 - \sum_k Z_k w(\mathbf{r},\mathbf{R}_k) + u(\mathbf{r},t), \tag{3.9}$$

with Z_k the *effective* positive charge of nucleus k screened by the frozen core-electrons. Since the basis functions are localized around each atomic site, we can now retain only the main local and nonlocal contributions from h_{ij} by neglecting all the other than nearest neighbor terms. In the similar fashion, for the two-body part w_{ijkl}, we account only those nonlocal terms which describe the interaction between the two localized charge clouds at different atomic sites, *i.e.*, we set $w_{ijkl} \approx \delta_{il}\delta_{jk}w_{ij}$, where $w_{ij} \sim 1/|\mathbf{R}_i - \mathbf{R}_j|$ is the long-range behavior of the interaction matrix elements for $i \neq j$. We can therefore write the lattice Hamiltonian as

$$\hat{H}(t) = \sum_{ij}\sum_{\sigma} h_{ij}(t)\,\hat{a}^{\dagger}_{i\sigma}\hat{a}_{j\sigma} + \frac{1}{2}\sum_{ij}\sum_{\sigma\sigma'} w_{ij}\,\hat{a}^{\dagger}_{i\sigma}\hat{a}^{\dagger}_{j\sigma'}\hat{a}_{j\sigma'}\hat{a}_{i\sigma} + \frac{1}{2}\sum_{ij} w_{ij}Z_iZ_j, \tag{3.10}$$

$$= \sum_i \epsilon_i(t)\,\hat{n}_i + \sum_{\langle i,j\rangle}\sum_{\sigma} h_{ij}\,\hat{a}^{\dagger}_{i\sigma}\hat{a}_{j\sigma} + \sum_i w_{ii}\hat{n}_{i\uparrow}\hat{n}_{i\downarrow} + \frac{1}{2}\sum_{i\neq j} w_{ij}\,(\hat{n}_i - Z_i)(\hat{n}_j - Z_j), \tag{3.11}$$

where $\frac{1}{2}\sum_{ij} w_{ij}Z_iZ_j$ is just an added constant in the Hamiltonian due to the effective interaction between the nuclei[1], $\hat{n}_i = \sum_\sigma \hat{n}_{i\sigma}$ and the matrix elements are denoted as

$$h_{ij}(t) = \begin{cases} \epsilon_i(t) = \epsilon_i - \sum_{k\neq i} Z_k w_{ik} + W_i(t) & i = j \\ h_{ij} \equiv b & \langle i,j\rangle \end{cases} \tag{3.12}$$

Here ϵ_i is the diagonal expectation value of kinetic energy operator plus the local positive background

$$h_{ii} = \epsilon_i = \int d\mathbf{r}\,\varphi_i^*(\mathbf{r})\Big\{-\frac{\nabla^2}{2} - Z_i w(\mathbf{r},\mathbf{R}_i)\Big\}\varphi_i(\mathbf{r}) \tag{3.13}$$

and it is often called as the *on-site energy* in the nearest neighbor approximation. The diagonal potential terms are then affected by the effective background due to the surrounding ionic lattice, $\sum_{k\neq i} Z_k w_{ik}$ and the time-dependent external potential

$$W^i(t) = \int d\mathbf{r}\,\varphi_i^*(\mathbf{r})u(\mathbf{r},t)\varphi_i(\mathbf{r}), \tag{3.14}$$

which we consider as *local* potential for simplicity. Moreover, the off-diagonal terms are denoted by time-independent elements h_{ij} which are called the *hopping* parameters.

[1]This quantity is added in order to have the second form of the Hamiltonian and does not have a physical significance in this context.

These matrix elements allows the lattice sites to share kinetic energy by tunneling the particles between the neighboring sites. Let us from now on call the nearest neighbor approximation as *tight binding* (TB) approximation. The Hamiltonians (3.10) and (3.11) now serve as starting points for modeling lattice systems and especially investigating the quantum transport system.

3.2 Basis representation of G and Σ

By the definition of the localized basis (3.2) and the representations for the field operators (3.4) and (3.5), it is also necessary to have the lattice representations for the Green function $G(1,2)$ and the self-energies $\Sigma(1,2)$. We can write the expansions in the following way

$$\begin{aligned} G(1,2) &= G(\mathbf{x}_1 z_1, \mathbf{x}_2 z_2) \\ &= \sum_{kl} \varphi_k^*(\mathbf{x_1})\varphi_l(\mathbf{x_2}) G_{kl}(z_1,z_2), \end{aligned} \tag{3.15}$$

$$\begin{aligned} \Sigma(1,2) &= \Sigma(\mathbf{x}_1 z_1, \mathbf{x}_2 z_2) \\ &= \sum_{kl} \varphi_k^*(\mathbf{x_1})\varphi_l(\mathbf{x_2}) \Sigma_{kl}(z_1,z_2), \end{aligned} \tag{3.16}$$

where the indices k,l encapsulate both the spatial and spin degrees of freedom. Here the components $G_{kl}(z_1,z_2)$ are simply given by the time-ordered product of creation and annihilation operators[2] $\hat{a}_l^\dagger(z_2)$ and $\hat{a}_k(z_1)$

$$G_{kl}(z_1,z_2) = -i \left\langle \mathscr{T}\left[\hat{a}_k(z_1)\hat{a}_l^\dagger(z_2)\right]\right\rangle . \tag{3.17}$$

Just like in the position-spin representation, we can define the lesser and greater Green functions in the lattice as

$$G_{kl}^<(z_1,z_2) = +i \left\langle \hat{a}_l^\dagger(z_2)\hat{a}_k(z_1)\right\rangle , \tag{3.18}$$

$$G_{kl}^>(z_1,z_2) = -i \left\langle \hat{a}_k(z_1)\hat{a}_l^\dagger(z_2)\right\rangle . \tag{3.19}$$

It is now straightforward to calculate the explicit expressions for the Hartree-Fock, Second Born and GW self-energies in the lattice PPP-basis. The self-energy components are

[2]We neglect the subscript H referring to Heisenberg picture from the lattice field operators.

given by

$$\text{(HF)} \quad \Sigma^{\text{HF}}_{ij}(z_1,z_2) = \Sigma^{\delta}_{ij}(z_1,z_2), \\ = \delta(z_1,z_2)\Big\{\delta_{ij}\sum_k w_{ik}\rho_{kk}(z_1) - w_{ij}\rho_{ij}(z_1)\Big\}, \tag{3.20}$$

$$\text{(2B)} \quad \Sigma^{\text{2B}}_{ij}(z_1,z_2) = \Sigma^{\text{HF}}_{ij}(z_1,z_2) + G_{ij}(z_1,z_2)\sum_{kl} w_{ik}w_{jl}G_{lk}(z_2,z_1)G_{kl}(z_1,z_2) \\ -\sum_{kl} w_{il}\,w_{kj}\,G_{ik}(z_1,z_2)G_{kl}(z_2,z_1)G_{lj}(z_1,z_2), \tag{3.21}$$

$$\text{(GW)} \quad \Sigma^{GW}_{ij}(z_1,z_2) = \Sigma^{\text{H}}_{ij}(z_1,z_2) + iG_{ij}(z_1,z_2)W_{ij}(z_1,z_2), \tag{3.22}$$

where $\rho_{ij}(z_1) = -iG^{<}_{ij}(z_1,z_1^+)$ is the density matrix and

$$\Sigma^{\text{H}}_{ij}(z_1,z_2) = \delta(z_1,z_2)\delta_{ij}\sum_k w_{ik}\rho_{kk}(z_1), \tag{3.23}$$

is the Hartree-part of the self-energy and

$$W_{ij}(z_1,z_2) = w_{ij}\delta(z_1,z_2) + \sum_{kl} w_{ik}\int P_{kl}(z_1,\bar{z})W_{lj}(\bar{z},z_2)d\bar{z}, \tag{3.24}$$

$$P_{kl}(z_1,z_2) = -iG_{kl}(z_1,z_2)G_{lk}(z_2,z_1), \tag{3.25}$$

are the screened interaction and the polarization function.

3.3 Quantum transport Hamiltonian

Modeling the two-terminal transport in nanostructures has become one of the most popular subjects in computational and theoretical nanophysics. A typical quantum transport system consists of two macroscopic and metallic electron reservoirs (leads) and a significantly smaller scattering region (for example, a quantum dot, quantum wire, or a molecular system) which is squeezed between the two reservoirs, see Fig. (3.1) for the topology of this system. The model Hamiltonian operator describing this two-terminal quantum transport setup is usually written in three different pieces as

$$\hat{H}(t) = \hat{H}_C(t) + \hat{H}_{leads}(t) + \hat{H}_T - \mu\hat{N}. \tag{3.26}$$

Here, the first part is the Hamiltonian for the central region, *i.e.*, the model description for a quantum dot, quantum wire or a molecule. Within the notation of second quantization, it has the expression as Eq. (3.10)

$$\hat{H}_C(t) = \sum_{i,j\in C}\sum_{\sigma} h_{ij}(t)\hat{d}^{\dagger}_{i\sigma}\hat{d}_{j\sigma} + \frac{1}{2}\sum_{\substack{ij\\ \sigma\sigma'}} w_{ij}\,\hat{d}^{\dagger}_{i\sigma}\hat{d}^{\dagger}_{j\sigma'}\hat{d}_{j\sigma'}\hat{d}_{i\sigma}, \tag{3.27}$$

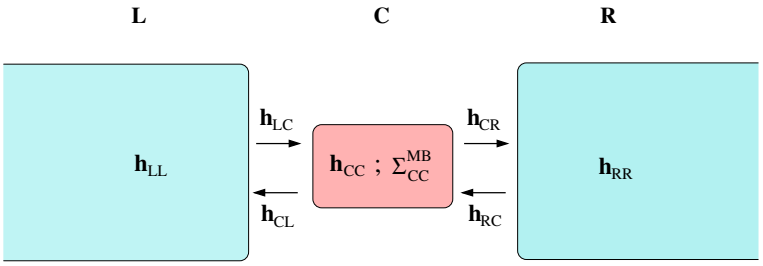

Figure 3.1: Schematic view of the quantum transport setup: The Correlated central region (C) is coupled to the left (L) and right (R) metallic electrodes via tunneling Hamiltonians $H_{\alpha C}$ and $H_{C\alpha}$, α =L,R.

where again the indices i and j label the atomic sites in the central region, σ and σ' are the spin-indices and $h_{ij}(t)$ is the one-body part of the central region Hamiltonian with the nearest neighbor parametrization. Furthermore, $\hat{d}^{\dagger}_{i\sigma}$ and $\hat{d}_{i\sigma}$ are the electron creation and annihilation operators for the central (C), often referred as *device*, region and the two-body matrix elements w_{ij} are the electron-electron interactions within the C-subspace. We choose the interaction matrix elements in the following way

$$w_{ij} = \begin{cases} w_{ii} & i = j \\ \frac{w_{ii}}{2|i-j|} & i \neq j \end{cases} \tag{3.28}$$

which is suitable for systems with chain topology. The second part in eq. (3.26) is the Hamiltonian for the *semi-infinite* leads and it attains the form

$$\hat{H}_{leads}(t) = \sum_{\alpha=L,R} \sum_{i,j\in\alpha}^{\infty} \sum_{\sigma} \left[h^{\alpha}_{ij} + W^{\alpha}(t)\delta_{ij} \right] \hat{c}^{\dagger}_{i\sigma\alpha}\hat{c}_{j\sigma\alpha}, \tag{3.29}$$

where h^{α}_{ij} is the nearest neighbor Hamiltonian of the lead $\alpha = L,R$. Moreover, $\hat{c}^{\dagger}_{i\sigma\alpha}$ and $\hat{c}_{j\sigma\alpha}$ are the creation and annihilation operators for the lead α and $W^{\alpha}(t)$ is the time-dependent local potential applied to the lead α, *i.e*, the bias voltage. In this model we assume that the bias voltage, generated by applying an electric field over the system, is simply a homogeneous potential shift in the leads: The external electric field is assumed to be screened instantly due to the generated Hartree-field.

The third part in the full Hamiltonian (3.26) describes the physical contacts or couplings between the central region and the leads. The explicit expression for this tunneling Hamiltonian is

$$\hat{H}_T = \sum_{\alpha=L,R} \sum_{\substack{i\in C \\ j\in\alpha}} \sum_{\sigma} V_{i,j\alpha} \left[\hat{d}^{\dagger}_{i\sigma}\hat{c}_{j\sigma\alpha} + \hat{c}^{\dagger}_{j\sigma\alpha}\hat{d}_{i\sigma} \right], \tag{3.30}$$

where $V_{i,j\alpha}$ are the matrix elements of the coupling Hamiltonian. Finally we have reduced from the Hamiltonian the chemical potential μ coupled to the total particle number operator $\hat{N} = \hat{N}_C + \sum_{\alpha}\hat{N}_{\alpha}$. Next we shall proceed to investigate the equations of

motion for the Green function in this semi-infinite transport lattice and extend them to treat continuum systems.

3.4 Embedded Kadanoff-Baym equations

The quantum transport Hamiltonian (3.26) describes now an infinite system with the electron-electron interactions limited to C-subspace and the direct implementation of the equations of motion for this Hamiltonian is practically impossible. However, due to the restricted domain of the w_{ij} -elements, we can contract the Hilbert space of the infinite site lattice to the interacting domain only. Let us start from the equation of motion for the one-particle Green function, which in the site basis representation reads

$$\Big\{i\partial_z - \mathbf{h}(z)\Big\}\mathbf{G}(z,z') = \mathbf{1}\delta(z,z') + \int d\bar{z}\mathbf{\Sigma}^{\mathrm{MB}}(z,\bar{z})\mathbf{G}(\bar{z},z'), \tag{3.31}$$

$$\Big\{-i\partial_{z'} - \mathbf{h}(z')\Big\}\mathbf{G}(z,z') = \mathbf{1}\delta(z,z') + \int d\bar{z}\mathbf{G}(z,\bar{z})\mathbf{\Sigma}^{\mathrm{MB}}(\bar{z},z'). \tag{3.32}$$

Here the one-body Hamiltonian, the many-body self-energy and the Green function have been written in the block matrix form as

$$\mathbf{h} = \begin{bmatrix} \mathbf{h}_{\mathrm{LL}} & \mathbf{h}_{\mathrm{LC}} & \mathbf{0} \\ \mathbf{h}_{\mathrm{CL}} & \mathbf{h}_{\mathrm{CC}} & \mathbf{h}_{\mathrm{CR}} \\ \mathbf{0} & \mathbf{H}_{\mathrm{RC}} & \mathbf{h}_{\mathrm{RR}} \end{bmatrix}, \mathbf{\Sigma}^{\mathrm{MB}} = \begin{bmatrix} \mathbf{0} & \mathbf{0} & \mathbf{0} \\ \mathbf{0} & \mathbf{\Sigma}^{\mathrm{MB}}_{\mathrm{CC}} & \mathbf{0} \\ \mathbf{0} & \mathbf{0} & \mathbf{0} \end{bmatrix}, \mathbf{G} = \begin{bmatrix} \mathbf{G}_{\mathrm{LL}} & \mathbf{G}_{\mathrm{LC}} & \mathbf{G}_{\mathrm{LR}} \\ \mathbf{G}_{\mathrm{CL}} & \mathbf{G}_{\mathrm{CC}} & \mathbf{G}_{\mathrm{CR}} \\ \mathbf{G}_{\mathrm{RL}} & \mathbf{G}_{\mathrm{RC}} & \mathbf{G}_{\mathrm{RR}} \end{bmatrix}, \tag{3.33}$$

where the subscripts refer to the matrix indices in different subspaces, such as CC = $\{i,j\} \in$ C or LC = $\{i \in \mathrm{L}, j \in \mathrm{C}\}$ and the lattice Green function is given by

$$G_{kl}(z,z') = -i\delta_{\sigma_k,\sigma_l}\frac{\mathrm{Tr}\left\{\mathscr{T}_C\left[e^{-i\int \hat{H}(\bar{z})d\bar{z}}\hat{a}_{k\sigma_k}(z)\hat{a}^{\dagger}_{l\sigma_l}(z')\right]\right\}}{\mathrm{Tr}\left\{e^{-i\int \hat{H}(\bar{z})d\bar{z}}\right\}}. \tag{3.34}$$

where we have explicitly written the spin indices σ_i. Since the Hamiltonian is invariant upon the rotations in spin-space, also the Green function is diagonal in the spin indices.

The equations of motion (3.31) and (3.32) can be cast into equivalent Dyson equations by expanding the full interacting and connected Green function $\mathbf{G}(z,z')$ in terms of disconnected and noninteracting Green function $\mathbf{g}(z,z')$ which obeys the equation of motion

$$\Big\{i\partial_z - \mathbf{h}^{\mathrm{d}}(z)\Big\}\mathbf{g}(z,z') = \mathbf{1}\delta(z,z'), \tag{3.35}$$

where $\mathbf{h}^{\mathrm{d}}(z)$ is the diagonal part of the total one-body Hamiltonian in (3.33). By separating the off-diagonal contributions $\mathbf{h}^{\mathrm{o}}$ of the one-body Hamiltonian, $\mathbf{h}(z) = \mathbf{h}^{\mathrm{d}}(z) + \mathbf{h}^{\mathrm{o}}$ and using (3.35) we get

$$\mathbf{G}(z,z') = \mathbf{g}(z,z') + \int \mathbf{g}(z,\bar{z})\,\mathbf{h}^{\mathrm{o}}\,\mathbf{G}(\bar{z},z')\,d\bar{z} + \int \mathbf{g}(z,\bar{z})\,\mathbf{\Sigma}^{\mathrm{MB}}(\bar{z},\bar{\bar{z}})\,\mathbf{G}(\bar{\bar{z}},z')\,d\bar{z}\,d\bar{\bar{z}}, \tag{3.36}$$

$$= \mathbf{g}(z,z') + \int \mathbf{G}(z,\bar{z})\,\mathbf{h}^{\mathrm{o}}\,\mathbf{g}(\bar{z},z')\,d\bar{z} + \int \mathbf{G}(z,\bar{z})\,\mathbf{\Sigma}^{\mathrm{MB}}(\bar{z},\bar{\bar{z}})\,\mathbf{g}(\bar{\bar{z}},z')\,d\bar{z}\,d\bar{\bar{z}}, \tag{3.37}$$

By projecting the equation of motion (3.31) into CC subspace,

$$\Big\{i\partial_z - \mathbf{h}_{\mathrm{CC}}(z)\Big\}\mathbf{G}_{\mathrm{CC}}(z,z') = \mathbf{1}\delta(z,z') + \int d\bar{z}\mathbf{\Sigma}^{\mathrm{MB}}_{\mathrm{CC}}(z,\bar{z})\mathbf{G}_{\mathrm{CC}}(\bar{z},z') + \sum_{\alpha=L,R}\mathbf{h}_{\mathrm{C}\alpha}\mathbf{G}_{\alpha\mathrm{C}}(z,z'), \tag{3.38}$$

and using the αC-projection of (3.36)

$$\mathbf{G}_{\alpha\mathrm{C}}(z,z') = \int \mathbf{g}_{\alpha\alpha}(z,\bar{z})\mathbf{h}_{\alpha\mathrm{C}}\mathbf{G}_{\mathrm{CC}}(\bar{z},z'), \tag{3.39}$$

we obtain a closed equation of motion for the one-particle Green function *projected on the central region*

$$\Big\{i\partial_z - \mathbf{h}_{\mathrm{CC}}(z)\Big\}\mathbf{G}_{\mathrm{CC}}(z,z') = \mathbf{1}\delta(z,z') + \int d\bar{z}\,\Big[\mathbf{\Sigma}^{\mathrm{MB}}_{\mathrm{CC}} + \mathbf{\Sigma}_{\mathrm{em,CC}}\Big](z,\bar{z})\mathbf{G}_{\mathrm{CC}}(\bar{z},z'). \tag{3.40}$$

Similarly, for the adjoint equation of motion one obtains

$$\Big\{-i\partial'_z - \mathbf{h}_{\mathrm{CC}}(z')\Big\}\mathbf{G}_{\mathrm{CC}}(z,z') = \mathbf{1}\delta(z,z') + \int d\bar{z}\,\mathbf{G}_{\mathrm{CC}}(z,\bar{z})\Big[\mathbf{\Sigma}^{\mathrm{MB}}_{\mathrm{CC}} + \mathbf{\Sigma}_{\mathrm{em,CC}}\Big](\bar{z},z'). \tag{3.41}$$

Here we introduced the *embedding self-energy*

$$\mathbf{\Sigma}_{\mathrm{em,CC}}(z,z') = \sum_{\alpha=L,R}\mathbf{h}_{\mathrm{C}\alpha}\mathbf{g}_{\alpha\alpha}(z,z')\mathbf{h}_{\alpha\mathrm{C}}, \tag{3.42}$$

accounting for the time-dependent effects of the leads, encapsulated by $\mathbf{g}_{\alpha\alpha}(z,z')$, to the central region via the tunneling Hamiltonians $\mathbf{h}_{\mathrm{C}\alpha}$ and $\mathbf{h}_{\alpha\mathrm{C}}$. We see that the equation of motion (3.40) is exactly of similar form as if C would be a closed system, but the self-energy is just replaced with the summation of the many-body self-energy and the embedding self-energy. We are then able to employ the implementation of the Kadanoff-Baym equations for closed systems in both ground-state [84, 73] and

in non-equilibrium [85]. The only difference of solving the embedded Kadanoff-Baym equations for the transport setup is the selection for the basis, which in this case is chosen to be the site basis for the PPP model system. It is worth noting that the embedded equation of motion (3.40) can, in principle, handle arbitrary number of terminals α with each having unique coupling matrices $\mathbf{h}_{\alpha\mathrm{C}}$ and $\mathbf{h}_{\mathrm{C}\alpha}$ to the scattering region and also unique internal structure and time-dependence determined by the lead Green functions $\mathbf{g}_{\alpha\alpha}(z,z')$.

The solution of the equations (3.40) and (3.41) in the ground-state and in the time-domain provides an access to the important time-dependent and steady-state properties of the system through the two-time Green function $\mathbf{G}_{\mathrm{CC}}(z,z')$. For example, the time-dependent total particle number in C is given by

$$N_{\mathrm{C}}(t) = -i\,\mathrm{Tr}_{\mathrm{C}}\Big\{\mathbf{G}_{\mathrm{CC}}(t,t^{+})\Big\}, \tag{3.43}$$

where the trace is taken over all the localized one-particle states (site-indices) of the central region.

3.5 Equations of motion on the Keldysh contour

Projection	$\mathbf{c}(z,z') = \int \mathbf{a}(z,\bar{z})\mathbf{b}(\bar{z},z')d\bar{z}$	$\mathbf{c}(z,z') = \mathbf{a}(z,z')\mathbf{b}(z',z)$
$\mathbf{c}^{>}(t,t')$	$\mathbf{c}^{>} = \mathbf{a}^{>}\cdot\mathbf{b}^{A} + \mathbf{a}^{R}\cdot\mathbf{b}^{>} + \mathbf{a}^{\rceil}\star\mathbf{b}^{\lceil}$	$\mathbf{c}^{>} = \mathbf{a}^{>}\cdot\mathbf{b}^{<}$
$\mathbf{c}^{<}(t,t')$	$\mathbf{c}^{<} = \mathbf{a}^{<}\cdot\mathbf{b}^{A} + \mathbf{a}^{R}\cdot\mathbf{b}^{<} + \mathbf{a}^{\rceil}\star\mathbf{b}^{\lceil}$	$\mathbf{c}^{<} = \mathbf{a}^{<}\cdot\mathbf{b}^{>}$
$\mathbf{c}^{R}(t,t')$	$\mathbf{c}^{R} = \mathbf{a}^{R}\cdot\mathbf{b}^{R}$	$\mathbf{c}^{R} = \begin{cases}\mathbf{a}^{R}\cdot\mathbf{b}^{<} + \mathbf{a}^{<}\cdot\mathbf{b}^{A}\\ \mathbf{a}^{R}\cdot\mathbf{b}^{>} + \mathbf{a}^{>}\cdot\mathbf{b}^{A}\end{cases}$
$\mathbf{c}^{A}(t,t')$	$\mathbf{c}^{A} = \mathbf{a}^{A}\cdot\mathbf{b}^{A}$	$\mathbf{c}^{A} = \begin{cases}\mathbf{a}^{A}\cdot\mathbf{b}^{<} + \mathbf{a}^{<}\cdot\mathbf{b}^{R}\\ \mathbf{a}^{A}\cdot\mathbf{b}^{>} + \mathbf{a}^{>}\cdot\mathbf{b}^{R}\end{cases}$
$\mathbf{c}^{\rceil}(t,\tau)$	$\mathbf{c}^{\rceil} = \mathbf{a}^{R}\cdot\mathbf{b}^{\rceil} + \mathbf{a}^{\rceil}\star\mathbf{b}^{M}$	$\mathbf{c}^{\rceil} = \mathbf{a}^{\rceil}\mathbf{b}^{\lceil}$
$\mathbf{c}^{\lceil}(\tau,t)$	$\mathbf{c}^{\lceil} = \mathbf{a}^{\lceil}\cdot\mathbf{b}^{A} + \mathbf{a}^{M}\star\mathbf{b}^{\lceil}$	$\mathbf{c}^{\lceil} = \mathbf{a}^{\lceil}\mathbf{b}^{\rceil}$
$\mathbf{c}^{M}(\tau,\tau')$	$\mathbf{c}^{M} = \mathbf{a}^{M}\star\mathbf{b}^{M}$	$\mathbf{c}^{M} = \mathbf{a}^{M}\mathbf{b}^{M}$

Table 3.1: The Langreth rules for extracting the different Keldysh contour projections for convolution integrals and product functions.

The equations of motion (3.40) and (3.41) now serve as the starting points for the kinetic equations on the Keldysh contour. The equations of motion together with the self-consistent and conserving self-energy approximations (3.20), (3.21) and (3.22) form now a closed set of integro-differential equations. The right hand side of the equations of motion contains the convolution integral of the self-energy with the Green function.

As we have already seen, the Green function and, consequently, the self-energy have different components depending on the relative order of the field operators. The contour integration is then performed with the functions

$$\begin{aligned}\mathbf{\Sigma}(z_1,z_2) &= \delta(z_1,z_2)\mathbf{\Sigma}^{\delta}(z_1,z_2)+\theta(z_1,z_2)\mathbf{\Sigma}^{>}(z_1,z_2)+\theta(z_2,z_1)\mathbf{\Sigma}^{<}(z_1,z_2), \quad (3.44)\\ \mathbf{G}(z_1,z_2) &= \theta(z_1,z_2)\mathbf{G}^{>}(z_1,z_2)+\theta(z_2,z_1)\mathbf{G}^{<}(z_1,z_2), \quad (3.45)\end{aligned}$$

where $\mathbf{\Sigma} = \mathbf{\Sigma}_{\rm em} + \mathbf{\Sigma}_{\rm MB}$ and $\mathbf{\Sigma}^{\delta}(z_1,z_2)$ is the time-local part of the self-energy. These functions belong to the Keldysh space where the contour integrals split into several components according to the *Langreth rules* [86, 31] shown in the table (3.1). By employing the integration rules to the equations of motion (3.40) and (3.41), we obtain for the real-time Green functions

$$\begin{aligned}i\partial_{t_1}\mathbf{G}^{\lessgtr}(t_1,t_2) &= \mathbf{h}(t_1)\mathbf{G}^{\lessgtr}(t_1,t_2)+\left[\mathbf{\Sigma}^{R}\cdot\mathbf{G}^{\lessgtr}+\mathbf{\Sigma}^{\lessgtr}\cdot\mathbf{G}^{A}+\mathbf{\Sigma}^{\rceil}\star\mathbf{G}^{\lceil}\right](t_1,t_2), \quad (3.46)\\ &= \mathbf{h}(t_1)\mathbf{G}^{\lessgtr}(t_1,t_2)+\mathbf{I}_1^{\lessgtr}(t_1,t_2)\end{aligned}$$

$$\begin{aligned}-i\partial_{t_2}\mathbf{G}^{\lessgtr}(t_1,t_2) &= \mathbf{G}^{\lessgtr}(t_1,t_2)\mathbf{h}(t_2)+\left[\mathbf{G}^{R}\cdot\mathbf{\Sigma}^{\lessgtr}+\mathbf{G}^{\lessgtr}\cdot\mathbf{\Sigma}^{A}+\mathbf{G}^{\rceil}\star\mathbf{\Sigma}^{\lceil}\right](t_1,t_2). \quad (3.47)\\ &= \mathbf{G}^{\lessgtr}(t_1,t_2)\mathbf{h}(t_2)+\mathbf{I}_2^{\lessgtr}(t_1,t_2),\end{aligned}$$

where $\mathbf{I}_{1,2}^{\lessgtr}$ are the $\lessgtr$-projections of the convolution integrals on the Keldysh contour. Similarly, one obtains for the mixed Green functions

$$\begin{aligned}i\partial_{t_1}\mathbf{G}^{\rceil}(t_1,\tau_2) &= \mathbf{h}(t_1)\mathbf{G}^{\rceil}(t_1,\tau_2)+\left[\mathbf{\Sigma}^{R}\cdot\mathbf{G}^{\rceil}+\mathbf{\Sigma}^{\rceil}\star\mathbf{G}^{M}\right](t_1,\tau_2), \quad (3.48)\\ &= \mathbf{h}(t_1)\mathbf{G}^{\rceil}(t_1,\tau_2)+\mathbf{I}^{\rceil}(t_1,\tau_2),\end{aligned}$$

$$\begin{aligned}-i\partial_{t_2}\mathbf{G}^{\lceil}(\tau_1,t_2) &= \mathbf{G}^{\lceil}(\tau_1,t_2)\mathbf{h}(t_2)+\left[\mathbf{G}^{\lceil}\cdot\mathbf{\Sigma}^{A}+\mathbf{G}^{M}\star\mathbf{\Sigma}^{\lceil}\right](\tau_1,t_2), \quad (3.49)\\ &= \mathbf{G}^{\lceil}(\tau_1,t_2)\mathbf{h}(t_2)+\mathbf{I}^{\lceil}(\tau_1,t_2),\end{aligned}$$

where $\mathbf{I}^{\rceil}(t_1,\tau_2)\equiv\mathbf{I}^{<}(t_1,t_0-i\tau_2)$ and $\mathbf{I}^{\lceil}(\tau_1,t_2)\equiv\mathbf{I}^{>}(t_0-i\tau_1,t_2)$ are the mixed time-variable projections of the convolution integrals[3]. Finally, one can also calculate the imaginary track projection of the EOM and one finds

$$\left(-\partial_\tau-\mathbf{h}_0\right)\mathbf{G}^{M}(\tau-\tau') = \mathbf{1}\delta(\tau-\tau')+i\left[\mathbf{\Sigma}^{M}\star\mathbf{G}^{M}\right](\tau-\tau'), \quad (3.50)$$

with $\mathbf{G}^{M}(\tau-\tau') = -i\mathbf{G}(-i\tau,-i\tau')$ and $\mathbf{\Sigma}^{M}(\tau-\tau') = -i\mathbf{\Sigma}(-i\tau,-i\tau')$ and where we have explicitly written the functions depending on the relative time. In the above equations, we have used a shorthand notations $\cdot$ and $\star$ for the real and imaginary time convolution integrals on the Keldysh contour

$$\begin{aligned}\left[\mathbf{a}\cdot\mathbf{b}\right](z_1,z_2) &= \int_{t_0}^{\infty}\mathbf{a}(z_1,t)\mathbf{b}(t,z_2)dt, \quad (3.51)\\ \left[\mathbf{a}\star\mathbf{b}\right](z_1,z_2) &= -i\int_{0}^{\beta}\mathbf{a}(z_1,\tau)\mathbf{b}(\tau,z_2)d\tau. \quad (3.52)\end{aligned}$$

[3]Similar notation applies to other mixed quantities also

Now, since the lesser and greater Green functions and the self-energies have the symmetry properties

$$\begin{aligned}\left[\mathbf{G}^{\lessgtr}(t_1,t_2)\right]^\dagger &= -\mathbf{G}^{\lessgtr}(t_2,t_1),\\ \left[\mathbf{\Sigma}^{\lessgtr}(t_1,t_2)\right]^\dagger &= -\mathbf{\Sigma}^{\lessgtr}(t_2,t_1),\\ \left[\mathbf{G}^{\lceil}(\tau,t)\right]^\dagger &= \mathbf{G}^{\rceil}(t,\beta-\tau),\\ \left[\mathbf{\Sigma}^{\lceil}(\tau,t)\right]^\dagger &= \mathbf{\Sigma}^{\rceil}(t,\beta-\tau),\end{aligned}$$

with $G^{>}_{mn}(t,t) = -i\delta_{mn} + G^{<}_{mn}(t,t)$, it is then necessary to only solve $\mathbf{G}^{<}(t_1,t_2)$ and $\mathbf{\Sigma}^{<}(t_1,t_2)$ for $t_1 \leq t_2$ and $\mathbf{G}^{>}(t_1,t_2)$ and $\mathbf{\Sigma}^{>}(t_1,t_2)$ for $t_1 > t_2$. One can also check that the convolution integrals obey the symmetry relations $[\mathbf{I}^{\lessgtr}_{1,2}(t,t')]^\dagger = -\mathbf{I}^{\lessgtr}_{2,1}(t',t)$ and $\mathbf{I}^{\lceil}(-i\tau,t) = [\mathbf{I}^{\rceil}(t,-i(\beta-\tau))]^\dagger$. The symmetry properties then imply that, in practice, we only need to solve the kinetic equations involving only $\mathbf{I}^{>}_1$,$\mathbf{I}^{<}_2$ and $\mathbf{I}^{\rceil}$ and the other components are determined through the above symmetry relations.

The last equation (3.50) is disconnected from the real-time and mixed-time equations and it describes the ground state solution for the one-particle Green function. The equations (3.46),(3.47),(3.48),(3.49) together with the ground-state solution (3.50) form the so called Kadanoff-Baym equations which can be solved numerically for different physical systems. The numerical implementation of the Kadanoff-Baym equations was done by N.E. Dahlen and was first applied to atoms and molecules in [71]. The numerical algorithm for solving the Dyson equation and performing the time-propagation is presented in detail in references [73] and [85].

3.6 Embedding self-energy and spectral broadening

In this work we consider the noninteracting parts of the electron reservoirs as two- or one-dimensional semi-infinite tight binding lattice structures. In the two-dimensional case, we assume that the leads have a finite width but infinite length. The general expression for the embedding self-energy is given by (we drop the CC indices from the $\mathbf{\Sigma}$)

$$\mathbf{\Sigma}_{\mathrm{em}}(z,z') = \sum_{\alpha=L,R} \mathbf{h}_{\mathrm{C}\alpha}\mathbf{g}_{\alpha\alpha}(z,z')\mathbf{h}_{\alpha\mathrm{C}} = \sum_{\alpha=L,R} \mathbf{\Sigma}_{\mathrm{em},\alpha}(z,z') \tag{3.53}$$

where the coupling Hamiltonians have the matrix elements

$$\begin{aligned}\left[\mathbf{h}_{\mathrm{C}\alpha}\right]_{ik} &= V_{i,k\alpha}\\ \left[\mathbf{h}_{\alpha\mathrm{C}}\right]_{ki} &= V_{k\alpha,i},\end{aligned} \tag{3.54}$$

with $i \in \mathrm{C}$ and $k \in \alpha$. Furthermore, the embedding self-energy has a similar structure as the Green function

$$\mathbf{\Sigma}_{\mathrm{em},\alpha}(z,z') = \theta(z,z')\mathbf{\Sigma}^{>}_{\mathrm{em},\alpha}(z,z') + \theta(z',z)\mathbf{\Sigma}^{<}_{\mathrm{em},\alpha}(z,z'), \tag{3.55}$$

where

$$\left[\mathbf{\Sigma}^{\gtrless}_{\mathrm{em},\alpha}\right]_{mn}(z,z') = \sum_{k,l\in\alpha} V_{m,k\alpha}\,\left[\mathbf{g}^{\gtrless}_{\alpha\alpha}\right]_{kl}(z,z')\,V_{l\alpha,n}, \tag{3.56}$$

and the lead Green functions $\mathbf{g}^{\gtrless}_{\alpha\alpha}(z,z')$ are expressed in the localized one-particle basis. For semi-infinite noninteracting leads the Green function $\mathbf{g}^{\gtrless}_{\alpha\alpha}(z,z')$ can be obtained from the Green functions in the delocalized orbital basis $\tilde{\mathbf{g}}^{\gtrless}_{\alpha\alpha}(z,z')$ which have the expressions

$$\left[\tilde{\mathbf{g}}^{>}_{\alpha\alpha}\right]_{kl}(z,z') = i\boldsymbol{\delta}_{kl}(f(\epsilon_{k\alpha})-1)e^{-i\int_{z'}^{z}(\epsilon_{k\alpha}-\mu+W^{\alpha}(\tilde{z}))d\tilde{z}}, \tag{3.57}$$

$$\left[\tilde{\mathbf{g}}^{<}_{\alpha\alpha}\right]_{kl}(z,z') = i\boldsymbol{\delta}_{kl}f(\epsilon_{k\alpha})e^{-i\int_{z'}^{z}(\epsilon_{k\alpha}-\mu+W^{\alpha}(\tilde{z}))d\tilde{z}}. \tag{3.58}$$

Here $\epsilon_{k\alpha}$ and $W^{\alpha}(t)$ are the energy of the k'th delocalized orbital and the time-dependent bias voltage of the lead α correspondingly and $\boldsymbol{\delta}$ is the unit matrix in the delocalized orbital basis of the lead. The basis transformation to the site basis can be obtained via the transformation matrix $\mathbf{D}$ which diagonalizes the Hamiltonian of the noninteracting lead α

$$\mathbf{D}\,\mathbf{h}_{\alpha\alpha}\,\mathbf{D}^{\dagger} = \mathrm{diag}(\epsilon_{k\alpha}), \tag{3.59}$$

and provides a mapping of the Fermion operators from the orbital basis $(\hat{a}_i, \hat{a}_i^{\dagger})$ to the localized site basis $(\hat{c}_i, \hat{c}_i^{\dagger})$. Consequently, the Green functions (3.57) and (3.58) transforms to the site basis as

$$\mathbf{g}^{\gtrless}_{\alpha\alpha}(z,z') = \mathbf{D}\,\tilde{\mathbf{g}}^{\gtrless}_{\alpha\alpha}(z,z')\,\mathbf{D}^{\dagger}, \tag{3.60}$$

so we have

$$\begin{aligned}\left[\mathbf{\Sigma}^{\lessgtr}_{\mathrm{em},\alpha}\right]_{mn}(z,z') &= \sum_{k,l\in\alpha} V_{m,k\alpha}\,\left[\mathbf{g}^{\lessgtr}_{\alpha\alpha}\right]_{kl}(z,z')\,V_{l\alpha,n} \\ &= \sum_{k,l,r,s\in\alpha} V_{m,k\alpha}\,[\mathbf{D}]_{kr}\,\left[\tilde{\mathbf{g}}^{\gtrless}_{\alpha\alpha}\right]_{rs}(z,z')\,\left[\mathbf{D}^{\dagger}\right]_{sl}V_{l\alpha,n}.\end{aligned} \tag{3.61}$$

We can furthermore define so called *linewidth function* $\mathbf{\Gamma}$ in the following way

$$[\mathbf{\Gamma}]_{mn,\alpha}(\epsilon) = 2\pi\sum_{k,r,s} V_{m,k\alpha}\,[\mathbf{D}]_{kr}\,\delta(\epsilon-\epsilon_{r\alpha})[\mathbf{D}^{\dagger}]_{rs}V_{s\alpha,n}, \tag{3.62}$$

and using this and the explicit expressions for the Green functions (3.57) and (3.58), the embedding self-energies then have the form

$$\mathbf{\Sigma}^{>}_{\mathrm{em},\alpha}(z,z') = ie^{-i\int_{z'}^{z}W^{\alpha}(\tilde{z})d\tilde{z}}\int\frac{d\epsilon}{2\pi}\left[f(\epsilon)-1\right]\mathbf{\Gamma}_{\alpha}(\epsilon)\,e^{-i(\epsilon-\mu)(z-z')}, \tag{3.63}$$

$$\mathbf{\Sigma}^{<}_{\mathrm{em},\alpha}(z,z') = ie^{-i\int_{z'}^{z}W^{\alpha}(\tilde{z})d\tilde{z}}\int\frac{d\epsilon}{2\pi}f(\epsilon)\mathbf{\Gamma}_{\alpha}(\epsilon)\,e^{-i(\epsilon-\mu)(z-z')}, \tag{3.64}$$

which can be easily evaluated numerically. It is then clear, that the form of the embedding self-energy depends on the structure of the lead, *i.e.* the energy spectrum and eigenfunctions which construct the linewidth function $\mathbf{\Gamma}$. In the appendix (A.0.1) it is shown that for two-dimensional semi-infinite lead α with R_α rows, longitudinal (λ) nearest neighbor hopping b_α^λ, transverse (τ) nearest neighbor hopping b_α^τ and on-site energy a_α this function is given by

$$\mathbf{\Gamma}_{mn,\alpha}(\epsilon) = \sum_{I,J,A}^{R_\alpha} \left[\mathbf{D}_\alpha^\tau\right]_{IA} \Gamma_{mn,\alpha}^{IJA}(\epsilon) \left[\mathbf{D}_\alpha^{\tau,\dagger}\right]_{AJ} \tag{3.65}$$

where

$$\Gamma_{mn,\alpha}^{IJA}(\epsilon) = \frac{2V_{i,I1\alpha}V_{J1\alpha,j}}{|b_\alpha^\lambda|}\sqrt{1-\frac{\hat{E}^2}{4|b_\alpha^\lambda|^2}}\;\Theta(2|b_\alpha^\lambda|-|\hat{E}|), \tag{3.66}$$

and $\hat{E} = \epsilon - a_\alpha - \epsilon_{A\alpha}$, with $\epsilon_{A\alpha} = -2|b_\alpha^\tau|\cos\left(\frac{A\pi}{R_\alpha+1}\right)$. Here the matrix elements $\mathbf{U}$ are given by the eigenfunctions of the transverse TB chain, $[\mathbf{D}_\alpha^\tau]_{IA} = \sqrt{\frac{2}{R_\alpha+1}}\sin\left(\frac{IA\pi}{R_\alpha+1}\right)$. Moreover, the coupling matrix elements $V_{m,I1\alpha}$ describe the physical connections between the sites m of the central region and the sites I of the first layer in lead α and vice versa.

In Fig. (3.2) we show an example of the real-time embedding self-energies (3.63) and (3.64) in double-time plane for two-dimensional semi-infinite lead with nine rows and with lead hopping parameters $b^\lambda = b^\tau = -2.5$. For this plots, the coupling matrix is now assumed to have connections only to the terminal site of the central row (in this case 5th row) of atoms of the two-dimensional lead and we set the coupling strength to be $V = -1.0$ so the embedding self-energies then equal the lattice Green function at that particular lattice position. We also consider the system at zero temperature ($\beta = 120$) with $\mu = 0$ and unperturbed ($W^\alpha(t) = 0$). As can be seen, both the real and imaginary parts oscillate in relative time with the frequencies equal to addition/removal energies and the oscillation is strongly damped due to the dissipative environment (energy continuum). Furthermore, the time-diagonal of $\mathrm{Im}\Sigma_{\mathrm{em}}^<(t,t^+) = V^2\mathrm{Im}\,g^<(t,t^+)$ gives the time-dependent spin-orbital occupation of the terminal site, $n^0(t) = 0.5$ since the coupling elements are set to $V = -1.0$. The lower panels shows the behavior of the mixed self-energy component (Green function) $\Sigma^\rceil(t,\tau)$. For $t = 0$ these functions equal the Matsubara Green function $g^M(\tau)$ which is a real function and is peaked around the edges of the imaginary time-interval $\tau \in [0,\beta]$. The Matsubara Green function obeys the anti-periodicity property, $g^M(\tau+\beta) = -g^M(\tau)$, even it cannot be seen from this plot due to the restricted time-interval. The mixed Green functions also damp as the difference between the time-arguments increases. The greater ($>$) quantities $\mathrm{Re}\,\Sigma_{\mathrm{em}}^\lceil(\tau,t)$, $\mathrm{Im}\,\Sigma_{\mathrm{em}}^\lceil(\tau,t)$ and $\mathrm{Im}\,\Sigma_{\mathrm{em}}^>(t,t')$ can be obtained by simply multiplying the corresponding lesser ($<$) quantities with -1.

For the time-translational invariant case, *i.e.*, when the bias voltage is time independent

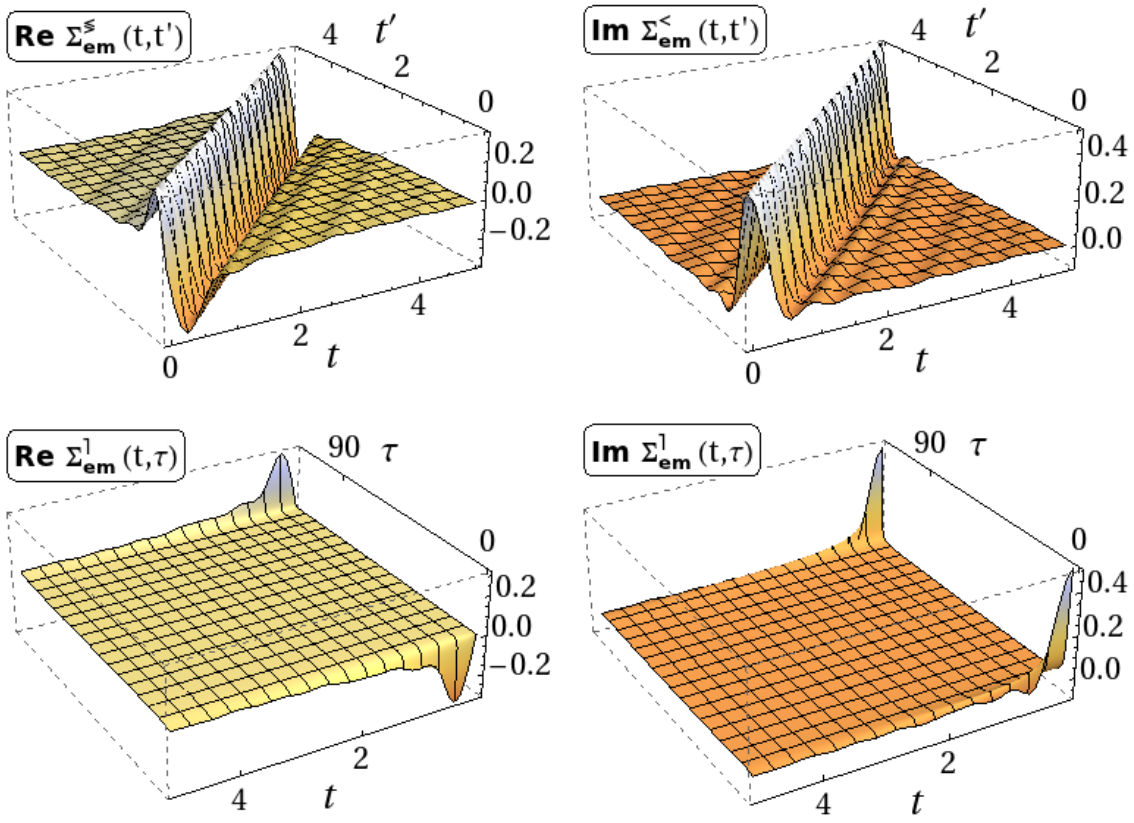

Figure 3.2: Embedding self-energies for a single site coupled to the terminal site of 5th row of the two-dimensional semi-infinite tight binding lattice. The parameters are chosen as follows: $b^{\lambda} = b^{\tau} = -2.5, a = \mu = 0, \beta = 120, W^{\alpha} = 0, R_{\alpha} = 9$ and $V = -1.0$.

or the system has reached a steady-state, the embedding self-energies can be expressed in ω -space

$$\mathbf{\Sigma}^{\lessgtr}_{\mathrm{em},\alpha}(z-z') = \int \frac{d\epsilon}{2\pi} e^{-i\epsilon(z-z')}\, \mathbf{\Sigma}^{\lessgtr}_{\mathrm{em},\alpha}(\epsilon), \tag{3.67}$$

where

$$\mathbf{\Sigma}^{>}_{\mathrm{em},\alpha}(\omega) = i[f_{\alpha}(\omega)-1]\tilde{\mathbf{\Gamma}}_{\alpha}(\omega), \tag{3.68}$$

$$\mathbf{\Sigma}^{<}_{\mathrm{em},\alpha}(\omega) = i f_{\alpha}(\omega)\tilde{\mathbf{\Gamma}}_{\alpha}(\omega), \tag{3.69}$$

with $f_{\alpha}(\omega) = f(\omega - W^{\alpha})$ and $\tilde{\mathbf{\Gamma}}_{\alpha}(\omega) = \mathbf{\Gamma}_{\alpha}(\omega - W^{\alpha})$. Furthermore, we can also calculate the retarded and advanced self-energies by Fourier transforming the real-time functions

$\mathbf{\Sigma}^{R/A}_{\mathrm{em},\alpha}(t,t') = \pm\theta(\pm t \mp t')[\mathbf{\Sigma}^{>}_{\mathrm{em},\alpha}(t-t') - \mathbf{\Sigma}^{<}_{\mathrm{em},\alpha}(t-t')]$ which gives

$$\mathbf{\Sigma}^{R/A}_{\mathrm{em},\alpha}(\omega) = \mathbf{\Lambda}_\alpha(\omega) \mp \frac{i}{2}\mathbf{\Gamma}_\alpha(\omega), \tag{3.70}$$

where

$$\mathbf{\Lambda}_\alpha(\omega) = \mathscr{P}\int \frac{d\omega'}{2\pi}\frac{\mathbf{\Gamma}_\alpha(\omega')}{\omega-\omega'}, \tag{3.71}$$

is the Hilbert transform of the linewidth function and $\mathbf{\Gamma}_\alpha(\omega) = -2\,\mathbf{h}_{C\alpha}\mathrm{Im}\left\{\mathbf{g}^R_{\alpha\alpha}(\omega)\right\}\mathbf{h}_{\alpha C}$ is essentially the imaginary part of the retarded Green function of the lead α weighted with the coupling matrices. The coupling of the correlated central region to the energy continua of the leads introduces a finite broadening to the many-body states of the central region. To see this more clearly, let us take the retarded Green function of the correlated central region by extracting the retarded component from (3.40) and assume that the system is in the steady-state when all the quantities depend on the time difference. We can then obtain the spectral function $\mathbf{A}_{CC}(\omega)$ of the central region as

$$\begin{aligned}
\mathbf{A}_{CC}(\omega) &= -\frac{1}{\pi}\mathrm{Im}\left\{\mathbf{G}^R_{CC}(\omega)\right\}, \\
&= -\frac{1}{\pi}\mathrm{Im}\left\{\frac{1}{\mathbf{1}(\omega+i\eta) - \mathbf{h}_{CC} - \mathbf{\Sigma}^{\mathrm{MB},R}_{CC}(\omega) - \mathbf{\Sigma}^R_{\mathrm{em},CC}(\omega)}\right\}, \\
&= -\frac{1}{\pi}\frac{\gamma(\omega)}{\left[\mathbf{1}\omega - \mathbf{h}_{CC} - \mathbf{\Delta}(\omega)\right]^2 + \boldsymbol{\gamma}(\omega)^2},
\end{aligned} \tag{3.72}$$

where $\mathbf{\Delta}(\omega) = \mathrm{Re}\left(\mathbf{\Sigma}^{\mathrm{MB},R}_{CC}(\omega)\right) + \mathbf{\Lambda}_\alpha(\omega)$ and $\boldsymbol{\gamma}(\omega) = \mathrm{Im}\left(\mathbf{\Sigma}^{\mathrm{MB},R}_{CC}(\omega)\right) - \mathbf{\Gamma}(\omega)/2$ are the real and imaginary parts of the self-energies. Equation (3.72) gives the local density of states (LDOS) matrix for the correlated domain C in the presence of the electron reservoirs. We see that the delta peaks positioned at the energies of the many-body levels of the isolated central region broaden to Lorentzian-shaped resonances due to the finite imaginary part in $\boldsymbol{\gamma}(\omega)$ due to the embedding self-energy. Moreover, the real part of the embedding self-energy shifts the positions of the peaks to higher or lower energies depending on the sign of $\Lambda(\omega)$ at the given energy of particular energy level.

In Fig. 3.3 we demonstrate the impact of the embedding self-energy on the energy levels which are physically coupled (finite coupling matrix elements $\mathbf{h}_{C\alpha/\alpha C} = -1.0$) to the semi-infinite one-dimensional tight binding lead with the lead TB parameters $a = \mu = 0, b^\lambda = -2.5$ and zero temperature. In the left panel we plot the real ($\Lambda(\omega)$) and imaginary ($\Gamma(\omega)/2$) parts of the retarded embedding self-energy (=Green function at the terminal site of the lead) in frequency space, see Eq. (3.70). As can be clearly seen from the equation of $\Gamma(\omega)$ (3.66) and from the left panel of Fig. (3.3) the imaginary part (for 1D system) is nonzero only within the frequency regime $[-2|b^\lambda|, 2|b^\lambda|]$ and has a maximum at $\omega = 0$ with $-\mathrm{Im}\Sigma^R_{\mathrm{em}}(\omega=0) = V^2/|b^\lambda|$. In the right panel we then

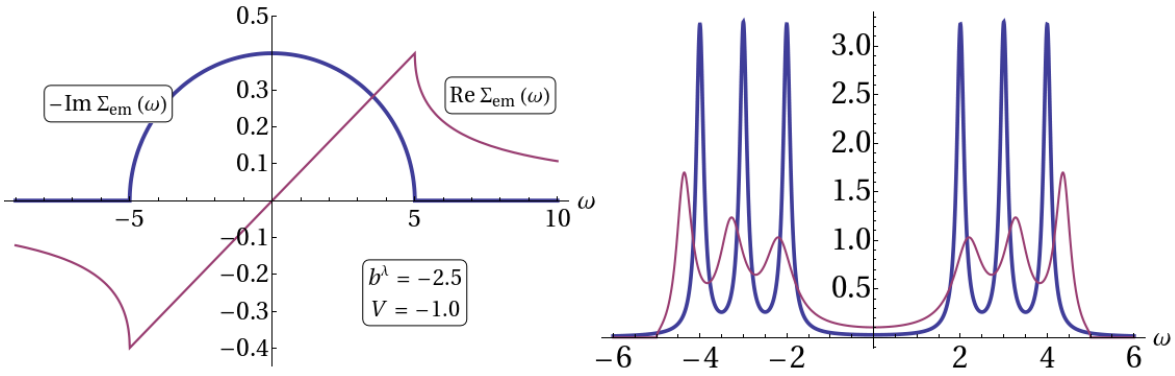

Figure 3.3: Left panel: Retarded embedding self-energy (the Green function at the terminal site of the lead) in frequency space for one-dimensional semi-infinite lead with $V = -1.0$ and $b^{\lambda} = -2.5$. Right panel: Spectral function of a six-level system coupled to continuum described by the embedding of left panel (thin curve) and a constant complex number $\Gamma = 0.1$ (sharp peaks).

show the corresponding spectral function of a six-level system (energy levels positioned at $\epsilon_i = -4,-3,-2,2,3,4$) where each of the levels is coupled to semi-infinite tight binding lead described by the embedding in the left panel (broad peaks, violet color). In addition, we also show the spectral function which is coupled to so called *wide-band lead* where the retarded embedding self-energy is approximated by a structureless imaginary constant $\Sigma^R_{\text{em}}(\omega) \approx i\Gamma$, $\Gamma = 0.1$ (blue,sharp peaks). We see that the levels coupled to the TB lead shift due to the finite real part of $\Sigma^R_{\text{em}}(\omega)$ whereas the wide-band approximation keeps the level positions static. Furthermore, it can be seen that the broadening of the spectral peaks depend on the energy domain since in the TB approximation the $\Gamma(\omega)$ has frequency dependency: The closer the edge the level is positioned, the smaller $\Gamma(\omega)$ will be and the less it broadens the spectral peak. If the level falls outside the lead continuum, it does not get broadened. In contrast to the frequency-dependent $\Gamma(\omega)$, in the wide-band approximation the levels are broaden equal amount.

It is also interesting to see how the physical parameters of the lead changes the form of the embedding self-energy in the two-dimensional case. In Fig. (3.4) we show the real and imaginary parts of $\Sigma^R_{\text{em}}(\omega)$ for different lead TB parameters for 2D lead with 9 rows with a simple terminal site coupling between the hybridized quantum system C and terminal site of 5th row. In the top left and bottom right panels the embedding self-energy is plotted with the equal longitudinal and transverse hoppings $b^{\lambda} = b^{\tau} = -1.0$ (top left) and $b^{\lambda} = b^{\tau} = -2.5$ (bottom right) whereas for the top right and bottom left panels the hoppings are not equal anymore. As can be seen from equation (3.65) the embedding self-energy is a sum of individual 1D self-energies (see Fig (3.3)) which are shifted and separated from each other on the ω axis with the transverse channel eigenvalue $-2|b^{\tau}|\cos(A\pi/(R+1))$ ($A = 1,...,R$ and $R = 9$). Furthermore, since the coupling matrix element is chosen to be nonzero only to the terminal site of 5th

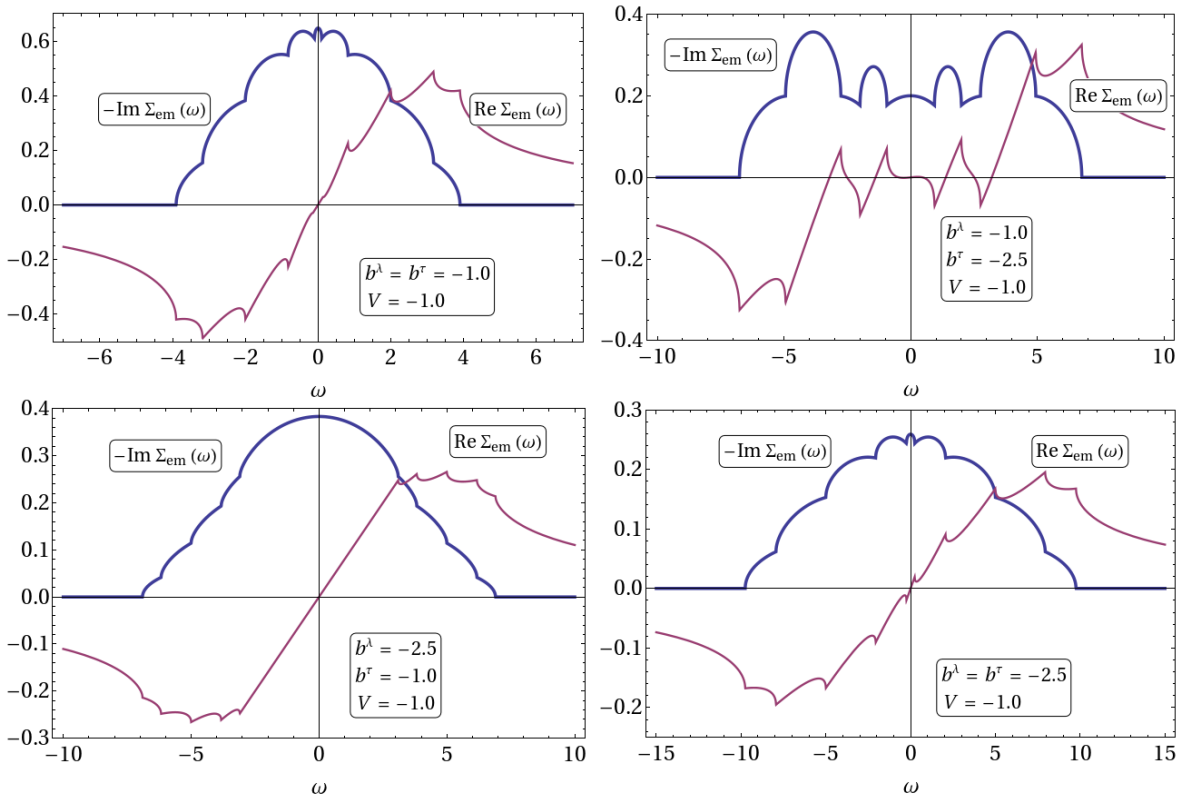

Figure 3.4: 2D retarded embedding self-energies for different lead parameters. A lead with 9 rows is considered here.

row, the prefactors $\frac{2}{R+1}\sin^2\left(\frac{5A\pi}{R+1}\right)$ arising from the eigenfunctions of the transverse channel give nonzero contributions only from every second site index A, *i.e.* for $A = 1, 3, 5, 7$ and $A = 9$. In general, however, the hybridization/coupling matrix can have multiple links between the hybridized nanostructure and the particle reservoir. Now, depending on the strength of the hopping parameters, the width of the imaginary part changes. For purely semi-infinite two-dimensional lattice, this width would be given by $[-2|b^\lambda| - 2|b^\tau|, 2|b^\lambda| + 2|b^\tau|]$ but already a finite lattice in transverse direction approaches this limit. The structure of the embedding SE is then simply determined the relative separation of the individual channel contributions, *i.e.* the parameters b^τ and b^λ and, as shown in the off-diagonal panels of Fig. (3.4), it can have a dramatic impact on the shape of $\Sigma^R_{\text{em}}(\omega)$ and furthermore to the non-equilibrium dynamics in transport systems through the spectral broadening and level shifting.

As a final check before continuing with the transport theory, let us see how the embedding self-energy behaves as a function of the number of rows in the transverse direction. For this purpose, we plot in Fig. (3.5) the $\Sigma^R_{\text{em}}(\omega)$ for $R_\alpha = 3$ (top left), $R_\alpha = 5$ (top right), $R_\alpha = 7$ (bottom left) and for $R_\alpha = 9$ (bottom right) rows. It can be clearly seen that the "resolution" of the embedding improves as the number of rows

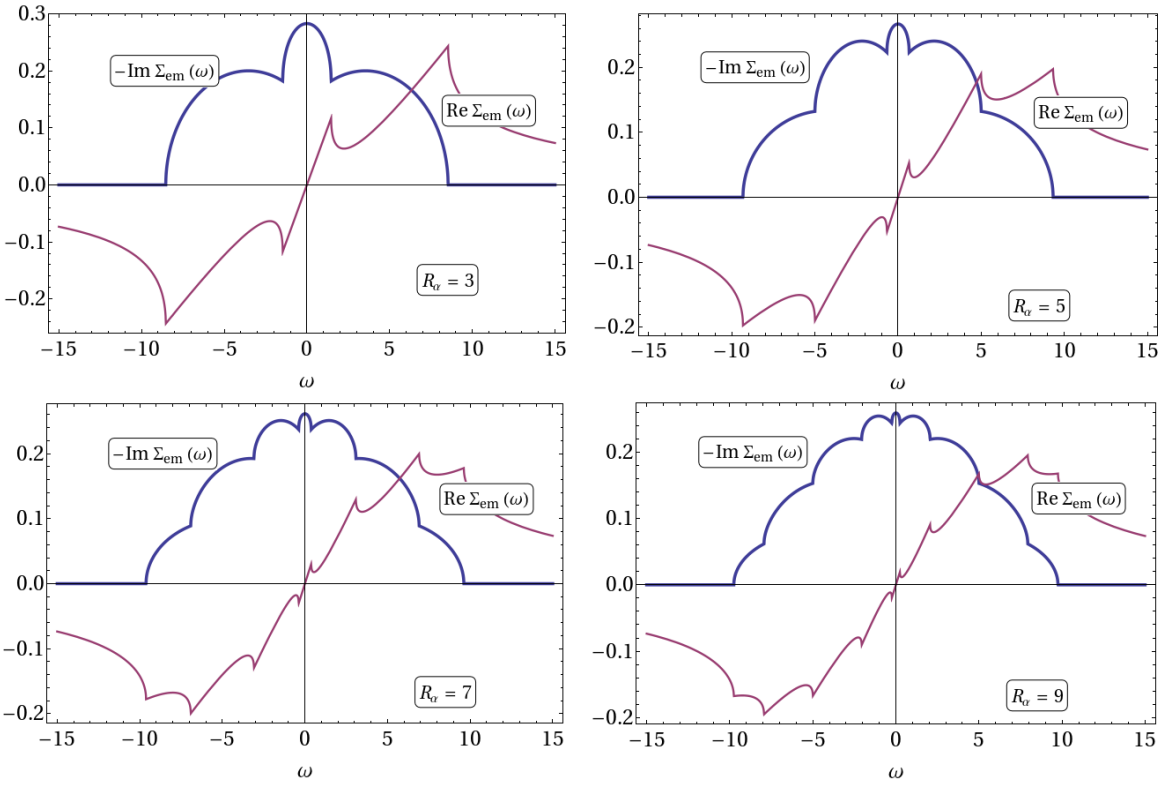

Figure 3.5: 2D retarded embedding self-energies for different lead widths $R_\alpha = 3, 5, 7$ and $R_\alpha = 9$ with the coupling only to the terminal site of 5th row. The parameters used for this plot are: $b^\lambda = b^\tau = -2.5, \mu = a = 0.0$ and $V_{\alpha 5,i} = V_{i,\alpha 5} = 1.0$.

is increased: The real and imaginary parts start to form a smoother function with less dramatic discontinuities and in the limit of $R_\alpha \to \infty$ (not shown here) the embedding self-energy becomes completely smooth function. It it, however, our interest also to investigate the transient dynamics in the lead regions as well which motivates us to keep the particle reservoirs a finite width. Let us next turn our attention to how to extract the time-dependent dynamics of the particle reservoirs from the embedded Kadanoff-Baym equations.

3.7 Lead density dynamics and Inbedding self-energy

The solution, $\mathbf{G}_{\mathrm{CC}}$ of the compact form of the embedded Kadanoff-Baym equations (3.40) allows not only the access to the time-dependent properties of the central region, but also to the dynamics of the lead regions. To see this, we first project the equation of motion (3.38) to $\alpha\alpha$-subspace

$$\left\{i\partial_z - \mathbf{h}_{\alpha\alpha}(z)\right\}\mathbf{G}_{\alpha\alpha}(z,z') = \mathbf{1}\delta(z,z') + \mathbf{h}_{\alpha\mathrm{C}}\mathbf{G}_{\mathrm{C}\alpha}(z,z'), \tag{3.73}$$

and use the $C\alpha$-projection of the equation (3.37)

$$\mathbf{G}_{C\alpha}(z,z') = \int d\bar{z}\, \mathbf{G}_{CC}(z,\bar{z})\, \mathbf{h}_{C\alpha}\, \mathbf{g}_{\alpha\alpha}(\bar{z},z'). \tag{3.74}$$

We then obtain the equation for the full lead Green function $\mathbf{G}_{\alpha\alpha}$

$$\Big\{ i\partial_z - \mathbf{h}_{\alpha\alpha}(z) \Big\} \mathbf{G}_{\alpha\alpha}(z,z') = \mathbf{1}\delta(z,z') + \int d\bar{z}\, \mathbf{\Sigma}_{\text{in},\alpha\alpha}(z,\bar{z})\, \mathbf{g}_{\alpha\alpha}(\bar{z},z'), \tag{3.75}$$

where we denoted the *inbedding self-energy* as

$$\mathbf{\Sigma}_{\text{in},\alpha\alpha}(z,z') = \mathbf{h}_{\alpha C} \mathbf{G}_{CC}(z,z') \mathbf{h}_{C\alpha}. \tag{3.76}$$

The equation (3.75) can now be solved for $\mathbf{G}_{\alpha\alpha}(z,z')$ with help of $\alpha\alpha$-projection of Eq. (3.35) and the result becomes

$$\mathbf{G}_{\alpha\alpha}(z,z') = \mathbf{g}_{\alpha\alpha}(z,z') + \int\int d\bar{z} d\bar{\bar{z}}\, \mathbf{g}_{\alpha\alpha}(z,\bar{z}) \mathbf{\Sigma}_{\text{in},\alpha\alpha}(\bar{z},\bar{\bar{z}}) \mathbf{g}_{\alpha\alpha}(\bar{\bar{z}},z'). \tag{3.77}$$

We can now from this equation obtain the time-dependent density in the lead α by simply extracting the lesser-component ($\mathbf{G}^<$) and taking the equal-time limit $z = t, z' = t^+$ in the Green function. The density in the localized spin-orbital k of the lead α is then given by

$$\begin{aligned}
n_{\alpha,k}(t) &= -iG^<_{kk}(t,t^+) \\
&= n^0_{\alpha,k}(t) - i \left\{ \int\int d\bar{z} d\bar{\bar{z}}\, \mathbf{g}_{\alpha\alpha}(t,\bar{z}) \mathbf{\Sigma}_{\text{in},\alpha\alpha}(\bar{z},\bar{\bar{z}})\, \mathbf{g}_{\alpha\alpha}(\bar{\bar{z}},t^+) \right\}^<_{kk} \\
&= n^0_{\alpha,k}(t) - i \Big\{ \mathbf{g}^< \cdot \mathbf{\Sigma}^A_{\text{in}} \cdot \mathbf{g}^A + \mathbf{g}^R \cdot \mathbf{\Sigma}^<_{\text{in}} \cdot \mathbf{g}^A + \mathbf{g}^\rceil \cdot \mathbf{\Sigma}^\lceil_{\text{in}} \cdot \mathbf{g}^A \\
&\qquad + \mathbf{g}^R \cdot \mathbf{\Sigma}^R_{\text{in}} \cdot \mathbf{g}^< + \mathbf{g}^R \cdot \mathbf{\Sigma}^\rceil_{\text{in}} \star \mathbf{g}^\lceil + \mathbf{g}^\rceil \star \mathbf{\Sigma}^M_{\text{in}} \star \mathbf{g}^\lceil \Big\}_{\alpha\alpha,kk} (t,t^+)
\end{aligned} \tag{3.78}$$

where we denoted $n^0_{\alpha,k}(t) = -ig^<_{\alpha\alpha,kk}(t,t^+)$ and in the last step the lesser component was written explicitly using the Langreth rules on the Keldysh contour. As can be seen, the time-dependent density is given by the density of the uncontacted lead $n^0_{\alpha,k}(t)$ plus an additional "perturbation" (the second term) induced by the presence of the interacting scattering region C.

3.8 Time-dependent current

As one of the main observables, we are interested in the time-dependent current flowing through the interacting-noninteracting interface between the central region and the

leads. We refer these as the left and right currents, $I_L(t)$ and $I_R(t)$ correspondingly and the sum of these currents as the total current $I_T(t)$. The current flowing through the interface α ($\alpha = L,R$) is given by

$$\begin{aligned} I_\alpha(t) &= \frac{d\langle \hat{N}_\alpha(t)\rangle}{dt} \\ &= -\mathrm{Tr}_\alpha\Big\{ i\partial_t \mathbf{G}^<_{\alpha\alpha}(t,t') + i\partial_{t'}\mathbf{G}^<_{\alpha\alpha}(t,t')\Big\}_{t'=t} \end{aligned} \tag{3.79}$$

where we have defined the current with respect to the change in the total particle number in the lead α, *i.e.*, we say that we have a positive current/particle flow to the lead α if the number of particles is increasing in α -domain. One can also define the current flow with an extra minus sign to refer to the real current which is opposite to the direction of the electron flow, but it is only a matter of convention and will not change the formalism in any way. The time-derivatives are now obtained from (3.31) and (3.32)

$$i\partial_t \mathbf{G}^<_{\alpha\alpha}(t,t') = \mathbf{1}\delta(t,t') + \mathbf{h}_{\alpha\alpha}(t)\mathbf{G}^<_{\alpha\alpha}(t,t') + \mathbf{h}_{\alpha\mathrm{C}}\mathbf{G}^<_{\mathrm{C}\alpha}(t,t') \tag{3.80}$$

$$-i\partial_{t'} \mathbf{G}^<_{\alpha\alpha}(t,t') = \mathbf{1}\delta(t,t') + \mathbf{G}^<_{\alpha\alpha}(t,t')\mathbf{h}_{\alpha\alpha}(t') + \mathbf{G}^<_{\alpha\mathrm{C}}(t,t')\mathbf{h}_{\mathrm{C}\alpha} \tag{3.81}$$

Subtracting (3.81) from (3.80), tracing over $\alpha\alpha$, setting $t' = t^+$ we obtain

$$I_\alpha(t) = -\mathrm{Tr}_\alpha\Big\{ \mathbf{h}_{\alpha\mathrm{C}}\mathbf{G}^<_{\mathrm{C}\alpha}(t,t') + \mathbf{G}^<_{\alpha\mathrm{C}}(t,t')\mathbf{h}_{\mathrm{C}\alpha}\Big\}_{t'=t^+}. \tag{3.82}$$

Now, by using the symmetry of the second piece

$$\Big\{ \mathbf{G}^<_{\alpha\mathrm{C}}(t,t')\mathbf{h}_{\mathrm{C}\alpha}\Big\}_{t'=t^+} = -\Big\{ \mathbf{h}_{\alpha\mathrm{C}}\mathbf{G}^<_{\mathrm{C}\alpha}(t,t^+)\Big\}^\dagger,$$

we obtain

$$\begin{aligned} I_\alpha(t) &= -2\mathrm{Re}\,\mathrm{Tr}_\alpha\Big\{ \mathbf{h}_{\alpha\mathrm{C}}\mathbf{G}^<_{\mathrm{C}\alpha}(t,t^+)\Big\}, \\ &= -2\mathrm{Re}\,\mathrm{Tr}_\mathrm{C}\Big\{ \mathbf{G}^<_{\mathrm{C}\alpha}(t,t^+)\mathbf{h}_{\alpha\mathrm{C}}\Big\}. \end{aligned} \tag{3.83}$$

Finally inserting the $C\alpha$-projection of the equation (3.37) we get the formula for the time-dependent current through the interface α:

$$\begin{aligned} I_\alpha(t) &= -2\mathrm{Re}\,\mathrm{Tr}_\mathrm{C}\Big\{ \int d\bar{z}\, \mathbf{G}_{\mathrm{CC}}(t,\bar{z})\mathbf{\Sigma}_{\mathrm{em},\alpha,\mathrm{CC}}(\bar{z},t^+)\Big\}^< \\ &= -2\mathrm{Re}\,\mathrm{Tr}_\mathrm{C}\Big\{ \int_0^\infty d\bar{t}\, \Big[\mathbf{G}^<_{\mathrm{CC}}(t,\bar{t})\mathbf{\Sigma}^A_{\mathrm{em},\alpha,\mathrm{CC}}(\bar{t},t^+) + \mathbf{G}^R_{\mathrm{CC}}(t,\bar{t})\mathbf{\Sigma}^<_{\mathrm{em},\alpha,\mathrm{CC}}(\bar{t},t^+)\Big]\Big\} \\ &\qquad -i\int_0^\beta d\bar{\tau}\, \mathbf{G}^\rceil_{\mathrm{CC}}(t,\bar{\tau})\mathbf{\Sigma}^\lceil_{\mathrm{em},\alpha,\mathrm{CC}}(\bar{\tau},t^+)\Big\}, \end{aligned} \tag{3.84}$$

where $\mathbf{\Sigma}_{\mathrm{em},\alpha,\mathrm{CC}}$ is again the embedding self-energy of lead α in CC indices. The first two terms describe the real-time contributions to the time-dependent current. Since the Green function, many-body self-energy and the embedding self-energy are in general time-nonlocal quantities, the real time-integrals will be performed over the history of the Green function and embedding self-energy. The nonlocal terms induce memory to the system and the first two terms integrate it into the time-dependent current. The last term, however, allows for the initial correlation and embedding effects to contribute to the real-time current, since the mixed-time variable quantities $(\rceil, \lceil)$ holds the memory of the initial state corresponding to the imaginary track of the Keldysh contour.

If we assume that in the long-time limit, when $t \to \infty$, the last term due to the memory of the initial state becomes zero, the current formula reduces (see appendix A.0.2) to the well-known Meir-Wingreen formula for the steady-state current [40]

$$I_\alpha^S = -i\,\mathrm{Tr}_\mathrm{C}\left\{\int_{-\infty}^{\infty}\frac{d\omega}{2\pi}\,\mathbf{\Gamma}_{\mathrm{CC},\alpha}(\omega)\Big\{\mathbf{G}^<_{\mathrm{CC}}(\omega) - 2\pi i f_\alpha(\omega)\mathbf{A}_{\mathrm{CC}}(\omega)\Big\}\right\}. \tag{3.85}$$

where

$$\begin{aligned}\mathbf{A}_{CC}(\omega) &= -\frac{1}{2\pi i}\Big\{\mathbf{G}^R_{\mathrm{CC}}(\omega) - \mathbf{G}^A_{\mathrm{CC}}(\omega)\Big\}, &(3.86)\\ &= -\frac{1}{\pi}\mathrm{Im}\Big\{\mathbf{G}^R_{\mathrm{CC}}(\omega)\Big\}, &(3.87)\end{aligned}$$

is the spectral function of the interacting central region with

$$\mathbf{G}^{R/A}_{\mathrm{CC}}(\omega) = \frac{1}{\mathbf{1}(\omega \pm i\eta) - \mathbf{h}_{\mathrm{CC}} - \mathbf{\Sigma}^{R/A}_{\mathrm{CC}}(\omega)}, \tag{3.88}$$

and

$$\mathbf{\Gamma}_{\mathrm{CC},\alpha}(\omega) = -2\,\mathrm{Im}\Big\{\mathbf{\Sigma}^R_{\mathrm{em},\alpha}(\omega)\Big\}, \tag{3.89}$$

is the imaginary part of the retarded embedding self-energy. Moreover, $f_\alpha(\omega) = f(\omega + W^\alpha)$ is the Fermi function of the W^α-biased lead α. Equation (3.84) is then a generalization of the Meir-Wingreen formula and the time-dependent current formula of Wingreen *et al.* [61, 50] to the transient time-domain and it correctly takes into account the corrections to the transient current due to the initial thermalization via the last integral term.

4 Numerical simulations

In the previous chapter we introduced the many-particle formalism to treat open and correlated quantum systems in nonequilibrium situations. This chapter is dedicated to applications of this formalism to two-terminal quantum transport. Instead of giving just an overall view of the research articles published for this thesis, I will demonstrate the main topics of the research articles with examples and focus also on topics which were not discussed in the published work. In this sense, this chapter extends the research articles and forms an entity that supports the already published work.

In the first section we look at the general transport properties of correlated quantum dot/two level systems coupled to semi-infinite noninteracting leads. We shall first investigate the basic time-dependent features which are present in the charge transport processes from the point of view of electron-electron interactions and correlation effects but also from the point of view of the electron reservoirs. The second section is then dedicated to an overview of the initial correlation effects and their implications on the transport features. These first two sections then contain most of the essential scientific content that was reported in the research articles [1] and [2]. In the third section the traditional transport setup is then elaborated to include the Coulomb interactions between the central scattering region and the electron reservoirs. An overview on how the lead interaction effects change the transient and steady-state transport features is given and it encapsulates the work reported in the research article [3]. The last section then summarizes the work published in journal article [4] concerning time-dependent alternating fields.

4.1 General transport properties of embedded quantum systems

Quantum wires are propably the most simplest systems to simulate the time-dependent transport phenomenon in the context of molecular electronics. A quantum wires are wire-like systems where the electrons are confined to move effectively in one dimension and the properties are determined by the quantum mechanics. In our model description, a quantum wire can be realized by simply placing atomic sites with nearest neighbor hopping next to each other into wire-like formation. This wire can then be attached to electron reservoirs and we then have a very simple model for transport sim-

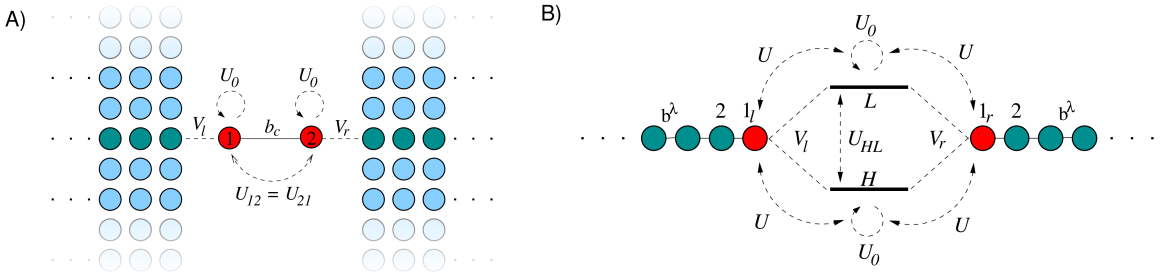

Figure 4.1: Transport setups for correlated two-site system coupled to two-dimensional noninteracting electrodes (A) and for two-level system coupled to one-dimensional electrodes with lead-molecule interaction (B)

ulations which can be modeled with the PPP/TB Hamiltonian given by Eq. (3.26). In the research articles [1] and [2] we investigated the transport properties of this kind of quantum wires attached to semi-infinite one -and two-dimensional leads.

We can, alternatively, work in the eigenbasis of the wire Hamiltonian and express the central wire as delocalized orbitals coupled to the terminal sites of the left and right leads. The mapping between these different pictures is provided by the unitary transformation matrix containing the eigenvectors of the wire Hamiltonian and, in this sense, they contain exactly the same physics with the only difference that all the matrix elements of one and two-body Hamiltonian and the coupling Hamiltonian are in the delocalized basis. In some cases, such as in the research article [3] the orbital-based approach provides much easier way to analyze the physics of the electron transport and the implications of the long-range Coulomb interaction on the properties of the system and we shall now employ both approaches to demonstrate some of the general transport properties of simple quantum systems.

4.1.1 Model transport setups

Let us consider two quantum transport setups depicted in Fig. (4.1). In the panel (A) we have a interacting two-site system connected to two-dimensional semi-infinite leads (l=left lead, r=right lead) with finite width. We shall use the following parameters for this setup: hopping $b_c = -0.75$ between sites 1 and 2, terminal site couplings $V_l = V_r = -0.35$ between the leads and central wire, longitudinal and transverse lead hopping $b^\lambda = b^\tau$ and the Coulomb interaction $w_{11} = w_{22} = U_0 = 1.0$ and $w_{12} = w_{21} = 0.5$ for the sites in the central region. The disconnected two-site system then has the Hartree-Fock energy levels at $\epsilon_1^{HF} = -0.5$ and $\epsilon_2^{HF} = 1.5$ with the HF gap $\Delta = 2.0$.

In the panel (B) we then have a simple two-level system (orbital representation of wire-like system) with the levels denoted by H (HOMO, highest occupied molecular orbital) and L (LUMO, lowest unoccupied molecular orbital) with the corresponding

single-particle energies $h_{ii} = \epsilon_i$, $i = H, L$. The two-level system is also coupled to left and right one-dimensional noninteracting electrodes ($b^\lambda = -1.0$) via weak tunneling Hamiltonians $V_{H/L,l} = V_{H/L,r} = -0.2$ and we denote the local Coulomb interaction matrix elements as $w_{ii} = U_0 = 1.0$ for the electrons occupying the same single particle level $i = H, L$ and the off-diagonal interaction matrix elements between the levels as $w_{HL} = U_{HL} = U_{LH} = w_{LH} = 1.0$. In this model we also consider the long-range Coulomb interaction between the molecular levels and the terminal sites of the leads. This is interaction strength is denoted with U. Furthermore, we choose the single particle levels $\epsilon_1 = -2.0$ and $\epsilon_2 = -1.0$ which then, together with the interaction matrix elements, yield the HF levels at $\epsilon_1^{HF} = -1.0$ and $\epsilon_2^{HF} = 1.0$ with the gap $\Delta = 2.0$.

For the sake of simplicity, in both transport setups we choose zero-temperature limit, half-filling for the leads and set the chemical potential between the Hartree-Fock energy levels of the isolated central region. The case of finite temperatures is left outside of this thesis and will be a subject of later investigations.

4.1.2 Transient and steady-state properties – mean-field study

We first demonstrate the transient and steady-state properties of the molecular junction as a response to the suddenly switched bias voltages and we also address the question how the Coulomb interaction changes qualitatively these properties. We shall work all the time within the weak interaction regime to compare the physics to the results published for moderately strong interactions [1, 2]. For this purpose let us first consider the transport system (A) of Fig. 4.1. Let us first choose two-dimensional leads with 9 rows for the model. Later we shall also briefly address the effects of lead dimensionality to the currents and lead dynamics. To generate a finite current flowing through the system we drive the system out of equilibrium with a symmetrically applied bias voltages corresponding to near-resonance and far from resonance conditions. In Fig. (4.2) we show the transient right currents $I_R(t)$ flowing through the right interface between the molecular device and the lead together with the corresponding steady-state spectral functions $A(\omega)$ of the molecular region with different electronic self-energy approximations. For the self-energy, we choose HF, 2B, 2B without the second exchange diagram (labeled as 2B-2ndEX) and GW approximation. For the sake of completeness and interest, we also show the same curves for the noninteracting system to demonstrate the fundamental differences and contrast between the noninteracting and interacting systems.

In the left panels we show the results for bias voltage $W^l = -W^r = 0.9$ while the right panels contain the results for bias $W^l = -W^r = 1.5$. By looking at the top left panel, a first observation is that the transient and the steady-state currents are strongly dependent on the self-energy approximation. Let us first investigate the steady-state properties before analyzing the structures of the short-time transients. For $W^l = -W^r = 0.9$

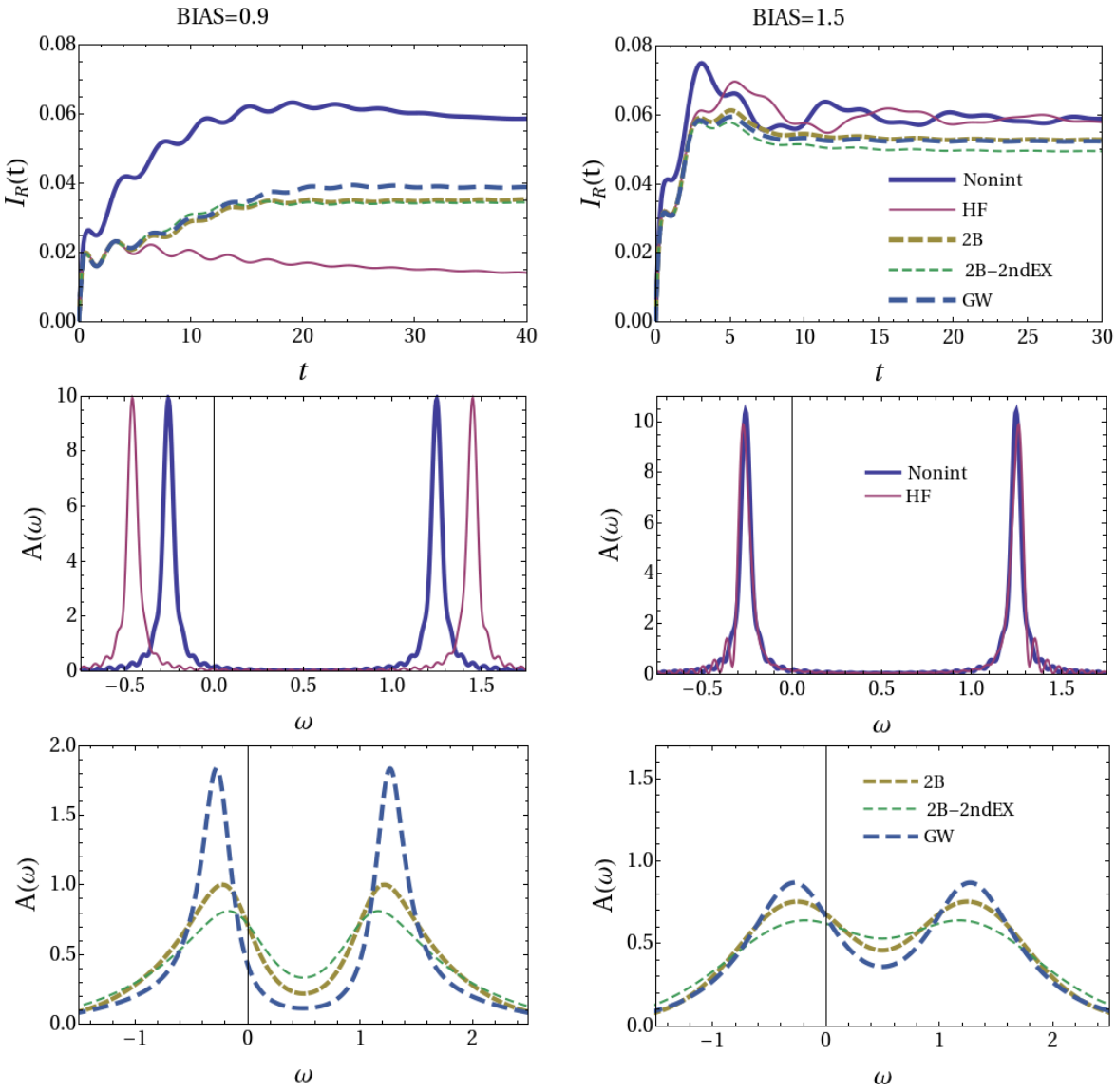

Figure 4.2: Transient right currents and steady-state spectral functions for noninteracting system, HF, 2B, 2B-2ndEX and GW approximations in the weak interaction regime, $U_0 = 1.0$. Left panels: bias voltage $W^l = -W^r = 0.90$, Right panels: bias voltage $W^l = -W^r = 1.50$. The chemical potential is $\mu = 0.5$.

the noninteracting system clearly produces the largest current while the HF steady-state current is remarkably smaller than the currents given by the correlated approximations. For stronger bias, $W^l = -W^r = 1.5$ however the noninteracting system and HF approximation behave very similarly and the steady-state values of the currents are equal. Moreover, the noninteracting and HF currents both are larger that the corresponding currents given by correlated approximations (2B, 2B-2ndEX, GW). To clarify this behavior more, let us first look at the steady-state spectral functions in the middle panels. It can be seen that for the mean field HF approximation, the steady-state gap

between the molecular quasiparticle levels is much larger than for noninteracting system[1]. This is easily understood, since the electron-electron interactions push the levels further out from each other and opens up the molecular gap compared to the noninteracting system. This is also the simple reason why the noninteracting system produces larger current for $W^l = -W^r = 0.9$ than HF: the steady-state current is directly proportional to the density of states (DOS) inside the conducting bias window region $[\mu + W^r, \mu + W^l] = [-0.5, 1.4]$. For HF approximation with bias $W^l = -W^r = 0.9$, the resonances are still outside the bias window at $\epsilon_1 \approx -0.5$ and $\epsilon_2 \approx 1.5$ which results as diminished DOS and blockage of the current flow. In other words, the current cannot flow through the molecular region without having any conducting channels in between the conduction bias region.

If we then look at the spectral functions for the higher bias value, $W^l = -W^r = 1.5$ (middle right panel) we see that the HF and noninteracting spectral functions are almost on top of each other: the HF molecular gap has collapsed in response to the large bias voltage whereas the noninteracting levels are independent of the bias voltage. The new non-equilibrium steady state levels are then positioned around $\epsilon_1 \approx -0.25$ and $\epsilon_2 \approx 1.25$. This phenomenon encapsulates the first qualitative difference between the interacting and noninteracting transport and has been investigated by Thygesen [44] and also in the research articles published for this thesis. The gap collapse in the interacting system is directly related to the polarization of the molecular region, *i.e.*, the charge balance between the occupied and unoccupied quasiparticle levels. Already in the HF level the finite interactions together with the changes in the level occupations collapses the molecular gap and changes the DOS (and consequently the current) *depending on the applied bias*. One can then say that for interacting systems, the spectral function $A(\omega)$ is also a bias dependent function $A \equiv A(\omega, W^{l/r})$.

[1]The noninteracting spectral function is shifted up in the frequency axis with 0.5 to make the equilibrium chemical potentials aligned. This has no effect on the physics of the system.

4.1.3 Transient and steady-state properties – effect of electron correlations

Let us then go beyond the noninteracting and mean-field approach and investigate the 2B and GW properties. As stated earlier, the correlated approximations produce larger currents already for the bias $W^l = -W^r = 0.9$. This phenomenon relates also to the bias dependent gap collapse but with the difference that the correlated non-equilibrium gap collapses for smaller biases compared to the mean-field HF approximation, and that the spectral functions broaden significantly. This is again one of the fundamental differences between the HF and correlated approximations in the context of quantum transport. In the 2B and GW level one accounts for the polarization (particle-hole excitation) processes which are strongly enhanced as the system is driven out of equilibrium while HF misses these effects completely. This enhancement of polarization due to increased quasiparticle scattering can lead to drastic broadening of the spectral peaks and more efficient charge distribution between the quasiparticle levels with smaller bias voltages than the HF approximation. This improved charge distribution between the levels then nourishes the gap collapse and increases the DOS inside the bias window which then results as larger currents. The results we see are in good agreement with the ones reported earlier [44]. As can be seen from the lowermost panels, the correlated spectral functions widen heavily compared to the noninteracting and mean-field HF spectra which retain their sharp features under both conducting and non-conducting conditions.

It is also interesting to compare the 2B results to 2B-2ndEX approximation where the second order exchange diagram is neglected from the self-energy. Although this approximation neglects the second order exchange process, it is however physically acceptable in a sense that is is also a conserving approximation and yields currents which obey the continuity equation. In this approximation it is then only the first bubble diagram which plays a role compared to mean-field HF approximation. We observe that for small biases, the 2B and 2B-2ndEX currents are on top of each other indicating that the second order exchange effects are almost negligible when the quasiparticle scattering is weak. Increasing the bias voltage we see a slight difference in the currents and correspondingly in the spectral functions as the current for 2B-2ndEX approximation is pushed down about 6% and the corresponding spectral function is also broader than the spectrum for the full second order approximation. It is then the second order exchange diagram which reduces the broadening of the spectral functions and corrects the spectral properties slightly towards the more exact values. It should also be noted that the GW approximation contains only the infinite series of polarization diagrams and neglects completely the higher order exchange effects. However, one would expect that the higher order exchange terms does not contribute significantly as already the second order correction has a marginal impact to the total value of steady-state current.

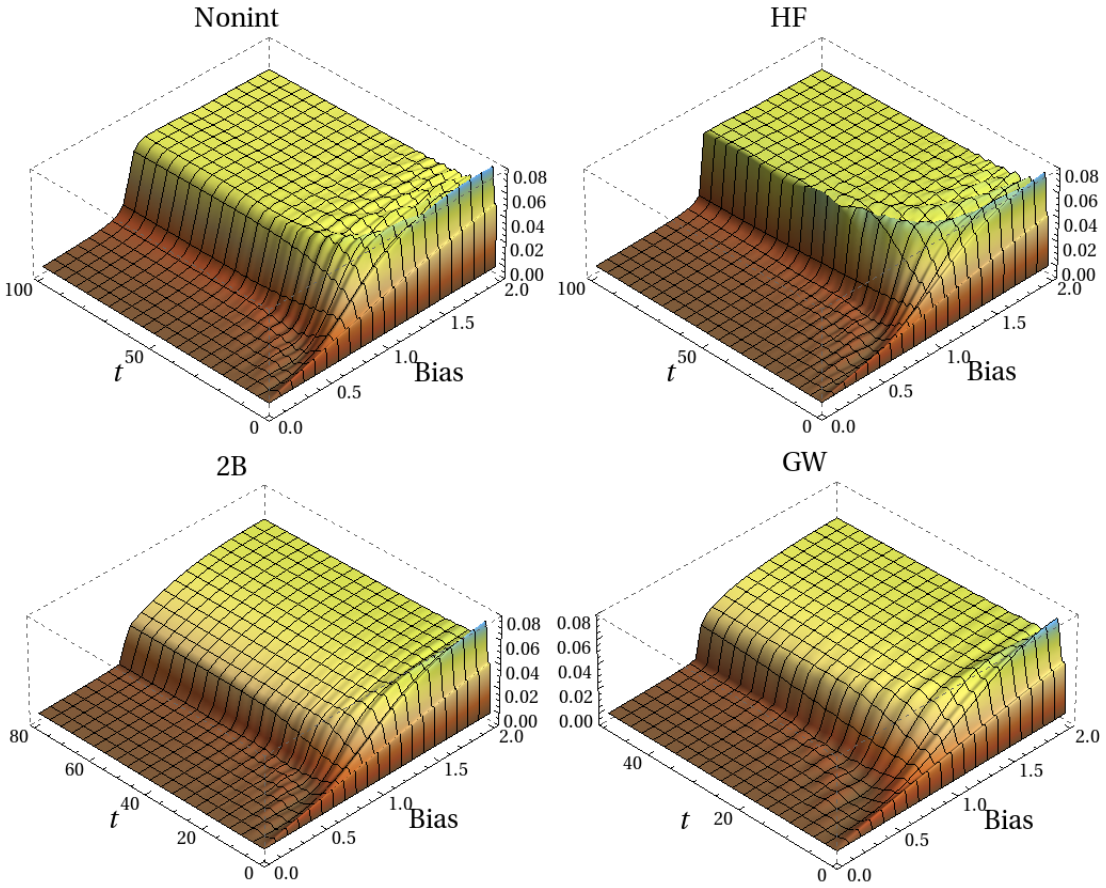

Figure 4.3: Transient right current vs. the applied symmetrical bias voltage and time for HF, 2B and GW approximations in the weak interaction regime, $U_0 = 1.0$.

4.1.4 Current–Voltage characteristics

In order to have a clear picture of the whole bias voltage regime, in Fig. (4.3) we also show the time-dependent right currents and in Fig. 4.4 the steady-state right currents I_R^S for bias voltage regime $W^l = -W^r \in [0,2]$ with the different approximations including the noninteracting system. It is clearly visible that both the noninteracting system and HF approximation produce a sharp jump in the current when the bias voltage hits the resonance while in the correlated approximations this jump is suppressed by the correlations. In the resonance conditions, the transient and steady-state currents have a quite large qualitative difference. After relatively long charging phase (for example the HF transients at the resonance) the currents settle to a steady state which is strongly dependent on the approximation as already stated earlier. It is clearly visible in the current–voltage characteristics how the resonance voltage (the quasiparticle gap) depends on the electronic self-energy approximation as the 2B and GW gap starts to collapse at $W^l = -W^r \approx 0.8$ while the HF gap follows the same trend at around

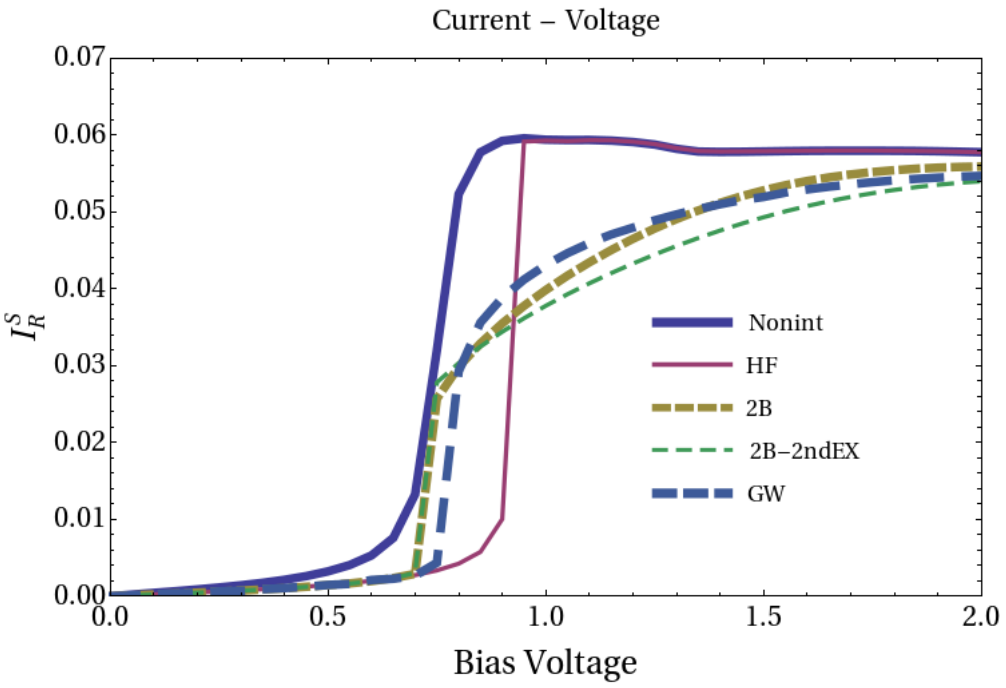

Figure 4.4: The Current-Voltage characteristics for the correlated two-site system with different approximations.

$W^l = -W^r \approx 0.95$. To see the spectral broadening effect as a function of the bias voltage, in Fig. 4.5 we also show the $A(\omega, W^l)$ for both Hartree-Fock and GW approxima-

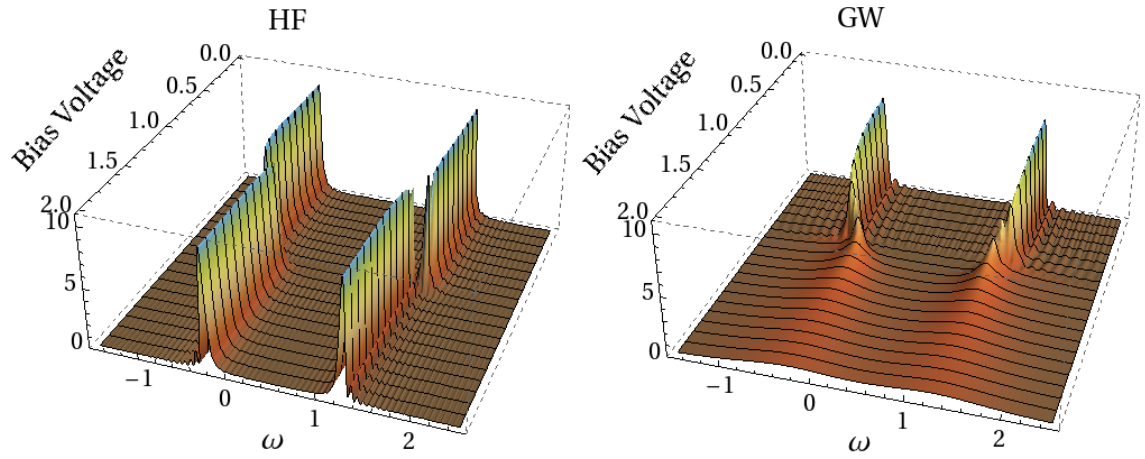

Figure 4.5: The bias-dependent non-equilibrium steady-state spectral functions $A(\omega, W^l)$ for the interacting central region in HF (left panel) and GW (right panel) approximations.

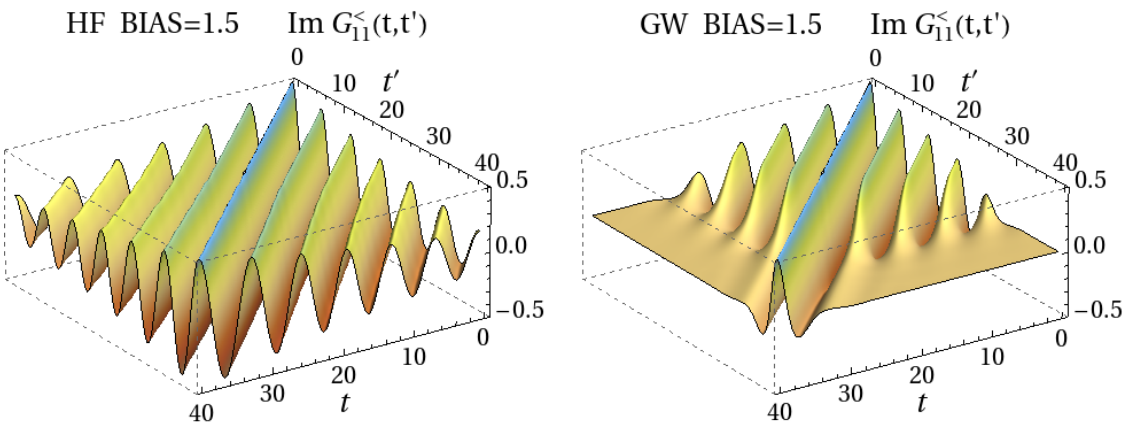

Figure 4.6: Imaginary part of lesser Green function at the site 1, $G^<_{11}(t,t')$, for HF (left panel) and GW (right panel). The system is propagated up to $t = 20$ a.u. before switching on a symmetric bias $W^l = -W^r = 1.5$.

tions (2B is very similar to GW). One can observe very well how the HF spectral peaks keep their sharp features after hitting the conducting bias window whereas the GW (and 2B similarly) broadens dramatically. This broadening then reflects to the current-voltage characteristics as a smooth increase of the current as the bias increases. In contrast, the HF I–V has almost no structure beyond the resonance bias voltage except a little jump around the bias value $W^l = -W^r \approx 1.3$ arising from the structural change of $\Gamma(\omega)$ of the two-dimensional lead around the frequency value $\omega \approx W^l$.

4.1.5 One-particle Green function and screened interaction

The significant collapse of the 2B and GW spectral function reflects also to the one-particle Green function and screened interaction $W(t,t')$. The former is demonstrated in Fig. 4.6 where we show the imaginary part of the lesser Green function for the first site in the central region, $G^<_{11}(t,t')$ in double time-plane. To emphasize the temporal structural change, the system is first propagated to $t = 20$ a.u. before switching on the symmetric bias voltage $W^l = -W^r = 1.5$ in the leads. The behavior of the Green functions are well in line with the observed spectral functions: the HF Green function stays oscillatory after $t = 20$ a.u. indicating a sharp peak structure but changes the frequency slightly whereas the 2B Green function damps very quickly after the switch-on. The damping time-scale is also relatively close to the time-scale it takes for dynamical observables like transient currents to reach a steady-state. Furthermore, the time-

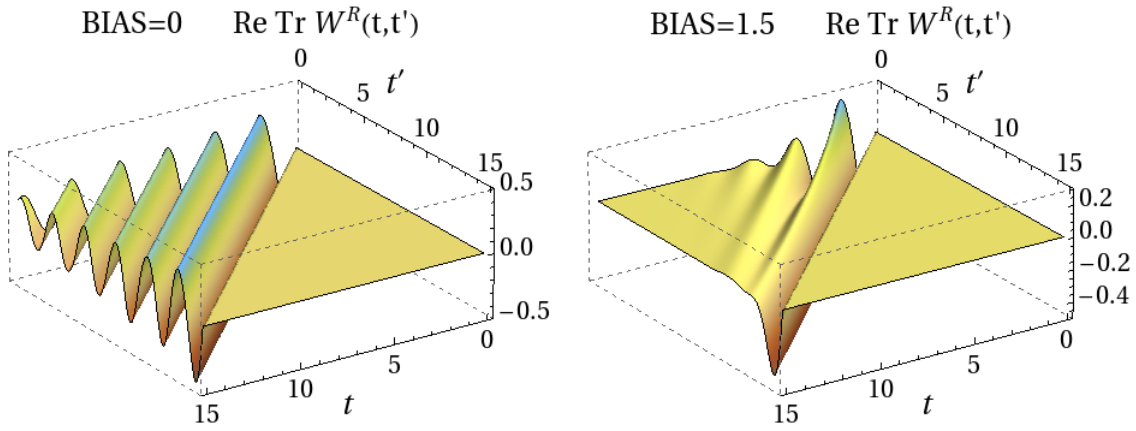

Figure 4.7: The real part of trace of the retarded screened interaction, $\mathrm{Re\,Tr}\, W^r(t,t')$ for ground state (left panel) and for high bias case $W^l = -W^r = 1.5$ (right panel).

diagonals of the lesser Green functions give directly the occupation number (per spin) of the site 1 which in both cases stay very close to equilibrium density.

In Fig. 4.7 we show also the real part of trace of the retarded screened interaction, $\mathrm{Re\,Tr}\, W^r(t,t') = \theta(t-t')\mathrm{Re\,Tr}\,[W^>(t,t') - W^<(t,t')]$ for the ground state (left panel) and for the high bias case (right panel). As we can clearly observe, the $W^r(t,t')$ becomes highly damped in the non-equilibrium situation, whereas in the ground state it remains as an oscillatory function with a small decay rate induced by the lead continua. This behavior is again related to the damping in the Green function. The W^r is also closely connected to the density response function: Since 2B and GW transients and steady-state results are very close, the screening process in the self-energy is dominated by the first particle-hole (bubble) diagram $P(t,t') = G(t,t')G(t',t)$. This diagram describes the response of the system to an external perturbation and it gives an approximate formula for the screened interaction $W(t,t') \approx w + wP(t,t')w$. As can be clearly seen, the retarded response indicated by the off-time-diagonal values of $\mathrm{Tr}\, W^r$ becomes also very weak due to the strong quasiparticle scattering and decreased lifetime of the quasiparticle states.

Let us briefly summarize the findings so far. We have found that the time-dependent features and steady-state properties of the currents are *strongly influenced* by the electron-electron interactions. This is also one of the most important messages of the research article [1] and [2] and is in good agreement with the previous studies on steady-state correlated molecular transport [44]. The electron interactions have a two-fold impact on the transport processes: on one hand, it causes the collapse of the molecular gap

arising from the polarization of the central molecular region and, one the other hand, broadens the resonances significantly when treated on correlated level within 2B or GW. Both features reflect to the electron/hole propagator and, consequently, to the spectral properties and screened interaction which become highly damped as the system is exposed to external driving fields.

4.1.6 Transient spectroscopy – fingerprints from the electronic transitions

Let us then turn our attention to the temporal properties of the individual transients. As we have already seen, the transients currents (as well as densities) have superimposed oscillations which can be traced back to the electronic transition properties of the equilibrium and non-equilibrium system. The transient oscillations originate from the electronic transitions between the biased Fermi levels of the leads and the ground state / non-equilibrium quasiparticle states of the central molecule and also from the internal electronic transitions inside the interacting molecular region. Furthermore, it is easy to understand from the previous analysis that the correlated approximation yield more damped transients especially in the high-bias regime. To demonstrate the transitions more clearly, we show in the Fig. (4.8) the transient site densities of the central region, denoted by $n_1(t)$ and $n_2(t)$ (panels a) and b)), transients dipole moments $d(t) = \sum_{i\in C} x_i n_i(t)$ of the central region (panels c) and d)) as well as their Fourier transforms $d(\omega)$ (panels e) and f)). The top panels imply that as the system is driven out of equilibrium, the molecular region gains a small but finite dipole where the charge accumulates to site 2 and depletes from site 1 while keeping the total amount of charge constant in the molecular region.

Fourier transforming the dipole moments we get access to the electronic transition spectrum of the system, which reveals that for the large bias regime the most dominant transitions occur between the molecular levels (peak 1)) and between the biased Fermi levels and the molecular levels (peaks 2) and 3)). For the bias $W^l = -W^r = 0.9$ the transition between the molecular levels is actually the most visible one and the other peaks are more or less suppressed. The diagram at Fig. (4.9) demonstrates the transitions of panel f) of the Fig. 4.8) which then also determine the temporal oscillations in the transient observables. The most dominant peak (peak 1) is smeared over a range of frequencies from 1.5 to 2.0 since the resonances are shifted dynamically from their ground-state positions $\epsilon_1 \approx -0.5, \epsilon_2 \approx 1.5$ (molecular gap $= 2.0$) to the non-equilibrium positions $\epsilon_1 \approx -0.25, \epsilon_2 \approx 1.25$ (molecular gap $= 1.5$) as the bias voltage is applied to the system. The peak 2 describes the low-energy transitions from the biased Fermi level of the left lead to the initially unoccupied level (LUMO) of the molecule as well as the transition from the initially occupied level of the molecule (HOMO) to the biased Fermi level of the right lead. This transition is also smoothened out over the

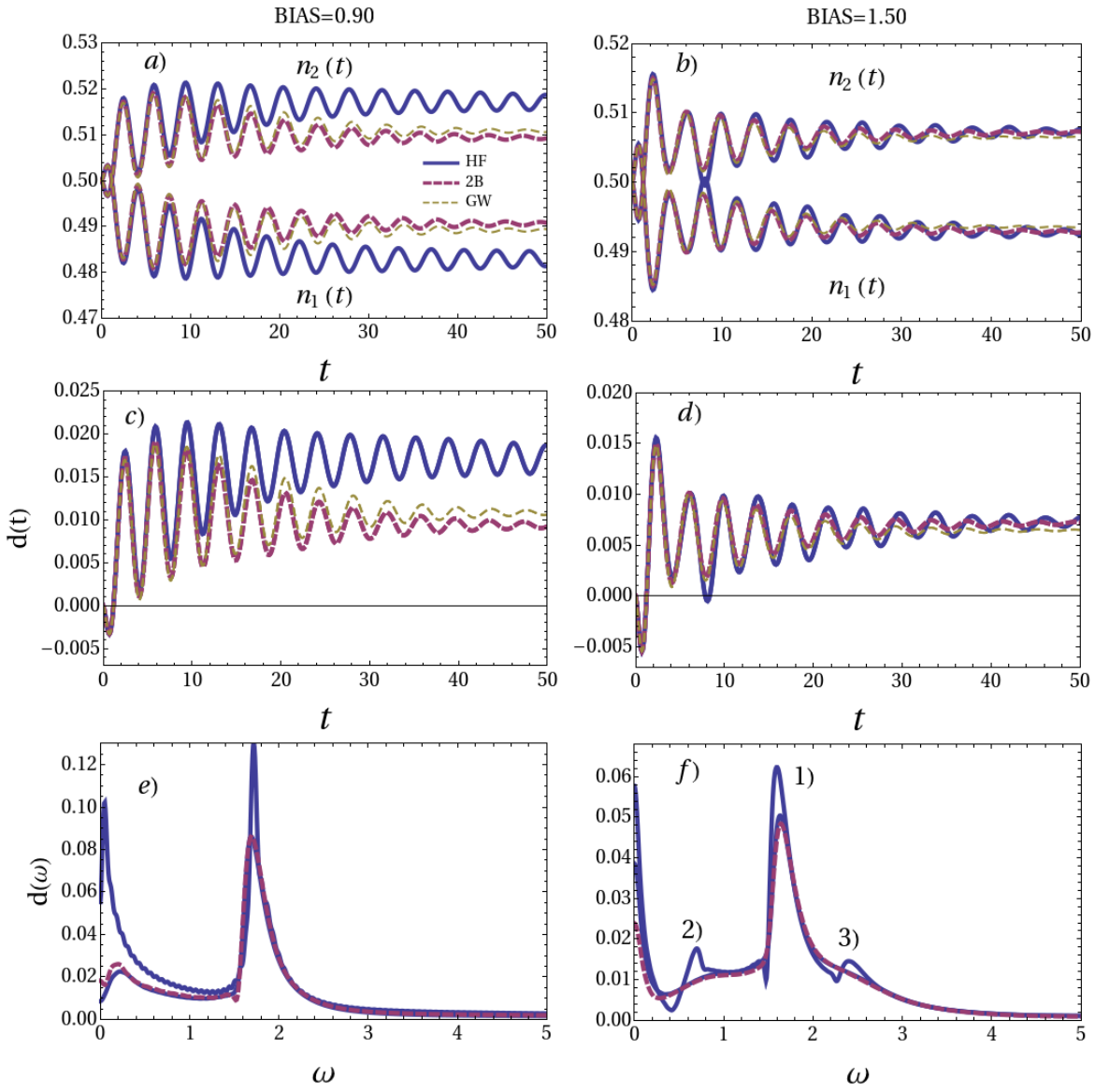

Figure 4.8: Transient site densities (panels a) and b)) dipole moments (panels c) and d)) and their Fourier transforms (panels e) and f)) under resonance conditions plotted using symmetrically applied bias voltages for HF, 2B and GW approximations in the weak interaction regime, $U_0 = 1.0$. The diagram in the Fig. 4.9 depicts the electronic transitions visible in the panel f).

energy range $\sim [0.5, 0.75]$ due to the renormalization of the molecular levels. The last peak (peak 3) describes the electronic transitions from the biased Fermi level of the left lead to the initially occupied level of the molecule and also from the initially unoccupied level to the biased Fermi level of the right lead with energy range $\sim [2.25, 2.5]$. The correlated approximations yield a similar spectrum although the peaks are subjected to much stronger damping due to the correlation effects. As we have showed in the research article [2], the transition spectrum becomes much more complicated

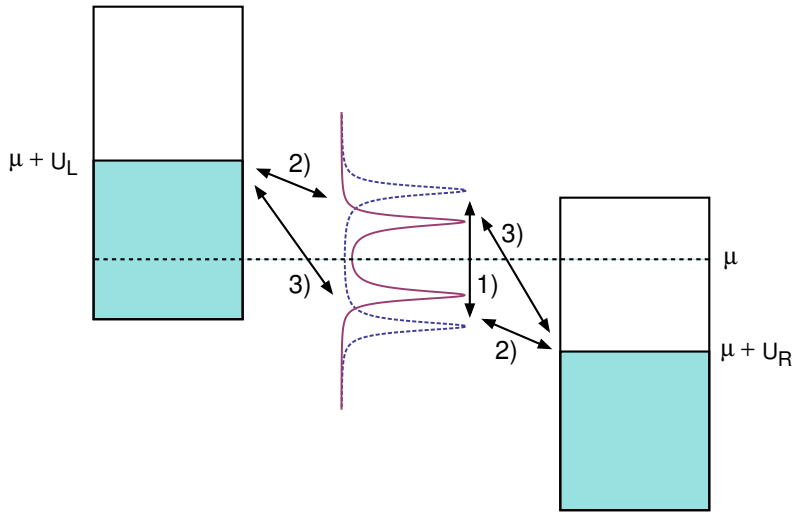

Figure 4.9: Electronic transition diagram corresponding to the panel f) of Fig. (4.8). The peaks closest to μ correspond to the nonequilibrium steady-state spectrum while the outermost peaks are the ground state spectral peaks.

for multilevel systems as there are more possibilities for electronic transitions to occur. From this analysis we can now conclude that the temporal properties of the transients contain a wealth of information on the underlying spectral structure of the molecular region in and out of equilibrium and also on the energetics of the electronic transitions occurring during the transport process.

4.1.7 On the time-scales of the transients

Returning back to the first plot (4.2), the time-scale of the transient current oscillations has a strong dependency on the applied bias and also on the approximation for the electronic self-energy. For noninteracting electrons, however, it has been shown that the transient time-scale is closely related to the $\Gamma(\omega)$ at the Fermi level [51] as the transient time-scale is proportional to $e^{-\Gamma t}$. Since Γ ($\Gamma \approx 2V^2/|b^\lambda|$ for 1D lead) effectively gives the lifetime $\tau \approx 1/\Gamma$ of a quantum state connected to semi-infinite lead, one can interpret it in real-time as the average time an electron spends on the level before getting dissipated into the leads. In the case of Coulomb interactions, the analysis complicates due to the levels shifts in non-equilibrium and especially due to the correlation effects which broaden the spectral functions and shorten the lifetime of the quasiparticle states. In this case one can, however, roughly approximate this time-scale with $\tau^{-1} \approx \Gamma + \mathrm{Im}\Sigma^{\mathrm{MB}}(\omega = \mu)$, where the imaginary part of the many-body self-energy gives the lifetime due to the correlation effects. It should be also noted that, apart from the bias dependent spectral broadening and gap reduction, the transient time-scale is also dependent on the resonance conditions, *i.e.*, whether the quasiparticle levels are

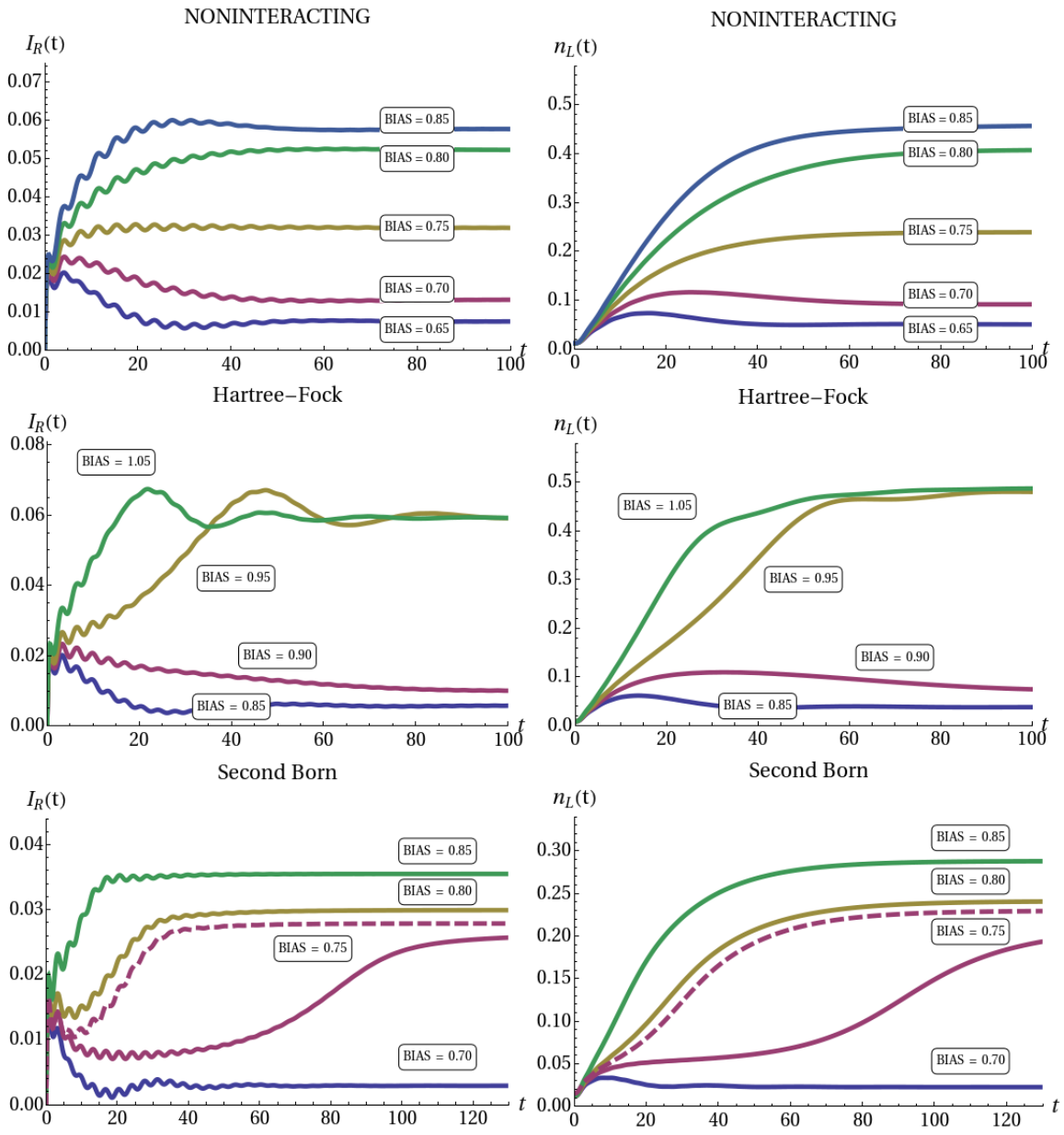

Figure 4.10: The transient right currents (left panels) and the corresponding occupation numbers (per spin) for the initially unoccupied level of central region (right panels) with different self-energy approximations. The bias voltages are chosen in a such way that the system is close to resonance conditions with the leads.

aligned with the biased Fermi levels of the electron reservoirs. This will be discussed next.

4.1.8 Resonance conditions

The resonance conditions can lead to nontrivial and relatively long charging times in the interacting systems. This is demonstrated in Fig. 4.10 for HF and 2B in comparison with the noninteracting system for several near-resonant bias voltages. In the left panels we show the transient right currents and in the right panels we show the time-dependent occupation numbers $n_L(t)$ (per spin) for the initially unoccupied (LUMO,L) level. The LUMO occupations are obtained by projecting the time-dependent density matrix $\boldsymbol{\gamma}(t) = -i\mathbf{G}^<(t,t^+)$ into the HF basis of the uncontacted central region. We first observe that the noninteracting current as well as the occupation of LUMO level increases steadily as the bias is increased under the resonance conditions. However, for Hartree-Fock a qualitative difference arises: The Hartree-Fock potential created by the charge density in the molecule starts to dynamically collapse the non-equilibrium gap as the system is charging, *i.e.*, the relative occupations of the HOMO and LUMO levels start to change, see for example the initial current and level occupation transient for bias $W^l = 0.95$. This initial charging phase accelerates the dynamical gap collapse with the result that the levels move inside the conducting bias window and the current increases. What then follows is a decaying, relatively long low-frequency oscillation originating from the transitions 2) and 3) of Fig. 4.9 and finally the current settles down to a steady-state. Increasing the bias voltage shortens the initial charging phase as the potential differences between the levels and the biased Fermi levels of the leads become finite. In other words, the levels are shifted inwards, away from the resonances with the leads. This then speeds up the initial charging process and the transient development is then dominated by the tunneling factor Γ.

The lowermost panels show a similar behavior also for the 2B approximation. In that case the charging phase can extend to more than 100 a.u.t to build-up the polarization charge which eventually collapses the molecular gap and brings the system to conducting state. For the purpose of interest, we also show the resonant current for the 2B-2ndEX approximation (dashed curve). It can be seen that the resonant charging time changes dramatically if we neglect the second order exchange correction to the self-energy. This is quite easy to understand since under the resonance conditions the system is very sensitive to slight changes in its configuration. However, the main point for this study is to address the existence of regimes where the different many-body effects/processes can have significant role in determining the time-scales for transients.

4.1.9 Dynamics of the leads

In the previous chapter we derived the embedded Kadanoff-Baym equations (3.40) and (3.41) together with the equation for the density dynamics for the lead regions

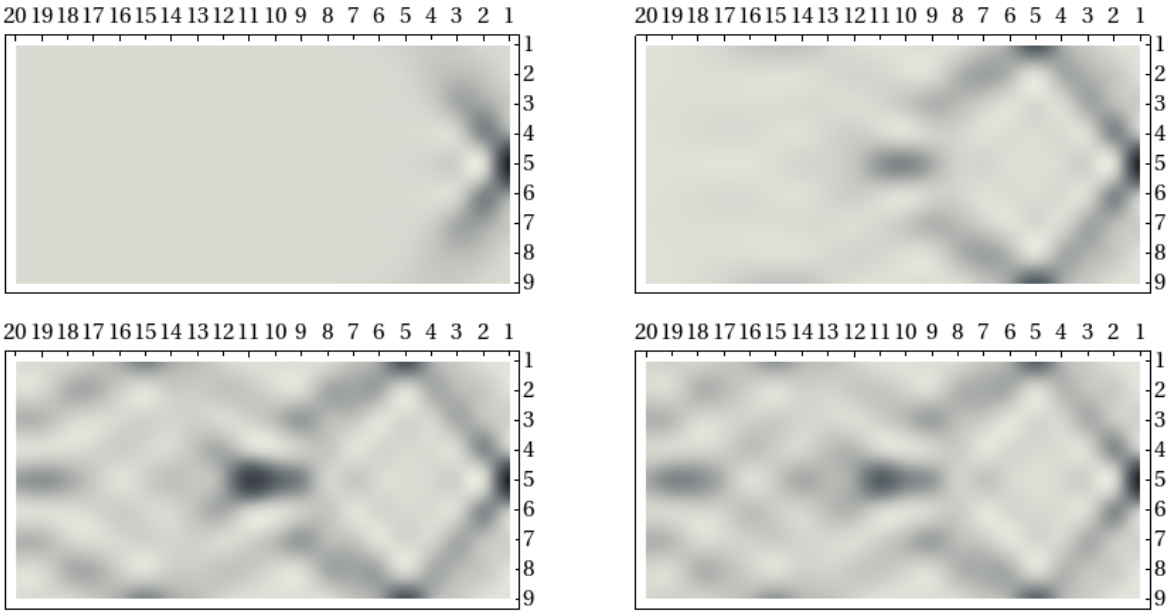

Figure 4.11: Time-dependent density distribution in the left electrode with 9 rows. Top left: $t = 1.0$, Top right: $t = 4.0$, Bottom left: $t = 7.0$ and Bottom right: $t = 15.0$.

(3.78). It is then interesting to demonstrate how the electron densities develop in the lead regions, since it helps to draw more detailed picture of the whole electron transport process through a narrow quantum system. Furthermore, it also provides a simple approach to stress the commonly used assumption that the lead regions remain in thermal equilibrium during the transport process. In the research article [2] we calculated the lead density dynamics for a two-dimensional lead with the width of 9 rows. As a comparison, it is interesting to see how the width of the electron reservoir affects the time-dependent density pattern observed in the lead. For this purpose we show in Figs. 4.11, 4.12, 4.13 the density distribution snapshots, $t = 1.0, 4.0, 7.0$ and $t = 15.0$ for the two-dimensional left leads with different widths, $R = 9$ (Fig. 4.11), $R = 5$ (Fig. 4.12) and for $R = 3$ (Fig. 4.13) and for 2B approximation. In these plots, the vertical index enumerates the rows and the horizontal index denotes the atomic layer which increases when moving deep inside the lead. In all cases, the correlated central wire is attached to the lead via a single link to the terminal site of the middle row (the dark area in the middle of the right edge).

A common feature for all the leads is that the charge is depleting from the leads via diamond-shaped pathway. This pathway essentially describes the spatial distribution of the Fermi surfaces in the half-filled semi-infinite leads. The zigzag-pathway is most clearly visible close to the right edge of the lead where the charge depletion is the strongest and it becomes slightly broken deeper in the lead where the electron waves flowing via different paths interfere. Furthermore, decreasing the width of the leads, also the depletion of the charge density increases which is natural since decreasing the

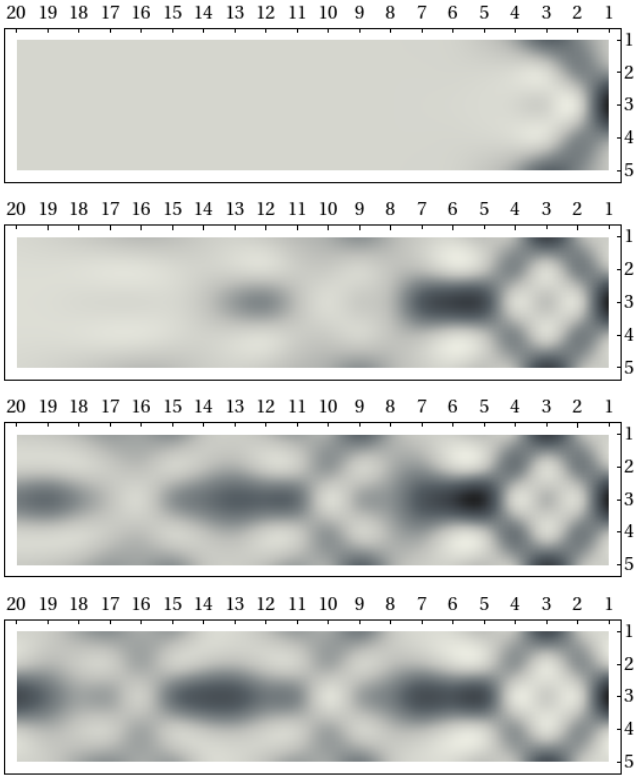

Figure 4.12: Time-dependent density distribution in the left electrode with 5 rows. Top left: $t = 1.0$, Top right: $t = 4.0$, Bottom left: $t = 7.0$ and Bottom right: $t = 15.0$.

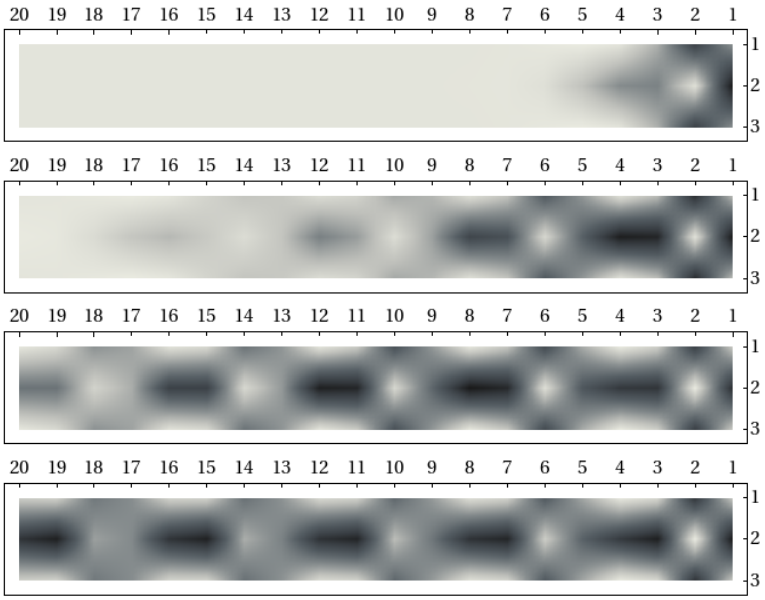

Figure 4.13: Time-dependent density distribution in the left electrode with 3 rows. The time-indices from top to bottom: $t = 1.0, 4.0, 7.0$ and $t = 15.0$.

lead width the surface area through which the charge density flows is also diminished. One can from the Figures 4.11 and 4.12 also observe a density pattern which is best visible near the "impurity" site which is coupled to the central region. This density pattern describes the Friedel oscillations which arise exactly from the impurity site at the edge of the lead: the electrons scatter from the impurity potential and interfere with the incoming electron waves. This interference then forms the deviation pattern in the electronic density which is enhanced by the non-equilibrium conditions. These oscillations are not visible in the ground state due to the weak coupling to the leads since the weak coupling diminishes the impurity effect to the terminal site of the lead and renders the Friedel oscillations negligible.

In Fig. 4.14 we also show the cross-section site densities for the different leads at different times during the transient phase. The cross-sections are taken in the middle along the longitudinal lead axis. In the horizontal axis the site index then refers to the site index along the cross section starting (i=1) from the terminal site which is linked to the central region and ending 20 layers deep inside the lead. The times corresponding to the different panels are $t = 1.0, 4.0, 7.0$ and $t = 15.0$ starting from top left and ending to bottom right panel. First one notices that the dynamics of the one-dimensional lead differs remarkably from the two-dimensional leads as the charge depletion is much

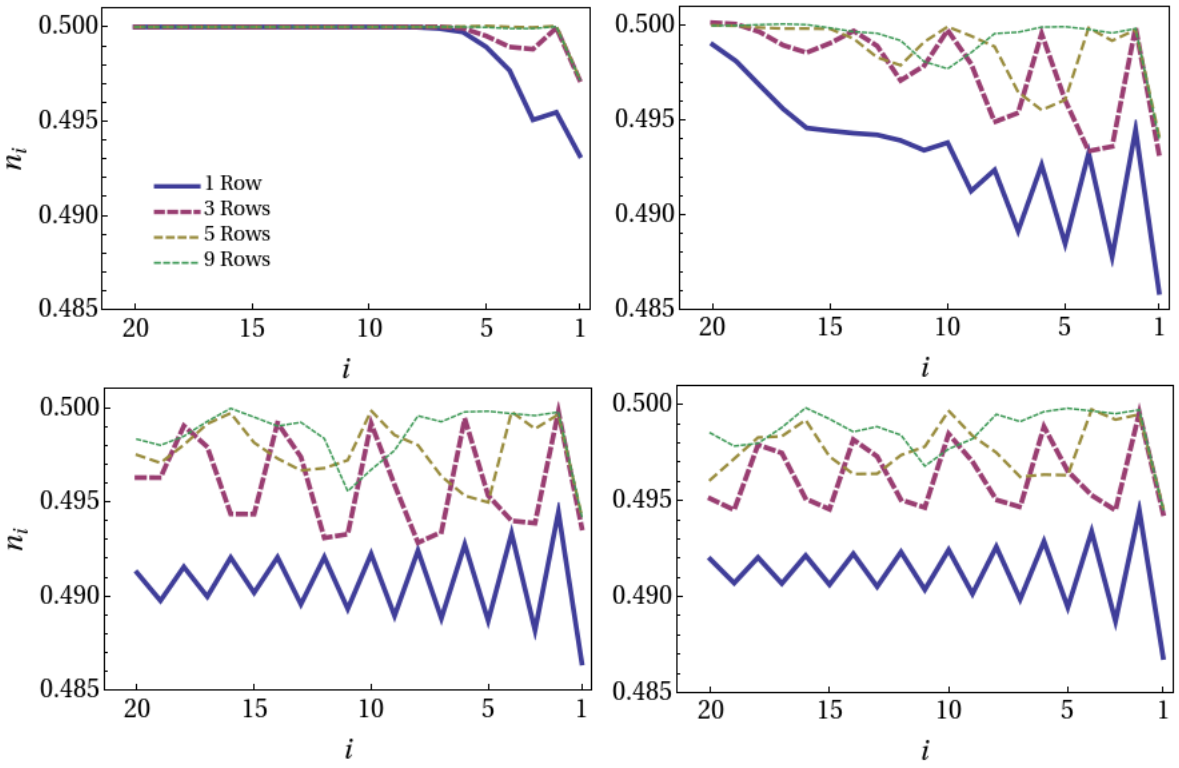

Figure 4.14: Cross-section site densities for leads with different width for different times. Top left: $t = 1.0$ top right: $t = 4.0$, bottom left: $t = 7.0$ and bottom right: $t = 15.0$.

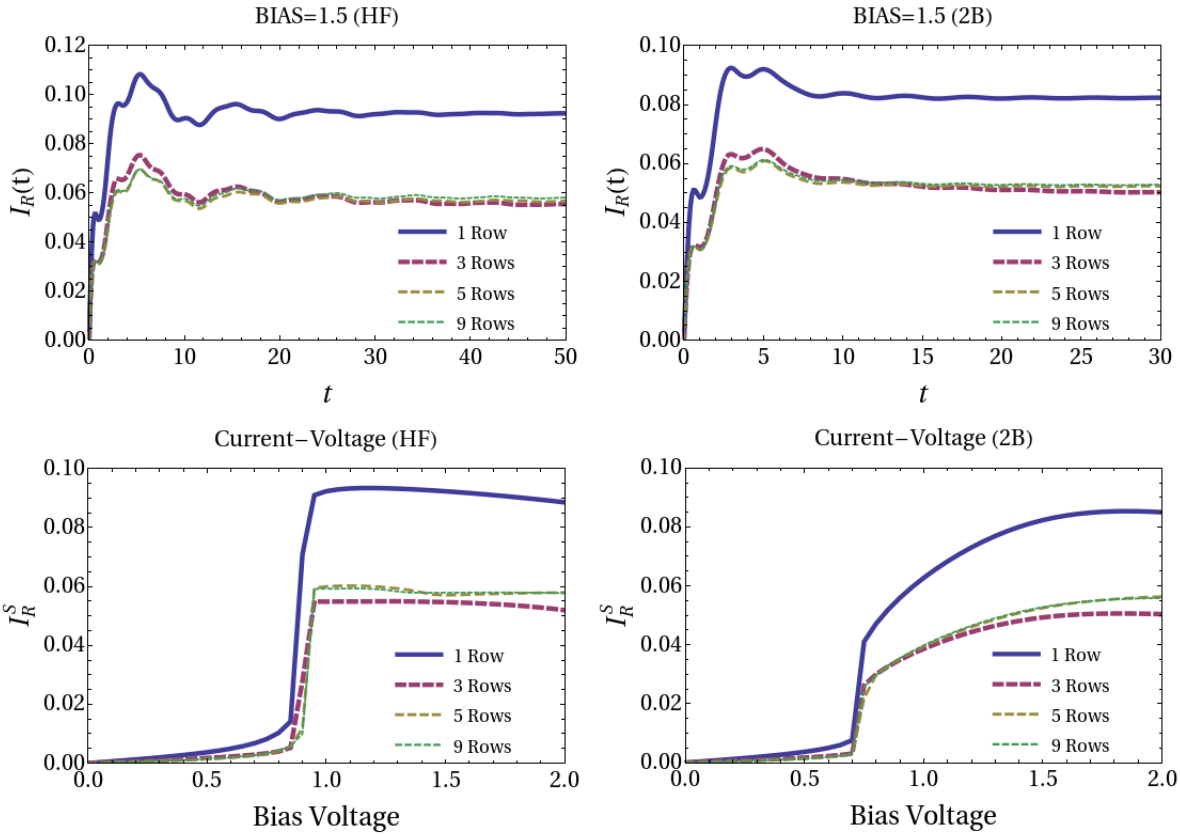

Figure 4.15: The influence of the lead dimensionality on transient currents for HF (top left) and 2B (top right). The bottom panels show the I–V curves for one-dimensional leads (1 Rows) and for two dimensional leads (3,5 and 9 Rows).

stronger for 1D leads. One can also observe the characteristic Friedel oscillation pattern for the one-dimensional lead as the decaying density oscillates at every second site according to $\cos(2k_F x)/x$, where $k_F = \pi/2$ for the one-dimensional semi-infinite half-filled lead and x is the distance from the terminal site [87].

We can also clearly observe how the width of the lead affects the charge depletion: increasing the width, the density deep inside the lead approaches the equilibrium density 0.5 and after 10 layers the density of the 9-row lead stays closest to the equilibrium distribution with only 0.4% deviation from the equilibrium. From these results we can directly verify that the common assumption that the leads remain in thermal equilibrium once the bias voltage is switched on, holds very well for the simulations performed here. For HF approximation, the charge deviations (not shown here) are slightly larger due to the larger current response for the selected bias voltage.

4.1.10 Lead dimensionality and currents

Before completing this section, the figure 4.15 finally demonstrates how the single transient currents and the current-voltage characteristics are affected by the dimensionality of the leads. In the top panels we plot the single transient currents for bias voltage $W^l = -W^r = 1.5$ for HF and 2B approximations with the lead widths $R = 1, 3, 5$ and $R = 9$. As we can clearly see, the temporal structure of the transients is not strongly affected by the dimensionality while the steady-state current is remarkably altered due to the diminishing of the coupling factor Γ as the dimensionality changes (see Figs. 3.3 and 3.5).

4.2 Initial state dependence and Initial correlation effects

The (embedded) Kadanoff-Baym equations come with a built-in initial correlation contributions, which manifest themselves in the set of integral equations (3.46), (3.47), (3.48) and (3.49). The initial correlations can basically be separated into two pieces. On one hand one can speak of initial correlations with the reference to the initial electron-electron interactions in general, but on the other hand one can refer to the time-nonlocal correlations present in the real-time propagation of the Kadanoff-Baym equations which have their origin in the initial state of the system. In the latter case, these initial correlations arise from the collision integrals where the time-integration is performed with the mixed-time components $(\rceil, \lceil)$ over the imaginary track of the Keldysh contour. In the case of mean-field HF approximation, this kind of *electronic* initial correlation effects are absent and the only contribution from the initial state arise from the initial embedding effects. These initial embedding effects account for the memory of the initial contacting, *i.e.*, the physical hybridization to the leads while the initial e-e correlation effects describe the memory of the possible Coulomb interactions present in the initial state. In the long-time limit, when the temporal separation of the time-indices in $G^{\rceil,\lceil}$ and $\Sigma^{\rceil,\lceil}$ increase, the contributions arising from the initial correlation effects vanish and do not contribute to the steady-state properties. It is then the transient structure where we expect to see changes as we neglect these correlation factors.

To demonstrate the implications of the initial electron-electron interactions and initial correlation effects to transients, we show in Fig. 4.16 the transient right currents for HF and 2B approximation for the high bias regime (top panels) and also for the resonant biases $W^l = -W^r = 0.91, 0.95$ (HF, bottom left panel) and $W^l = -W^r = 0.75$ (2B, bottom right panel) together with the transients where we neglect the initial correlation terms. For HF approximation, these initial correlation terms consist only on em-

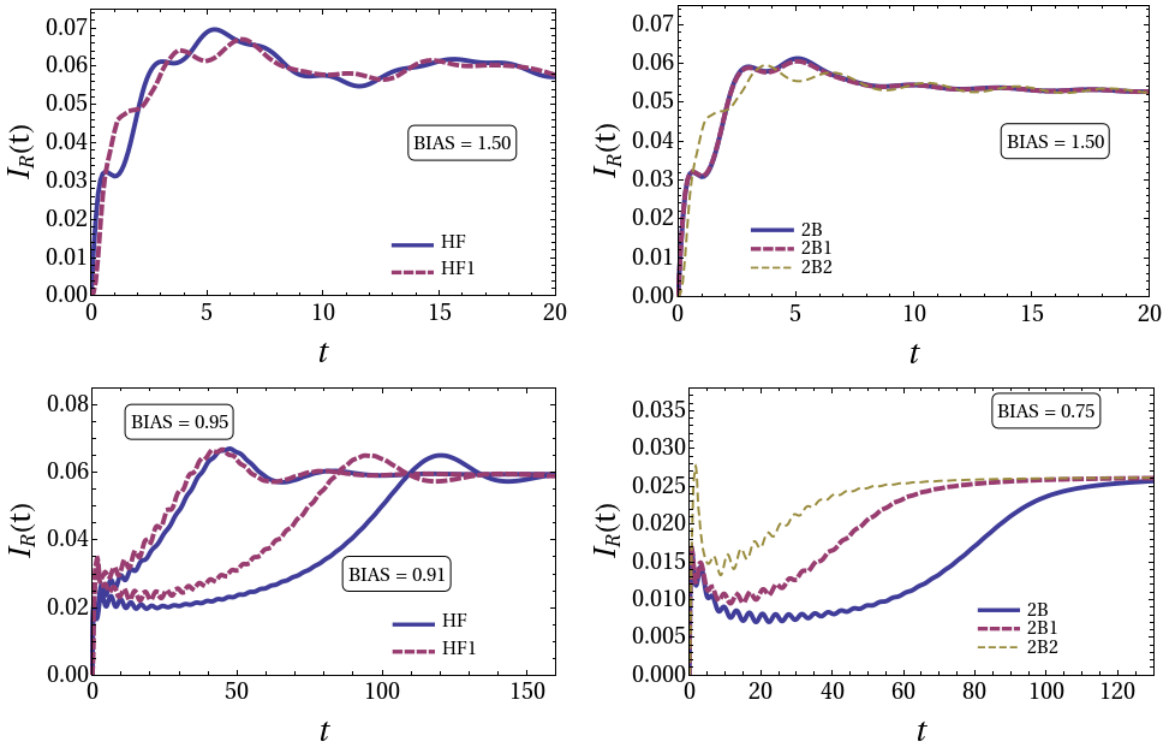

Figure 4.16: The effect of initial correlation and embedding effects on transient currents. In the top panels, a bias of $W^l = -W^r = 1.50$ is used while in the bottom panels the system is brought into resonance with the biases $W^l = -W^r = 0.91, 0.95$ (bottom left, HF) and $W^l = -W^r = 0.75$ (bottom right, 2B).

bedding self-energies $\Sigma_{\rm em}^{\rceil,\lceil}$ while the correlated approximations have initial correlation contributions from both the embedding self-energies and the many-body correlation self-energies $\Sigma_{\rm MB}^{\rceil,\lceil}$. We refer the HF curves without the initial embedding self-energies as HF1. Furthermore, for 2B approximation, the curves including the initial embedding self-energy but neglecting the initial many-body self-energy terms are labeled as 2B1 and the curves neglecting both the initial embedding and e–e correlation terms are labeled as 2B2.

We see that for the high bias region both the HF (top left panel) and 2B (top right panel) approximation have a weak dependence on the initial correlation and embedding effects. The neglect of the initial embedding effects leads to very similar dynamics as the full solution for the current and the only practical difference is that the oscillations occur at different phase. The same effect happens for 2B approximation. Furthermore, we also see that for 2B the initial electron-electron correlation effects are almost negligible. These observations can be easily explained by remembering that we are investigating the effects arising from the weakly coupled molecule with relatively weak interaction parameters ($U_0/|b^\lambda| = 0.4$). Furthermore, for this large bias regime, the system is also far from resonance and the initial charging time is relatively short especially for 2B

approximation. This then renders the initial correlation effects relatively ineffective for the short timescales.

Let us then focus on the bottom panels where we show the similar plots for HF and 2B but for the resonance conditions where the levels are aligned with the biased Fermi levels of the leads and long charging times take place. We see that for HF approximation, neglecting the initial correlations increases the transient currents slightly while keeping the dynamical structure very similar (bias 0.95). By tweaking the bias voltage in such a way, that the temporal charging times increase, we start to see much larger changes in the currents (bias 0.91). For the 2B case we observe much more drastic behavior. Neglecting the initial e-e correlations in 2B shortens the charging time remarkably (2B $\rightarrow$ 2B1). Similar effect happens also if we further neglect the initial embedding effects which then shortens the charging phase roughly with a factor of two compared to the full transient current including both the initial embedding and electronic correlations. As we have seen earlier, the transient transport features are quite sensitive under the resonance conditions which also explains the quickening of the charging times as the initial correlation terms are neglected. It is then a clear demonstration that these terms act as dissipative quantities in the equations of motion and in the equation for the time-dependent current which slow down the temporal charging processes. The above results also show that even though we work in the relatively weak interaction regime it is possible to point out the importance of the initial correlation and embedding effects on the transients. The take-home message of this study is that the time-dependent quantum transport simulations are very sensitive to the initial conditions and one should properly account for both the equilibrium embedding and electronic correlation effect in the time-propagation. Otherwise, one may obtain transient features with remarkable discrepancies.

4.3 Lead interactions and image charge effects

So far we have demonstrated some basic properties of time-dependent transport process when the electron-electron interactions are restricted only to the central scattering region. As we have seen, the transient and steady-state DC transport properties of these models are strongly dominated by the structure of the contacts together with the many-body effects which lead to bias dependent gap closing and renormalization of the quasiparticle levels of the molecular region. The question arises, that how these features change if we account for the Coulomb interactions between the molecular region and the electron reservoirs? It has been demonstrated both experimentally [88, 89] and theoretically [90, 91, 92, 93, 45, 46] that the gap between the highest occupied molecular orbital (H,HOMO) and lowest unoccupied molecular orbital (L,LUMO) can reduce dramatically when the molecule is brought into the vicinity of a metallic conducting surface. This reduction of the gap is due to the image charges which are formed in the metallic surfaces and is present even the molecule has only a capacitive coupling to the surface charges. In this sense, the image charge formation is purely a property of the long-range interaction between the molecule and the conducting surface. It is therefore expected that the image charge formation changes remarkably both the transient and steady-state transport properties.

In the research article [3] we investigated these effects in the time-domain by using a simple two-level system inspired by earlier studies on the topic [45]. Firstly, a few words are in place to clarify how to treat this problem within the Kadanoff-Baym formalism. To start with, we use the transport model B) of Fig. 4.1 with the Hamiltonian (3.26) where we consider the molecular region together with the interacting terminal sites of the leads as the interacting central region. The one-body part and the interaction part of this "hybrid" central region can then be written in the matrix notation as

$$[h]_{ij}(t) = \begin{pmatrix} -2U + W^l(t) & V_l & V_l & 0 \\ V_l & \epsilon_H - 2U & 0 & V_r \\ V_l & 0 & \epsilon_L - 2U & V_r \\ 0 & V_r & V_r & -2U + W^r(t) \end{pmatrix}, \tag{4.1}$$

$$[w]_{ij} = \begin{pmatrix} 0 & U & U & 0 \\ U & U_0 & U_{HL} & U \\ U & U_{LH} & U_0 & U \\ 0 & U & U & 0 \end{pmatrix}, \tag{4.2}$$

where the rows and columns of these matrices are indexed from left (top) to right (bottom) as $i = 1_l, H, L, 1_r$. Here the indexes $i = 1_l$ and $i = 1_r$ refer to the interacting terminal sites of the leads. Furthermore, the factors $-2U$ at the terminal sites arise from the positive ionic background of the molecular region whereas the corresponding

$-2U$ terms at the molecule come from the positive background of the terminal sites. Furthermore, $W^l(t)$ and $W^r(t)$ are the time-dependent local potential terms due to the bias voltage which is also applied to the interacting terminal sites. Now, since the interacting terminal sites are included to the hybrid central region, the embedding self-energies are given by $\Sigma_{\mathrm{em},11}(z,z') = |b^\lambda|^2 g_{\alpha\alpha,22}(z,z')$. Here the lead hopping elements b^λ act as the coupling matrix elements that capture the dynamics of the lead Green functions $g_{\alpha\alpha,22}(z,z')$ at the terminal noninteracting lead sites 2 to form the embedding self-energy to the central region.

4.3.1 Image charge effect and spectral properties

Before starting with the time-dependent transport, let us briefly introduce how the image charge formation changes the spectral properties of the molecule when it is Coulomb-interacting with the metallic surface of the lead. For this purpose, let us analyze the situation where the molecule is interacting only with a single metallic surface modeled with a semi-infinite tight binding lead. The Figure 4.17 shows the behavior of the ground state spectral function of the molecule for different approximations and for different interaction strengths $U = 0, 0.5, 1.0$ and for $U = 1.5$ when the molecule is hybridized to the conducting metal surface with a coupling strength $V = -0.2$. The first observation is that the correlated approximations have a very different qualitative behavior compared to mean field HF as the interaction strength is increased. For the HF approximation the HOMO and LUMO spectral peaks move slightly apart from each other, *i.e.*, the gap between the molecular levels opens up whereas for the correlated 2B and GW approximations the gap starts to close as the molecule-lead Coulomb interaction is increased. Another feature which is actually more or less common for all the approximations is that the intensity of the spectral peaks decreases when the interaction U increases.

Let us investigate the HF case first. The broadening and outward shifting of the HF spectral peaks is related to a collaborative effect of the Coulomb interaction and hybridization between the molecular levels and the leads. In fact, as we have shown in detail in research article [3], the key processes that are responsible for the spectral peak broadening are the first order exchange processes $\Sigma_{H1} = UG_{H1}$ and $\Sigma_{L1} = UG_{L1}$. These terms are nonzero only for nonzero hybridizations V and, for the finite lead-molecule Coulomb interactions, they renormalize the coupling matrix elements $V \to V + UG_{H/L1}$ and, furthermore, the whole embedding self-energy as

$$\Sigma_{\mathrm{em}} \to 1/(1-UC)^2 \Sigma_{\mathrm{em}}. \tag{4.3}$$

Here C is just a constant which is weakly dependent on U for small U values. This renormalization provokes a significant increase of the embedding self-energy which then flattens the spectral peaks and moves them slightly outwards (see Fig. 3.3) from

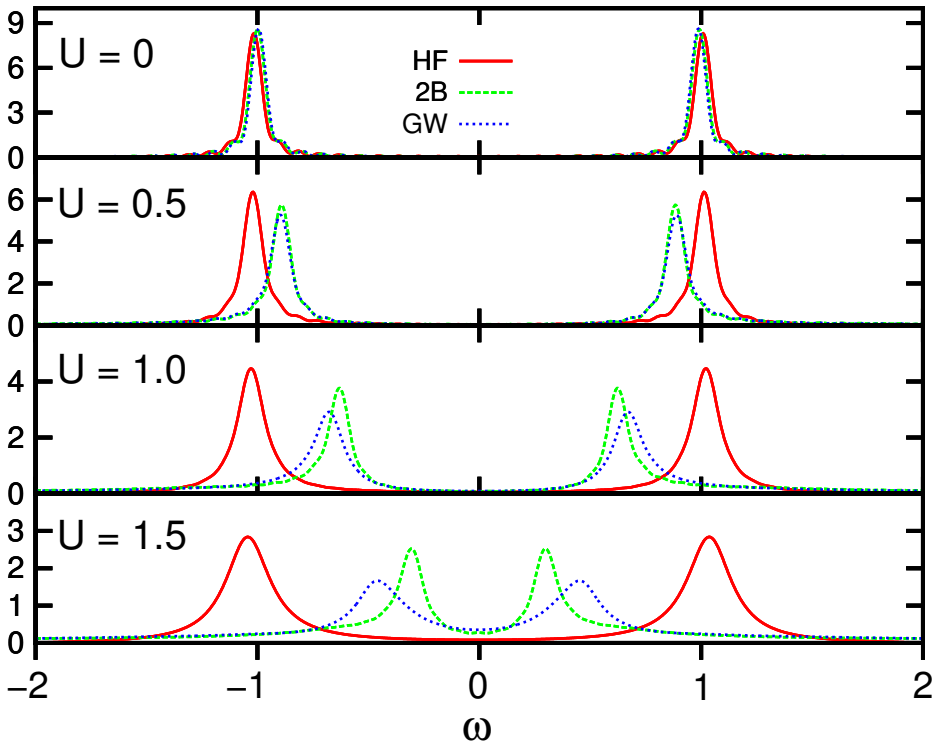

Figure 4.17: The equilibrium spectral functions for the HF, 2B and GW approximations with different molecule-lead interaction strengths $U = 0, 0.5, 1.0$ and for $U = 1.5$. Here the lead hopping is $b^{\lambda} = -1.0$ with hybridization $V = -0.2$.

the original positions corresponding to $U = 0$. In the case of zero hybridization, no renormalization occurs and the HF spectral peaks are completely independent on the lead-molecule interaction.

The situation changes for 2B and GW approximations. The gap closing in the 2B and GW level compared to the HF encapsulates again the fundamental differences between the mean-field approach and the correlated 2B and GW approximations: 2B and GW account for the polarization, *i.e.*, the formation of the particle-hole pairs while the HF accounts only the Hartree and exchange effect in the interacting "hybrid" region. In other words, the more sophisticated 2B and GW approximations are able to account for the polarization of the metallic lead while HF lacks completely this effect. To understand this polarization process more intuitively, one can think of adding an extra electron to the LUMO level of the molecule. In the 2B and GW level this extra electron couples not only to the density at the terminal site (HF), but also to the whole particle-hole continuum of the lead region which is described by a single polarization bubble diagram at the terminal site of the lead. This particle-hole continuum (bubble diagram) describes now the charge-neutral excitations of the lead as a response to the added electron to the LUMO. This excitation process depletes the charge density from the terminal site of the lead leaving behind a positive ionic background which then screens out the excess

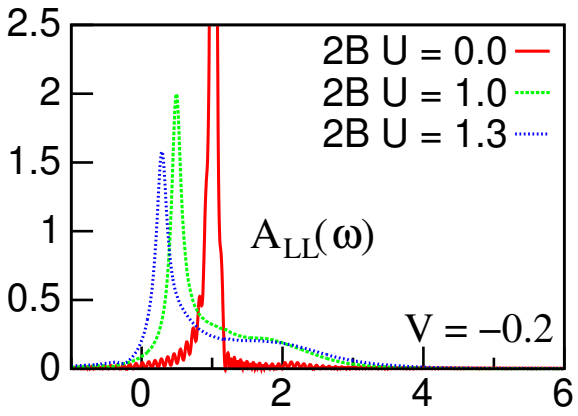

Figure 4.18: Ground state satellite spectrum above the main LUMO spectral peak for 2B approximation. The molecule-lead hybridization strength is set to $V = -0.2$ and the lead hopping parameters $b^{\lambda} = -0.6$

charge of the added electron. It is this screening process which then lowers the addition energy of the LUMO level and renormalizes the molecular gap. It has been shown by Thygesen [45] and by us [3] that GW approximation is able to describe the image charge formation very accurately and agrees very well with the exact results.

The charge depletion (excitation) from the terminal site of the lead is now exactly the process of image charge formation and it appears in the correlated spectral functions as long tails above (below) the main LUMO (HOMO) peaks. These tails describe the continuum contribution of the different excited states of the lead to the spectral function and the intensity of this satellite spectrum depends strongly on the molecule-lead interaction and the response function P of the lead ($P \approx$ bubble diagram $\sim 1/b^{\lambda}$ for 1D

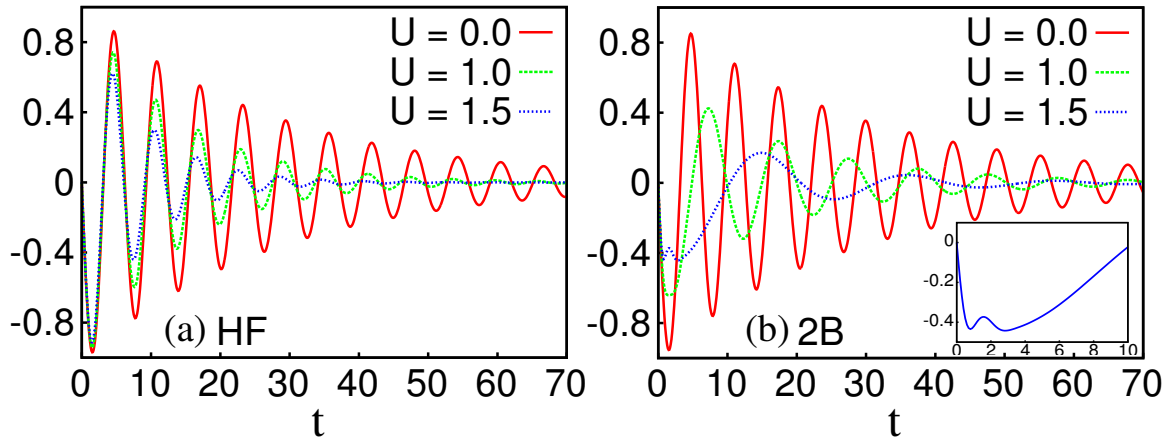

Figure 4.19: The greater Green functions $G^{>}_{LL}(t,0)$ for HF (panel a) and 2B (panel b) approximations for $U = 0.0, 1.0, 1.5$. The lead hopping is set to $b^{\lambda} = -1.0$ and the coupling constant is $V = -0.2$. The inset shows the initial transient of the $U = 1.0$

lead). This satellite spectrum is emphasized more clearly in Fig. 4.18 where we show the LUMO spectral function for 2B approximation for different molecule-lead Coulomb interaction strengths and for a narrow-band lead with $b^\lambda = -0.6$. The shoulder above the main peak has width of $4|b^\lambda|$ equal to the bandwidth of the lead and the shoulder becomes more pronounced as a function of the interaction strength.

All the above spectral features induced by the finite hybridization together with the Coulombic molecule-lead interaction reflect to the temporal structure of the Green functions. The figure 4.19 illustrates these features for the real part of the greater Green function $G^>_{LL}(t,0)$ for both HF (left panel) and 2B (right panel) approximations. We clearly see that the broadening of HF spectral peaks originate from the heavily damped Green functions with a renormalized relaxation time-scale $\tau_{\rm rel} \sim \Gamma^{-1}(1-CU)^2$ as U increases. Similar feature is also present for 2B with the difference that a small transient develops in the early beginning of the curve corresponding to $U = 1.5$. This transient phase can be identified as the build-up process of the image charge which is a process with time-scale $\tau_{\rm scr} \sim 1/|b^\lambda|$. We can now conclude that the lead-molecule hybridization and Coulomb interaction can significantly change the competing time-scales between the relaxation (tunneling time-scale) and the screening (image charge formation) processes.

4.3.2 Transients and steady-state properties: HF study

Let us next move on to investigate how the lead interaction effects change the non-equilibrium transport properties. It is natural to first discuss the properties on the HF level and then continue with the more sophisticated 2B and GW approximations. The figure 4.20 shows the short-time transient right currents for HF approximation for a range of bias voltages $W^l = -W^r \in [0, 1.2]$ and for different strengths of the molecule-lead interaction $U = 0.0, 0.5$ and $U = 1.0$. The bottom right panel also shows the current-voltage characteristics corresponding to the different panels. In the case of $U = 1.0$ the HF currents remain very oscillatory and the corresponding steady-state current values are the average values around which the oscillation happens. The top left panel ($U = 0.0$) shows a typical bias sweep with already well known properties for the transient and steady-state currents: vanishingly small electron flow through the system until the bias voltage reaches the resonance (around $W^l = -W^r \approx 0.85$) which results as a sudden jump in the I-V curve and lengthened charging times. By introducing a finite Coulomb interaction between the molecular levels and the leads, the behavior starts to change. We see that the transient oscillations are emphasized and the resonance voltages are significantly lowered as the resonance is reached already at $W^l = -W^r \approx 0.7$ for $U = 0.5$ and $W^l = -W^r \approx 0.6$ for $U = 1.0$. Furthermore, the I–V curve corresponding to $U = 1.0$ also develops an additional step structure for a narrow bias interval $W^l = -W^r \approx [0.55, 0.6]$. The shifting of the resonance in the current-

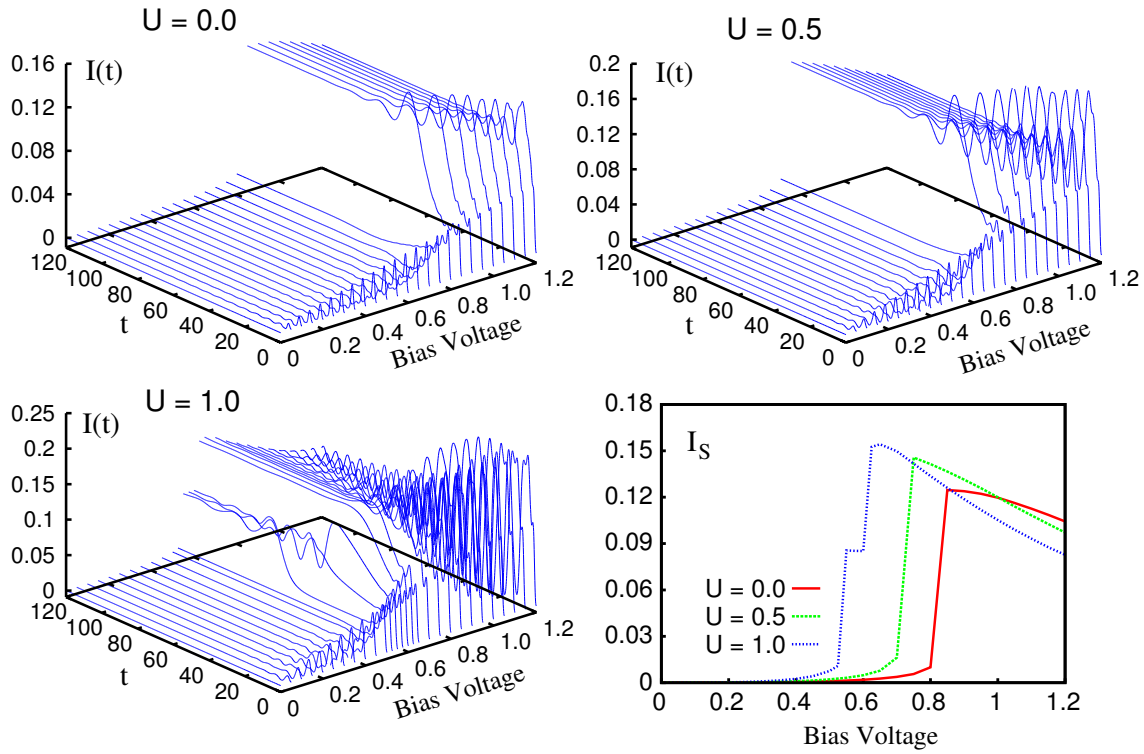

Figure 4.20: Time-dependent right current for HF appoximation for different molecule-lead interactions, $U = 0.0, 0.5$ and for $U = 1.0$. The bottom right panel shows the current-voltage characteristics corresponding to the 3D-plots.

voltage characteristics has its origin at an improved polarization of the molecular region for larger U. To support this statement, the Fig. 4.21 shows the individual transient currents and densities for the bias voltage 0.8 together with the ground state (GS) and non-equilibrium steady-state spectral functions. One can clearly see from the panel d) that the polarization increases drastically by increasing the interaction strength U. As we already know, this polarization (described by the relative occupations $n_H(t)$ and $n_L(t)$) leads to a HOMO-LUMO gap collapse (panel b) which then induces a significant increase in the current (panel a). For this model, one can approximate the positions of the HF resonances with the equations (see Eq. (4.1))

$$\begin{aligned} \epsilon_H^{\mathrm{HF}} &\approx h_{HH} + \Sigma_{HH}^{HF}, \\ &= \epsilon_H - 2U + U_0 n_H + 2U_{HL} n_L + 2U[n_{1r} + n_{1l}], \end{aligned} \tag{4.4}$$

$$\begin{aligned} \epsilon_L^{\mathrm{HF}} &\approx h_{LL} + \Sigma_{LL}^{HF}, \\ &= \epsilon_L - 2U + U_0 n_L + 2U_{HL} n_H + 2U[n_{1r} + n_{1l}], \end{aligned} \tag{4.5}$$

which agree very well the observed spectral peak positions of panel b) when evaluated using the densities of panel c) and d) together with the parameters for the interaction

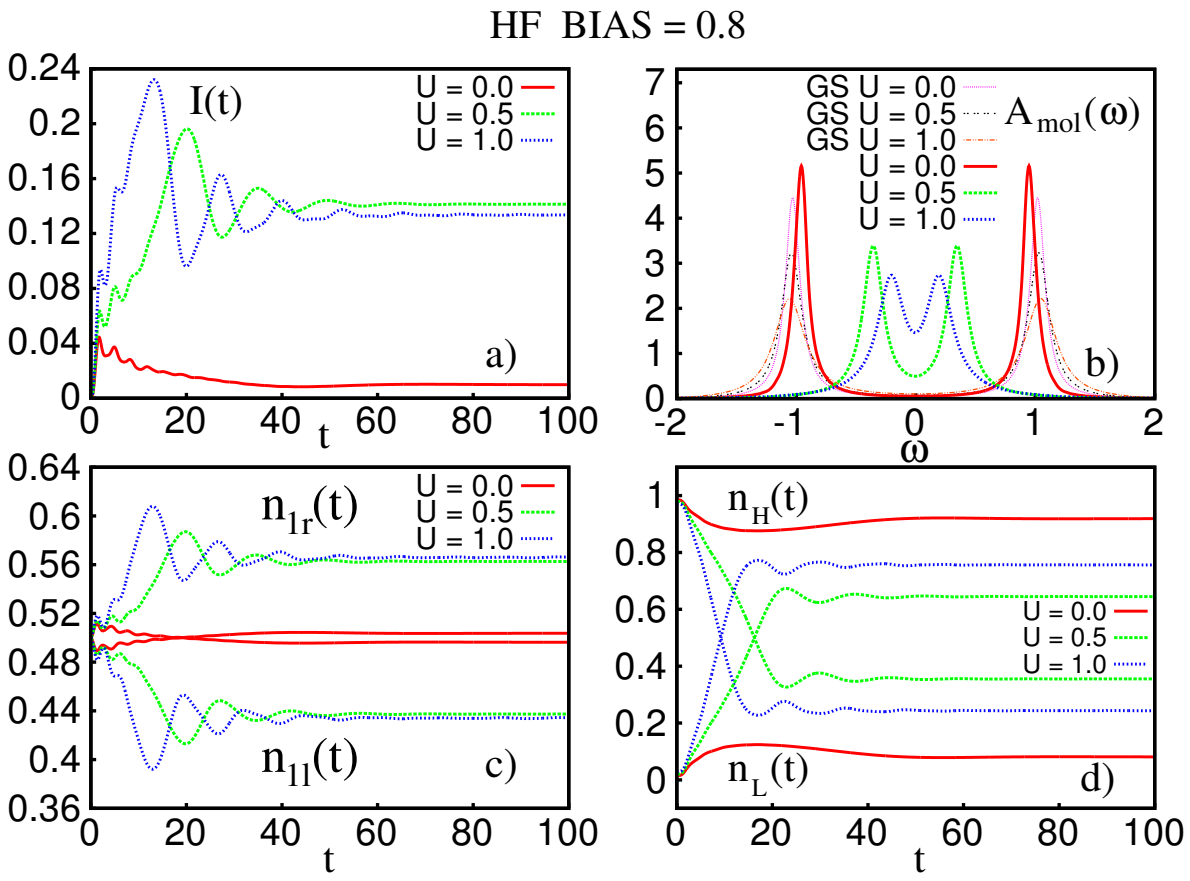

Figure 4.21: Time-dependent right currents (panel a), terminal site densities (panel c) and HOMO, LUMO densities (panel d) for HF approximation with $U = 0.0, 0.5$ and for $U = 1.0$. The panel b) shows the ground state (GS) and non-equilibrium steady-state spectral functions.

matrix elements.

The additional step in the I–V curve has also very interesting origin. For the bias voltages corresponding to the narrow step-like region, the molecule acquires excess charge during the charging phase, see Fig. 4.22. This excess charge induces Hartree potentials to the terminal sites of the leads which then temporarily block the current flow and a metastable step-structure is formed into the current-voltage characteristics. Increasing the bias voltage, a maximal current flow is then retained and the metastable state vanishes.

The resonance shifting and the formation of this metastable region are not the only peculiar properties that can be observed for the mean-field HF approximation. In fact, longer time-propagation reveals that for the bias voltages larger than the metastable biases, the system does not even reach a steady state. We demonstrate this property in Fig. 4.23 for the bias voltage $W^l = -W^r = 0.8$ by propagating the system up to 350 a.u.t. We see that for short propagation times the system seems to settle down do a

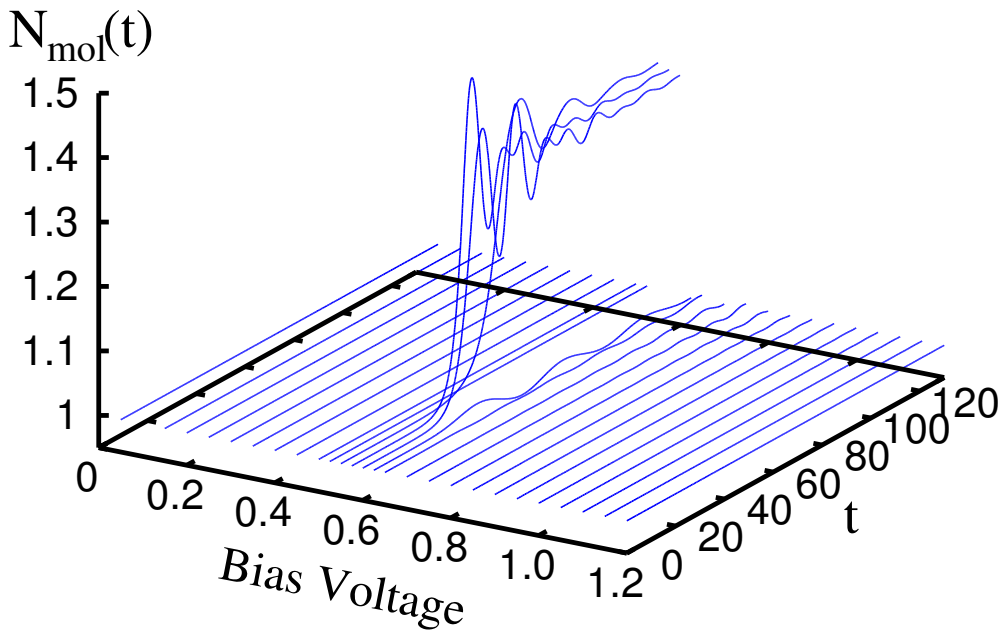

Figure 4.22: Time-dependent occupation in the molecular region, $N_{\rm mol}(t) = n_H(t) + n_L(t)$, as a function of the bias voltage. The molecule gains excess charge for the bias region $W^l = -U_R \in [0.55, 0.6]$ which causes a temporary blocking of the current.

well-defined steady state. However, the switch-on process induces time-dependent oscillations into the system which are kept alive and nourished by the finite bias voltage and the mean-field Coulomb effects. These oscillations develop in time and the system end up into an oscillatory state where the currents and densities oscillate dramatically around their average non-equilibrium values. The panel b) of Fig. 4.23 also shows the Fourier transform of the total current $|I_{\rm tot}(\omega)| = |I_l(\omega) + I_r(\omega)|$. The Fourier spectrum shows peaks at the odd multiples of the main frequency region which mainly corresponds to the electronic transitions between the dynamically renormalized molecular levels.

The formation of the metastable current region is sensitive not only to the molecule-lead Coulomb interaction but also to the hybridization strength $V^{l,r}$. The figure 4.24 shows for $V^{l,r} = -0.3$ how the metastable bias region extends to relative large bias regime $W^l = -W^r \in [0.425, 0.7]$ and the system becomes unstable for the larger bias voltages. One can therefore conclude that the formation of the metastable region is actually governed by the renormalization effect of the embedding self-energy due to the molecule-lead Coulomb interaction. In fact, the same phenomenon can drive the

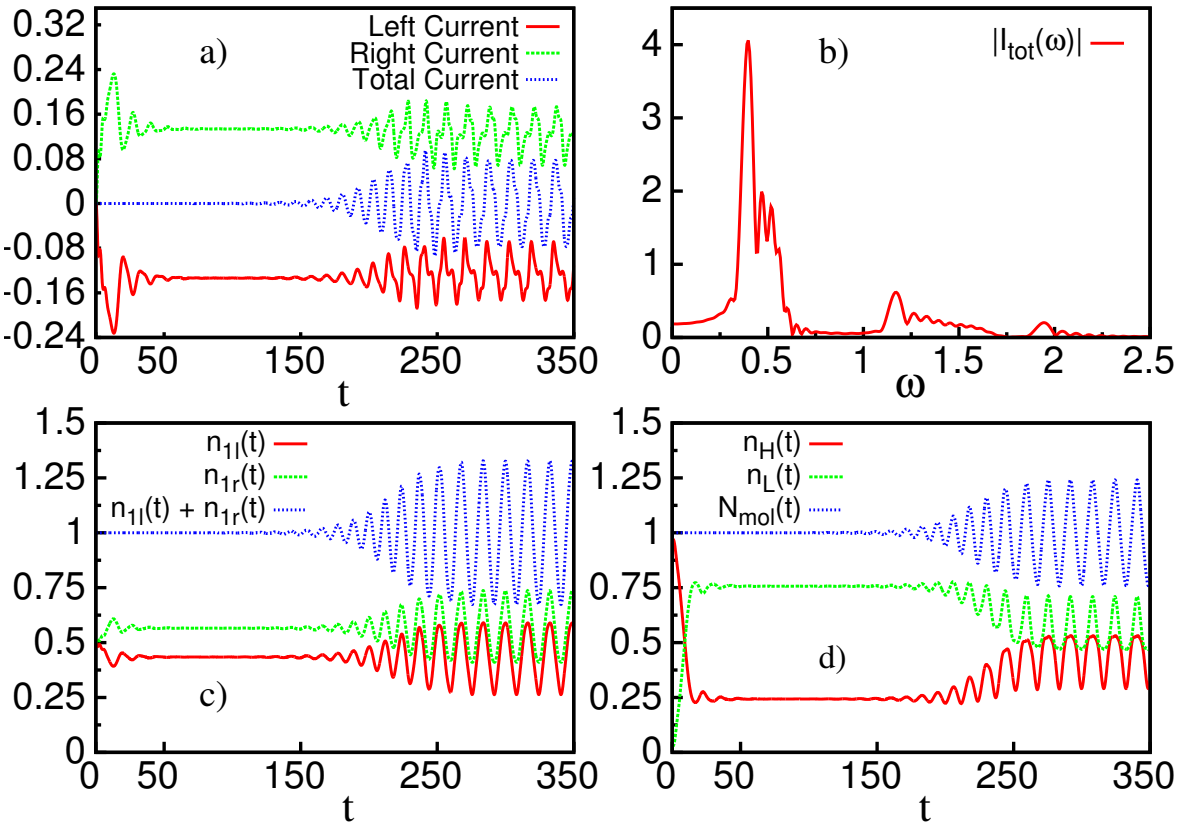

Figure 4.23: The unstable behavior of HF approximation. a) Time-dependent currents, c) terminal site densities, d) HOMO-LUMO densities. Panel b) contains the Fourier transform of the total current of panel a). The lead-molecule interaction $U = 1.0$ and $W^l = -W^r = 0.8$.

system to non-stationary solutions observed with larger bias voltages: the density matrices $G_{1H/L}$ and $G_{H/L1}$ become highly oscillatory functions which leads to *dynamical renormalization* of the embedding self-energy as the prefactor of Σ_{em} (see Eq. (4.3)) or, equivalently, the effective coupling matrix elements $V_{\text{eff}}(t) = V + U\rho_{H/L,1}(t)$ oscillates in time. The result is a strongly oscillating, self-consistent and self-sustaining non-stationary solution for the currents and densities.

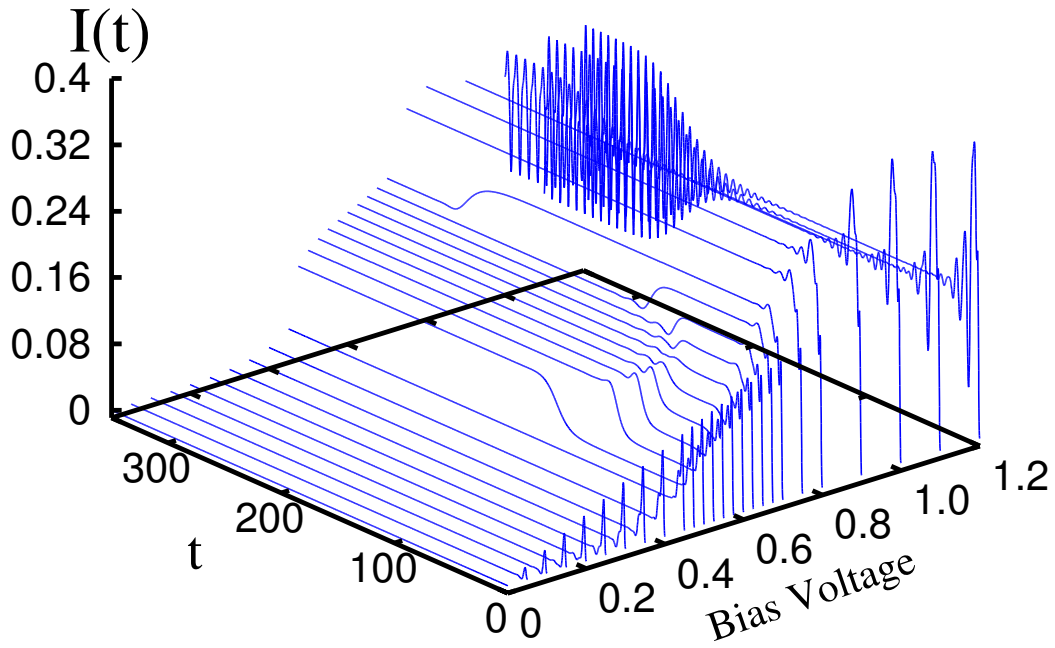

Figure 4.24: Time-dependent right currents as a function of bias voltage for HF approximation with $V^l = V^r = -0.3$ and $U = 1.0$.

4.3.3 Transients and steady-state properties: correlated approximations

Let us next investigate how the transport properties change if we account for the correlation-induced effects via the self-energy. The Figs. 4.25 and 4.26 shows now the transient right currents and I–V characteristics for 2B and GW approximation with different lead-molecule Coulomb interactions. As expected, the correlated approximations produce much less oscillatory currents with a stable steady-state due to the enhanced spectral broadening. This is something that one would expect from the basis of earlier analysis since the higher order self-energy diagrams provide substantial dissipation to the system which fights back the self-nourishing oscillations arising from the mean-field effects. Furthermore, just like for the HF approximation, the resonance voltages are clearly shifted towards smaller bias voltages since both the 2B and GW approximations contain the singular HF part in the self-energies. This shifting of the resonance is however accented by the image charge effect which closes the equilibrium gap (see Fig. 4.17) and redistributes the spectral weight between the main quasiparticle peaks and the satellite spectra arising from the leads. One can also observe that the sharp

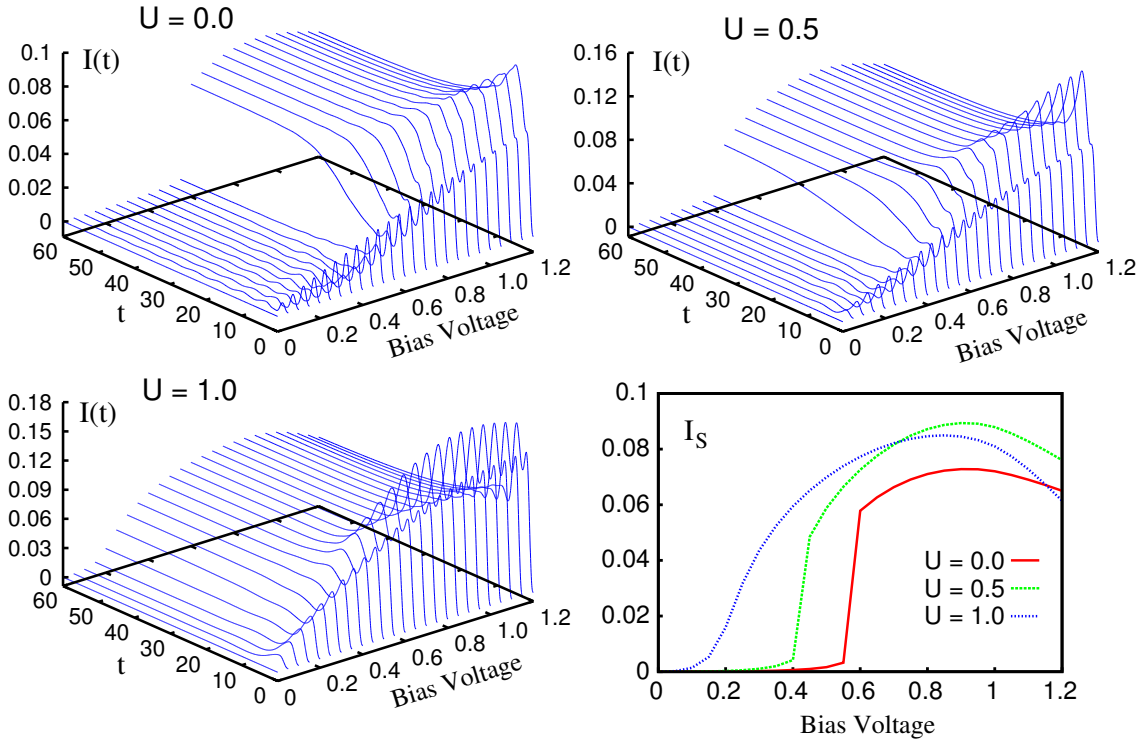

Figure 4.25: Time-dependent right current for 2B approximation for different molecule-lead interactions, $U = 0.0, 0.5$ and for $U = 1.0$. The bottom right panel shows the current-voltage characteristics corresponding to the 3D-plots.

jump of the current at the resonance is smeared out as the lead-molecule interaction is increased and that the metastable region is completely absent in the I–V curves. These features are clear evidences of the interplay of image charge effect together with the bias dependent gap closing mechanism discussed earlier. The bias dependent closing and image charge effect spread the spectral weight of the main peaks and the sharp jump in the I–V washes out.

As the final comparison, the Fig. 4.27 shows the non-equilibrium steady-state spectral functions $A(\omega, W^l)$ of the whole interacting region corresponding to the left panels of figures 4.20, 4.25 and 4.26. The left panels of Fig. 4.27 are obtained for the molecule-lead interaction $U = 0$ and the right panels correspond to $U = 1.0$. From this figure one can obtain a clear picture how the lead interaction effects change the non-equilibrium spectral properties. Let us first focus on the HF spectrum. The comparison of the left and right panels for HF shows immediately that the spectral structure is significantly transformed in the metastable bias region as the main spectral peaks are pushed down in energy and also two sharp edges are formed at the edges of the lead continua. These two edges are the manifestations of the Hartree-potentials at the terminal sites of the

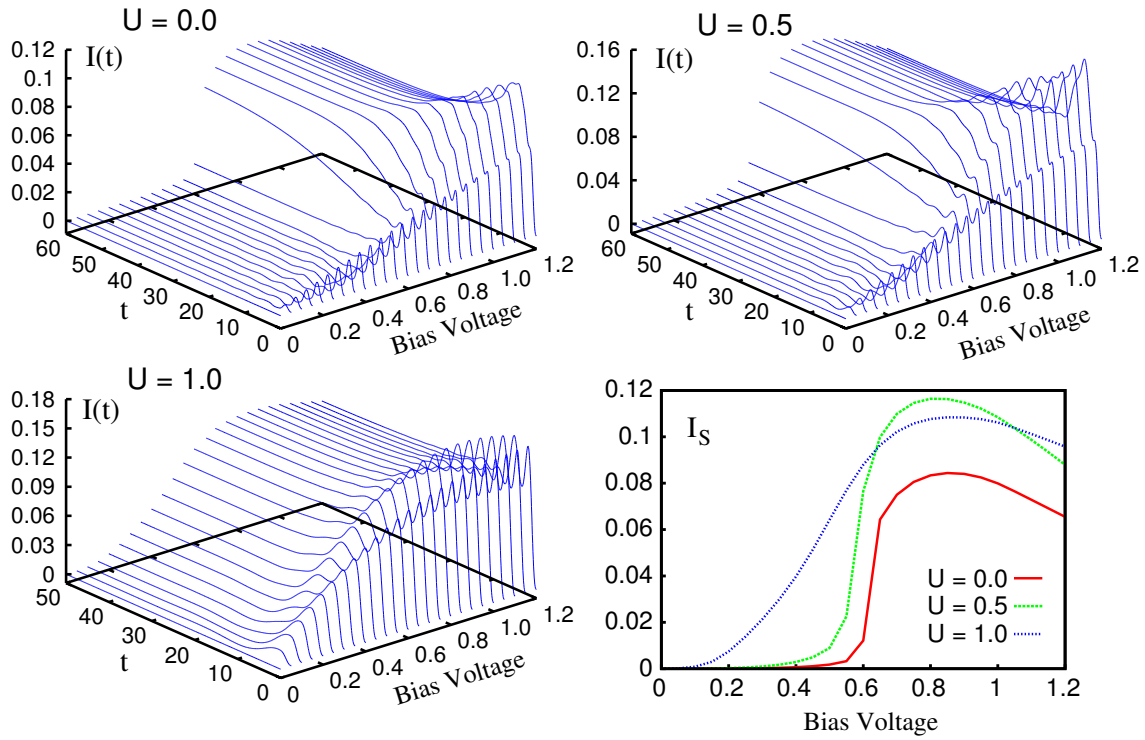

Figure 4.26: Time-dependent right current for GW appoximation for different molecule-lead interactions, $U = 0.0, 0.5$ and for $U = 1.0$. The bottom right panel shows the current-voltage characteristics corresponding to the 3D-plots.

leads when the molecular region is filled with an excess charge and it is also this charge gain that pushes the main peaks to lower frequencies, out of the bias window and partially blocking the current flow. For larger biases the gap narrows drastically and the peaks sharpen which is consistent with the strong temporal current oscillations.

The correlated spectral functions show also very interesting behavior. For $U = 0$ the gap collapse broadens the HOMO and LUMO spectral peaks to flat distribution over the whole energy continuum $[W^r - 2|b^\lambda|, W^l + 2|b^\lambda|]$. For $U = 1.0$ the situation is different and the spectral features remain relatively sharp for the whole bias voltage region. One can also see that for 2B approximation, the molecular gap is actually opening up rather than closing while the GW peak positions are not altered significantly. We can therefore say that the interaction between the molecule and the lead in a correlated level can have an opposite effect to the non-equilibrium spectral properties than the interactions restricted to the molecular region only.

The above results summarize the essential content of research article [3]. In conclusion, we investigated the mechanism how the molecule-lead interactions can renor-

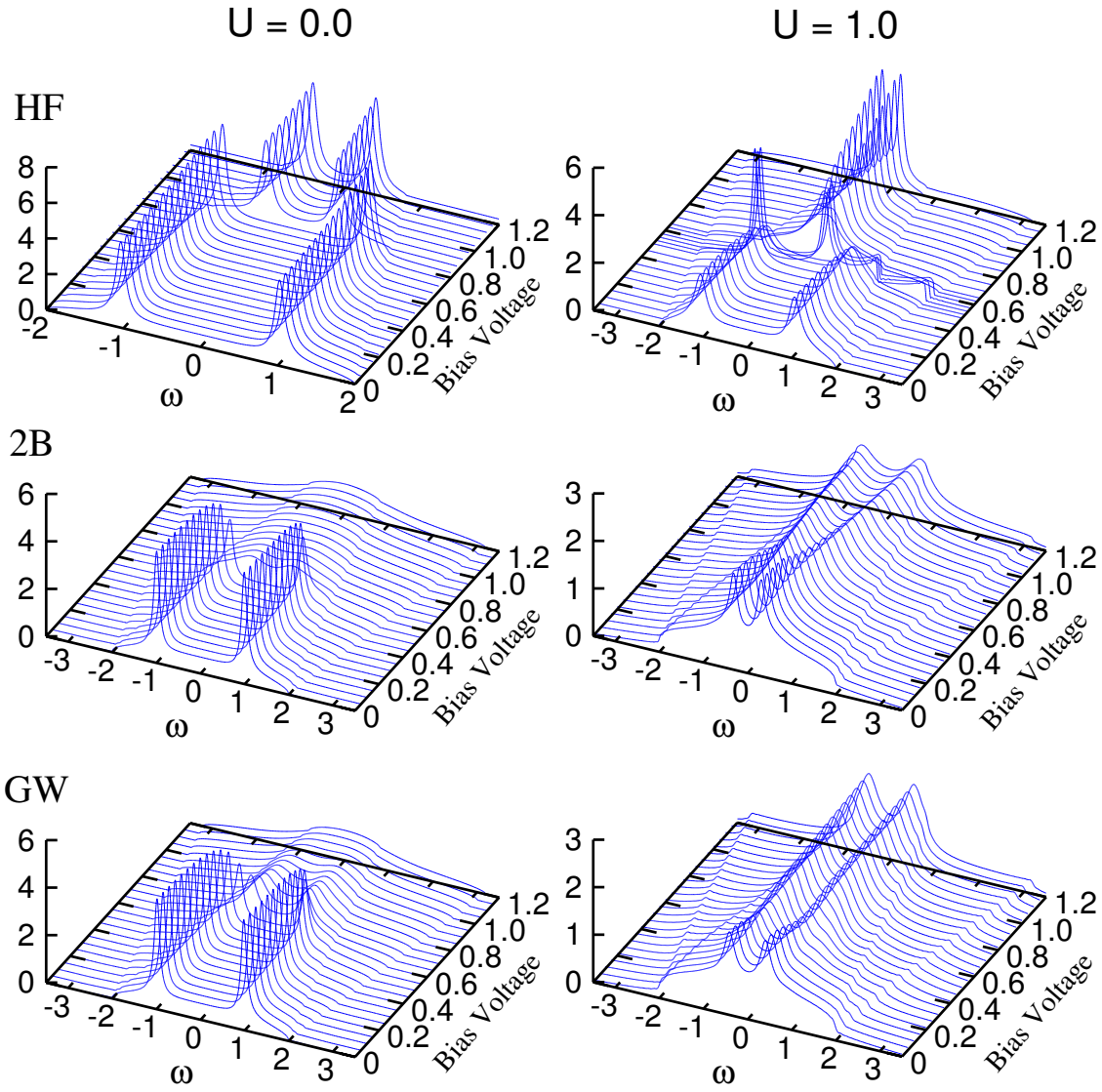

Figure 4.27: The non-equilibrium steady-state spectral functions $A(\omega, W^l) = \sum_i A_{ii}(\omega, W^l)$ ($i = 1l, H, L, 1r$.) for $U = 0.0$ (left panels) and for $U = 1.0$ (right panels) with different self-energy approximations corresponding to figures 4.20, 4.25 and 4.26.

malize the lead-molecule hybridizations and the whole embedding self-energy. In the HF level, this has profound consequences on ground-state, non-equilibrium the steady-state and transient properties of the system when driven out of equilibrium with a bias voltages. Firstly, the renormalization of the embedding can lead to nontrivial dynamical effects such as current blockage and undamped post-transient dynamics where the system does not reach a steady-state. These peculiarities can be cured by treating the e–e interactions within 2B or GW level which dynamically accounts for the important image charge effects, *i.e.*, the gap closing and satellite spectra, and also the bias dependent

gap closing mechanism. Interestingly, the molecule-lead interactions, when treated on a correlated level, can retain the sharp features of the non-equilibrium spectral functions.

4.4 AC transport

AC driven systems are the basic building blocks for modern day electronics. The application of AC perturbations to nanoscale systems offers a whole new playground for simulating the current and density responses of lead-molecule-lead junctions to alternating external fields. The Kadanoff-Baym formalism offers a natural framework to study this problem as the treatment of general time-dependent fields requires the same computational cost as the sudden-switches of time-independent biases or gate voltages.

In the journal article [4] we scratched the surface of this topic by briefly studying the AC-Bias response of a quantum wire connected to one-dimensional leads. The essential content of this article can be summarized as follows: By applying either symmetrical or asymmetrical AC bias voltages, the currents, densities and dipole moments generate very high level harmonics of the basic driving frequency ω_0 of the external time-dependent AC bias voltage. One can also, by using anti-symmetrical fields, selectively generate only the odd higher harmonic frequencies $(2n+1)\omega_0$ up to $n = 9$ which is very far from the linear response regime. By introducing an external AC bias that break the antisymmetry, also the even harmonics $2n\omega_0$ can be observed. We also found that the generated harmonics are emphasized around the energies corresponding to the average HOMO-LUMO transitions and also the electronic transitions between the molecular levels and the biased Fermi levels of the leads. This implies that one can, also in the case of AC fields, find fingerprints of the underlying spectral structure of the molecular region and the electronic transitions from the measured transient AC current. In this case, the HOMO and LUMO energy levels are also dynamically renormalized due to the alternating bias voltage, *i.e.*, the positions of the molecular levels depend on the phase of the bias voltage.

5 Summary & Outlook

Simulations are an essential part of research. They support experiments by providing a well-defined and controlled environment to reproduce the measured physics and, in many cases, predicting new phenomena which may have not been yet realized experimentally. In this sense quantum transport, as a relatively new and important branch of nanoscience, is an ideal playground for both the experiments and theory. Whenever one deals with systems the dynamics of which is determined by quantum mechanics, one ends up working with quantum transport process. Actually, every measurement, whether it is subjected to quantum mechanical, mesoscopic or even macroscopic systems, leads to a process where an external measurement apparatus is interacting with the test subject and, one way or another, induces charge and/or energy transfer processes in the subsystems. From this point of view, understanding the charge transport processes, and especially quantum transport processes is of utmost importance for all the fields within nanoscience. The work presented in this thesis has taken one step further in understanding the basic principles of quantum transport through small molecular-like structures where the electronic interactions have a significant role. Let us briefly summarize the topics covered in this work.

In this thesis I have given an overview of the NEGF formalism and derived the quantum kinetic equations of motion, the Kadanoff-Baym equations, for the one-particle Green function. This powerful formalism was then applied to open systems and extended via a projection technique to account for arbitrary number of electron reservoirs to yield *embedded Kadanoff-Baym equations*. This set of equations, consisting of the equation for the initial state, *i.e.*, the Dyson equation, and the set of real-time equations were then numerically solved for the molecular quantum systems coupled to source and sink terminals. For the interacting model Hamiltonian we adopted the PPP description suitable for the low-energy properties of conjugated hydrocarbons while the electron reservoirs were modeled as one -and two-dimensional semi-infinite tight binding leads. Within this model, we then calculated the current and density responses of the system to applied bias voltages.

Our results suggest that the electron-electron interactions, and especially the electron correlation effects beyond the mean-field, play a leading role in both the time-dependent and steady-state transport properties of the metal-molecule-metal junctions. In non-equilibrium situations when the interacting scattering region is subjected to current flow from source to sink terminal, the Coulomb interactions can give rise to a substantial renormalization of the molecular levels and also of the molecular gap.

This has profound consequences on both time-dependent and steady-state conductivity properties of these junctions. From the steady-state point of view, the interactions can lead to dramatic shifts and broadening of the conductance peaks and, on a mean-field level, can introduce anomalous step-structures to the current–voltage characteristics. These anomalous step-structures can be identified as situations where the current is temporarily and partially blocked.

From the transient point of view, the mean-field treatment of interactions can lead to overestimation of the transient features. The HF treatment of the Coulomb interactions lacks dissipative effects and this is reflected in the transient currents and densities which remain highly oscillatory during the whole transient time. These oscillations reflect the electronic transitions between energy levels of the central molecular region and also between the central region and the electron reservoirs. In fact, the mean-field treatment of long-range Coulomb interactions between the molecular device and the source/sink terminals can lead to dynamics where the time-dependent currents and densities do not reach a steady-state. This kind of dynamics is a prime example of the instantaneous nature of HF potential which neglects the history dependence. In contrast to the mean-field dynamics, the electron correlation effects on 2B or GW level account for these important memory effects which repress the overestimated transient features originating from the mean-field treatment.

The results reported in this thesis and in our research articles also suggest that the transient features are also sensitive to the initial conditions, *i.e.*, to the initial state which corresponds to the equilibrium solution provided by the Dyson equation. The Kadanoff-Baym formalism accounts this initial state dependence via the collision integrals where the non-local self-energy act as memory kernel to the initial state. Neglecting these memory terms can have a considerable effect on the transient dynamics especially under resonance conditions where the system can experience relatively long charging times. Our findings therefore advocates a proper treatment of the initial state and initial correlation terms during the time-evolution.

We have seen so far that the embedded Kadanoff-Baym equations offer a general, and flexible framework to deal with non-equilibrium quantum systems connected to electron reservoirs. This framework makes possible to study such a vast range of different topological systems driven with AC/DC perturbations that including them in one thesis is an impossible task. However, it is useful to point out the different applications which could be of great interest for the future research.

Apart from the AC biased systems, AC gated systems provide also an intriguing application for further research. For example, the implication of long-range electron correlation effects on phenomena such as photon assisted tunneling [94, 95] is still unexplored. The AC fields together with electron correlations could also be applied, for example, to electron pumping [96, 55] where an alternating time-dependent potential is used

to transport electron between source and drain electrodes. In addition to the research on AC fields, the extensions of transport topics involving spintronics, superconducting leads [97], shot noise [98], lead plasmons, Coulomb blockade and higher order tunneling processes, such as co-tunneling [99] to correlated time-dependent transport would offer challenging and interesting fields for future investigations with the real-time Kadanoff-Baym approach.

Appendix A: Embedded KB-equations

A.0.1 Embedding self-energy for two-dimensional semi-infinite TB lattice

The purpose of this appendix is to give an accurate description of the embedding self-energy for two-dimensional lattice. Let us go through in detail the derivation of article II Appendix B of this thesis.

Consider a two dimensional site lattice α with R_α rows and M_α columns, see Fig. (A.0.1). The tight-binding Hamiltonian for this system reads

$$\hat{H} = \sum_{IJ}^{R_\alpha} \sum_{ij}^{M_\alpha} \left[\mathbf{h}_\alpha\right]_{Ii,Jj} \hat{c}^\dagger_{Ii\alpha} \hat{c}_{Jj\alpha} - \mu \hat{N}_\alpha \tag{A.1}$$

where I, J (and also other capital indices in α-domain) runs through the rows and i, j (and other small indices in α-domain) runs through the columns of the site lattice. Thus the index pairs Ii and Jj comprises the spatial coordinates of the sites in the two-dimensional lattice. Here h^{ij}_{IJ} describes the nearest neighbor hoppings of electrons from site to another both in horizontal and vertical directions. The matrix elements of the Hamiltonian (A.1) can further be separated as independent components depending on the spatial direction:

$$\left[\mathbf{h}_\alpha\right]_{Ii,Jj} = \left[\mathbf{h}^\lambda_\alpha\right]_{ij} \delta_{IJ} + \left[\mathbf{h}^\tau_\alpha\right]_{IJ} \delta_{ij} \tag{A.2}$$

where $\mathbf{h}^\lambda_\alpha$ and $\mathbf{h}^\tau$ are the longitudinal (λ) and transverse (τ) hopping matrices with the matrix elements

$$\left[\mathbf{h}^\lambda_\alpha\right]_{ij} = \begin{cases} a_\alpha & i = j \\ b^\lambda_\alpha & i, j \text{ nearest neighbours} \\ 0 & \text{otherwise} \end{cases}$$
$$\left[\mathbf{h}^\tau_\alpha\right]_{IJ} = \begin{cases} b^\tau_\alpha & I, J \text{ nearest neighbours} \\ 0 & \text{otherwise} \end{cases} \tag{A.3}$$

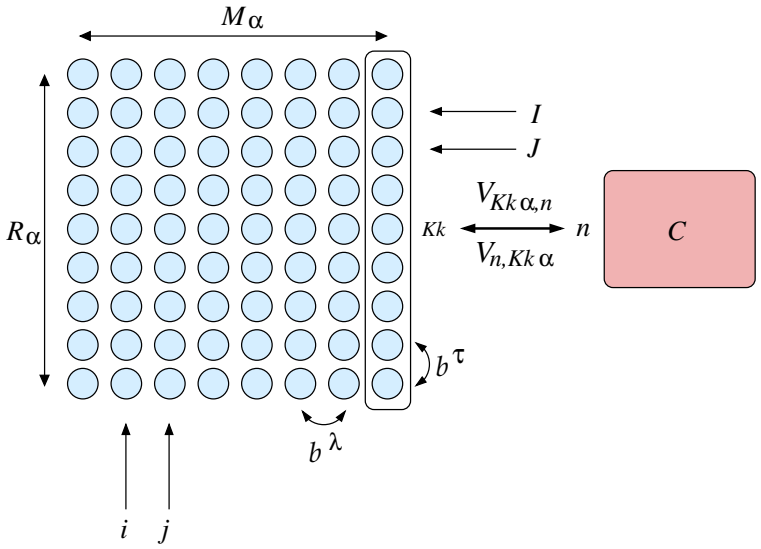

Figure A.1: Two-dimensional tight binding site lattice for lead α with R_α rows and M_α columns.

Hereby the Hamiltonian (A.1) becomes

$$\hat{H} = \sum_{I}^{R_\alpha}\sum_{ij}^{M_\alpha}\left[\mathbf{h}_\alpha^\lambda\right]_{ij}\hat{c}_{Ii\alpha}^\dagger\hat{c}_{Ij\alpha} + \sum_{i}^{M_\alpha}\sum_{IJ}^{R_\alpha}\left[\mathbf{h}_\alpha^\tau\right]_{IJ}\hat{c}_{Ii\alpha}^\dagger\hat{c}_{Ji\alpha} - \mu\hat{N}_\alpha \tag{A.4}$$

Since the Hamiltonian is separable, the single-particle eigenvalues of (A.4) are given by the sum of longitudinal and transverse channel eigenvalues, $\epsilon_{k\alpha}^\lambda$ and $\epsilon_{K\alpha}^\tau$, where k enumerates the orbitals in longitudinal direction and K in transverse direction. Furthermore, the eigenfunctions are product functions of the corresponding channel eigenfunctions, *i.e.*, the eigenfunctions of $\mathbf{h}_\alpha^\lambda$ and $\mathbf{h}_\alpha^\tau$.

Our aim is to calculate the noninteracting Green function and the embedding self-energy in the localized site basis for the two-dimensional lattice. For this purpose, let us expand the Fermionic field operators of the domain α using the localized site orbitals as

$$\hat{\psi}_\alpha(\mathbf{x}) = \sum_{Jj}\varphi_{Jj\alpha}(\mathbf{x})\hat{c}_{Jj\alpha} \tag{A.5}$$

$$\hat{\psi}_\alpha^\dagger(\mathbf{x}) = \sum_{Jj}\varphi_{Jj\alpha}^*(\mathbf{x})\hat{c}_{Jj\alpha}^\dagger, \tag{A.6}$$

where $\varphi_{Jj\alpha}(\mathbf{x})$ is the localized orbital at site coordinate Jj. Let us then consider the basis transformation from the localized site basis to the nonlocal orbital basis spanned by the wave functions $\chi_{Kk\alpha}(\mathbf{x})$

$$\chi_{Kk\alpha}(\mathbf{x}) = \sum_{Ii}\left[\mathbf{U}_\alpha^\tau\right]_{IK}\left[\mathbf{U}_\alpha^\lambda\right]_{ik}\varphi_{Ii\alpha}(\mathbf{x}) \tag{A.7}$$

or inversely

$$\varphi_{Ii\alpha}(\mathbf{x}) = \sum_{Kk} \left[\mathbf{U}_\alpha^{\tau,\dagger}\right]_{KI} \left[\mathbf{U}_\alpha^{\lambda,\dagger}\right]_{ki} \chi_{Kk\alpha}(\mathbf{x}). \tag{A.8}$$

Here $\chi_{Kk\alpha}(\mathbf{x})$ is the delocalized orbital corresponding to the transverse and longitudinal eigenvalues $\epsilon_{K\alpha}^{\tau}$ and $\epsilon_{k\alpha}^{\lambda}$ and $\mathbf{U}_\alpha^{\tau}$ and $\mathbf{U}_\alpha^{\lambda}$ are unitary basis transformation matrices which diagonalize the separate Hamiltonians

$$\begin{aligned} \left[\mathbf{U}_\alpha^{\lambda}\mathbf{h}_\alpha^{\lambda}\mathbf{U}_\alpha^{\lambda,\dagger}\right]_{kl} &= \epsilon_{k\alpha}^{\lambda}\,\delta_{k,l} \\ \left[\mathbf{U}_\alpha^{\tau}\mathbf{h}_\alpha^{\tau}\mathbf{U}_\alpha^{\tau,\dagger}\right]_{KL} &= \epsilon_{K\alpha}^{\tau}\,\delta_{K,L} \end{aligned} \tag{A.9}$$

$$\begin{aligned} \mathbf{U}_\alpha^{\lambda,\dagger}\mathbf{U}_\alpha^{\lambda} = \mathbf{U}_\alpha^{\lambda}\mathbf{U}_\alpha^{\lambda,\dagger} &= \mathbf{1}_{M_\alpha\times M_\alpha} \\ \mathbf{U}_\alpha^{\tau,\dagger}\mathbf{U}_\alpha^{\tau} = \mathbf{U}_\alpha^{\tau}\mathbf{U}_\alpha^{\tau,\dagger} &= \mathbf{1}_{R_\alpha\times R_\alpha} \end{aligned}$$

Inserting (A.8) into (A.5) and (A.6) it immediately follows that the Fermionic operators transform as

$$\begin{aligned} \hat{c}_{Ii\alpha} &= \sum_{k,K}^{M_\alpha,R_\alpha} [\mathbf{U}_\alpha^{\tau}]_{IK}[\mathbf{U}_\alpha^{\lambda}]_{ik}\,\hat{a}_{Kk\alpha}, \\ \hat{c}_{Ii\alpha}^{\dagger} &= \sum_{l,L}^{M_\alpha,R_\alpha} [\mathbf{U}_\alpha^{\tau}]_{IL}^{*}[\mathbf{U}_\alpha^{\lambda}]_{il}^{*}\,\hat{a}_{Ll\alpha}^{\dagger}, \end{aligned} \tag{A.10}$$

where $\hat{a}_{Ll\alpha}^{\dagger}$ and $\hat{a}_{Kk\alpha}$ are the Fermionic creation and annihilation operators in the delocalized basis obeying $\{\hat{a}_{Kk\alpha}, \hat{a}_{Ll\alpha}^{\dagger}\} = \delta_{KL}\delta_{kl}$ and $\{\hat{a}_{Kk\alpha}, \hat{a}_{Ll\alpha}\} = \{\hat{a}_{Kk\alpha}^{\dagger}, \hat{a}_{Ll\alpha}^{\dagger}\} = 0$.

Now, by using the notation in Eq. (A.10) for the Fermionic opertors, we can write the embedding self-energy for the lead α as

$$\left[\mathbf{\Sigma}_{\mathrm{em},\alpha}\right]_{mn}(z,z') = \sum_{IJkl} V_{m,Ik\alpha}\,\left[\mathbf{g}_{\alpha\alpha}\right]_{Ik,Jl}(z,z')\,V_{Jl\alpha,n}, \tag{A.11}$$

where the Green function for the lead α is given by

$$\begin{aligned} \left[\mathbf{g}_{\alpha\alpha}\right]_{Ik,Jl}(z,z') &= -i\left\langle \mathscr{T}_C\left[\hat{c}_{Ik\alpha,H}(z)\hat{c}_{Jl\alpha,H}^{\dagger}(z')\right]\right\rangle, \\ &= \sum_{ABcd} [\mathbf{U}_\alpha^{\tau}]_{IA}[\mathbf{U}_\alpha^{\lambda}]_{kc}\,[\hat{\mathbf{g}}_{\alpha\alpha}]_{Ac,Bd}(z,z')\,[\mathbf{U}_\alpha^{\lambda,\dagger}]_{dl}\,[\mathbf{U}_\alpha^{\tau,\dagger}]_{BJ}, \end{aligned} \tag{A.12}$$

with

$$\left[\hat{\mathbf{g}}_{\alpha\alpha}^{<}\right]_{Ac,Bd}(z,z') = i\delta_{AB}\delta_{cd} f(\epsilon_{Ac\alpha}) e^{-i\int_{z'}^{z}(\epsilon_{Ac\alpha}-\mu+W^{\alpha}(\tilde{z}))d\tilde{z}}, \tag{A.13}$$

$$\left[\hat{\mathbf{g}}_{\alpha\alpha}^{>}\right]_{Ac,Bd}(z,z') = i\delta_{AB}\delta_{cd}[f(\epsilon_{Ac\alpha})-1] e^{-i\int_{z'}^{z}(\epsilon_{Ac\alpha}-\mu+W^{\alpha}(\tilde{z}))d\tilde{z}}. \tag{A.14}$$

Here $f(\epsilon) = 1/(e^{\beta(\epsilon-\mu)}+1)$ is the Fermi-Dirac distribution function and $\epsilon_{Ac\alpha} = \epsilon^{\lambda}_{c\alpha} + \epsilon^{\tau}_{A\alpha}$, where

$$\epsilon^{\lambda}_{k\alpha} = a_\alpha - 2|b^{\lambda}_{\alpha}| \cos\left(\frac{k\pi}{M_\alpha+1}\right), \; k = 1, ..., M_\alpha, \tag{A.15}$$

$$\epsilon^{\tau}_{K\alpha} = -2|b^{\tau}_{\alpha}| \cos\left(\frac{K\pi}{R_\alpha+1}\right), \; K = 1, ..., R_\alpha, \tag{A.16}$$

Using this, we can write the lesser component of the self-energy in the following way

$$\begin{aligned}
&\left[\mathbf{\Sigma}^{<}_{\mathrm{em},\alpha}\right]_{mn}(z,z') \\
&= \sum_{IJAklc} V_{m,Ik\alpha}[\mathbf{U}^{\tau}_{\alpha}]_{IA}[\mathbf{U}^{\lambda}_{\alpha}]_{kc}\left\{if(\epsilon_{Ac\alpha})e^{-i\int_{z'}^{z}(\epsilon_{Ac\alpha}-\mu+W^{\alpha}(\tilde{z}))d\tilde{z}}\right\}[\mathbf{U}^{\lambda,\dagger}_{\alpha}]_{cl}[\mathbf{U}^{\tau,\dagger}_{\alpha}]_{AJ}V_{Jl\alpha,n} \\
&= \sum_{IJA}[\mathbf{U}^{\tau}_{\alpha}]_{IA}[\mathbf{U}^{\tau,\dagger}_{\alpha}]_{AJ}\, i\int \frac{d\epsilon}{2\pi} f(\epsilon)e^{-i\int_{z'}^{z}(\epsilon-\mu+W^{\alpha}(\tilde{z}))d\tilde{z}} \\
&\qquad\qquad \times \underbrace{\left\{2\pi\sum_{klc} V_{m,Ik\alpha}[\mathbf{U}^{\lambda}_{\alpha}]_{kc}\,\delta(\epsilon-\epsilon_{Ac\alpha})[\mathbf{U}^{\lambda,\dagger}_{\alpha}]_{cl}V_{Jl\alpha,n}\right\}}_{\Gamma^{IJA}_{mn,\alpha}(\epsilon-\epsilon_{A\alpha})} \\
&= ie^{-i\int_{z'}^{z}W^{\alpha}(\tilde{z})d\tilde{z}}\int\frac{d\epsilon}{2\pi}f(\epsilon)\underbrace{\left\{\sum_{IJA}[\mathbf{U}^{\tau}_{\alpha}]_{IA}[\mathbf{U}^{\tau,\dagger}_{\alpha}]_{AJ}\Gamma^{IJA}_{mn,\alpha}(\epsilon-\epsilon_{Ac\alpha})\right\}}_{[\mathbf{\Gamma}]_{mn,\alpha}(\epsilon)}e^{-i(\epsilon-\mu)(z-z')} \\
&= ie^{-i\int_{z'}^{z}W^{\alpha}(\tilde{z})d\tilde{z}}\int\frac{d\epsilon}{2\pi}f(\epsilon)[\mathbf{\Gamma}]_{mn,\alpha}(\epsilon)e^{-i(\epsilon-\mu)(z-z')}.
\end{aligned} \tag{A.17}$$

In the equation for $\Gamma^{IJA}_{mn,\alpha}(\epsilon-\epsilon_{A\alpha})$, the summation over the lead indices can be reduced if we consider the coupling matrices $V_{m,Ik\alpha}$ and $V_{Jl\alpha,n}$ to have nonzero elements only between the central region and the first layer of the two-dimensional lead α, *i.e.*, we set $k = l = 1$. Furthermore, by using the explicit expressions for the transformation matrix elements

$$\left[\mathbf{U}^{\lambda}_{\alpha}\right]_{kc} = \sqrt{\frac{2}{M_\alpha+1}}\sin\left(\frac{kc\pi}{M_\alpha+1}\right), \tag{A.18}$$

$$\left[\mathbf{U}^{\tau}_{\alpha}\right]_{IA} = \sqrt{\frac{2}{R_\alpha+1}}\sin\left(\frac{IA\pi}{R_\alpha+1}\right), \tag{A.19}$$

we then obtain

$$\begin{aligned}\Gamma^{IJA}_{mn,\alpha}(\epsilon-\epsilon_{A\alpha}) &= 2\pi V_{m,I1\alpha}V_{J1\alpha,n}\sum_{c=1}^{M_\alpha}[\mathbf{U}^{\lambda}_{\alpha}]_{1c}\delta(\epsilon-\epsilon_{Ac\alpha})[\mathbf{U}^{\lambda,\dagger}_{\alpha}]_{c1}\\ &= \frac{4\pi V_{m,I1\alpha}V_{J1\alpha,n}}{M_\alpha+1}\sum_{c=1}^{M_\alpha}\sin^2\left(\frac{c\pi}{M_\alpha+1}\right)\delta(\epsilon-\epsilon_{Ac\alpha})\\ &\rightarrow \frac{4\pi V_{m,I1\alpha}V_{J1\alpha,n}}{M_\alpha+1}\int_1^{M_\alpha}\sin^2\left(\frac{c\pi}{M_\alpha+1}\right)\delta(\epsilon-\epsilon_{Ac\alpha})dc\end{aligned} \tag{A.20}$$

where $\epsilon_{Ac\alpha}=\epsilon^{\lambda}_{c\alpha}+\epsilon^{\tau}_{A\alpha}$ and in the last step we consider the continuum limit as M_α becomes large. The integral can now be easily evaluated by changing the variables to $y=-2|b^{\lambda}_{\alpha}|\cos\left(\frac{c\pi}{M_\alpha+1}\right)$, which in the limit $M_\alpha\rightarrow\infty$ gives the integration limits from $-2|b^{\lambda}_{\alpha}|$ to $2|b^{\lambda}_{\alpha}|$. We then have

$$\begin{aligned}\Gamma^{IJA}_{mn,\alpha}(\epsilon-\epsilon_{A\alpha}) &= \frac{4\pi V_{m,I1\alpha}V_{J1\alpha,n}}{M_\alpha+1}\int_1^{M_\alpha}\sin^2\left(\frac{c\pi}{M_\alpha+1}\right)\delta(\epsilon-\epsilon_{Ac\alpha})dc\\ &= \frac{2V_{m,I1\alpha}V_{J1\alpha,n}}{|b^{\lambda}_{\alpha}|}\int_{-2|b^{\lambda}_{\alpha}|}^{2|b^{\lambda}_{\alpha}|}\sqrt{1-\frac{y^2}{4|b^{\lambda}_{\alpha}|^2}}\,\delta(\epsilon-a_\alpha-\epsilon^{\tau}_{A\alpha}-y)dy\\ &= \frac{2V_{m,I1\alpha}V_{J1\alpha,n}}{|b^{\lambda}_{\alpha}|}\sqrt{1-\frac{\hat{E}^2}{2|b^{\lambda}_{\alpha}|^2}}\,\Theta(2|b^{\lambda}_{\alpha}|-|\hat{E}|)\end{aligned} \tag{A.21}$$

where $\hat{E}=\epsilon-a_\alpha-\epsilon^{\tau}_{A\alpha}$ and $\epsilon^{\tau}_{A\alpha}=-2|b^{\tau}_{\alpha}|\cos\left(\frac{A\pi}{R_\alpha+1}\right), A=1...R_\alpha$.

The lesser component for the embedding self-energy for two-dimensional semi-infinite lead α is then finally given by

(2D)
$$\begin{aligned}\left[\mathbf{\Sigma}^{<}_{\mathrm{em},\alpha}\right]_{mn}(z,z') = i\frac{e^{-i\int_{z'}^{z}W^{\alpha}(\tilde{z})d\tilde{z}}}{|b^{\lambda}_{\alpha}|\pi}\sum_{IJA}^{R_\alpha}V_{m,I1\alpha}[\mathbf{U}^{\tau}_{\alpha}]_{IA}[\mathbf{U}^{\tau,\dagger}_{\alpha}]_{AJ}V_{J1\alpha,n}\\ \times\int_{a_\alpha+\epsilon^{\tau}_{A\alpha}-2|b^{\lambda}_{\alpha}|}^{a_\alpha+\epsilon^{\tau}_{A\alpha}+2|b^{\lambda}_{\alpha}|}f(\epsilon)\sqrt{1-\frac{(\epsilon-a_\alpha-\epsilon_{A\alpha})^2}{4|b^{\lambda}_{\alpha}|^2}}e^{-i(\epsilon-\mu)(z-z')}d\epsilon,\end{aligned} \tag{A.22}$$

and in the case of one-dimensional semi-infinite lead, the self-energy simplifies to

(1D)
$$\begin{aligned}\left[\mathbf{\Sigma}^{<}_{\mathrm{em},\alpha}\right]_{mn}(z,z') &= i\frac{e^{-i\int_{z'}^{z}W^{\alpha}(\tilde{z})d\tilde{z}}}{|b^{\lambda}_{\alpha}|\pi}V_{m,1\alpha}V_{1\alpha,n}\\ &\times\int_{a_\alpha-2|b^{\lambda}_{\alpha}|}^{a_\alpha+2|b^{\lambda}_{\alpha}|}f(\epsilon)\sqrt{1-\frac{(\epsilon-a_\alpha)^2}{4|b^{\lambda}_{\alpha}|^2}}e^{-i(\epsilon-\mu)(z-z')}d\epsilon.\end{aligned} \tag{A.23}$$

The greater component of the embedding self-energy, $\mathbf{\Sigma}^{>}_{\mathrm{em},\alpha}(z,z')$, can be obtained by simply replacing the Fermi function $f(\epsilon)$ with $f(\epsilon)-1$. Also the other components $(\rceil, \lceil, M)$ follow by considering the time-indices on the different domains on the Keldysh contour.

A.0.2 Meir-Wingreen formula from the time-dependent current expression

In the equation for the time-dependent current (3.84), let t grow until the initial correlation effects have died out. This means that

$$\mathbf{G}^{\rceil}(t,\bar{\tau})\mathbf{\Sigma}^{\lceil}_{\mathrm{em},\alpha}(\bar{\tau},t) \to 0 \quad t \text{ large.}$$

The resulting equation for the current will become

$$I_\alpha(t) = -2\,\mathrm{Re}\,\mathrm{Tr}\left\{\int_0^\infty d\bar{t}\left\{\mathbf{G}^{<}(t,\bar{t})\mathbf{\Sigma}^{A}_{\mathrm{em},\alpha}(\bar{t},t) + \mathbf{G}^{R}(t,\bar{t})\mathbf{\Sigma}^{<}_{\mathrm{em},\alpha}(\bar{t},t)\right\}\right\}. \tag{A.24}$$

Here all the matrices are in the central region indices and the trace is taken over this domain. Let us assume that in this limit, the Green function and the embedding self-energy depend only on the time-differences, that is

$$\begin{aligned}
\mathbf{G}^{<}(t,\bar{t}) &= \mathbf{G}^{<}(t-\bar{t}),\\
\mathbf{\Sigma}^{A}_{\mathrm{em},\alpha}(\bar{t},t) &= \mathbf{\Sigma}^{A}_{\mathrm{em},\alpha}(\bar{t}-t),\\
\mathbf{G}^{R}(t,\bar{t}) &= \mathbf{G}^{R}(t-\bar{t}),\\
\mathbf{\Sigma}^{<}_{\mathrm{em},\alpha}(\bar{t},t) &= \mathbf{\Sigma}^{<}_{\mathrm{em},\alpha}(\bar{t}-t).
\end{aligned}$$

Then we can express the above terms as a Fourier transformation, for example

$$\mathbf{G}^{<}(t-\bar{t}) = \int_{-\infty}^{\infty}\frac{d\omega}{2\pi}e^{-i\omega(t-\bar{t})}\mathbf{G}^{<}(\omega). \tag{A.25}$$

The equation for the current can then be written as

$$\begin{aligned}
I_\alpha(t) = -2\,\mathrm{Re}\,\mathrm{Tr}\Bigg\{&\int_0^\infty d\bar{t}\int_{-\infty}^{\infty}\frac{d\omega}{2\pi}e^{-i\omega(t-\bar{t})}\,\mathbf{G}^{<}(\omega)\int_{-\infty}^{\infty}\frac{d\tilde{\omega}}{2\pi}e^{-i\tilde{\omega}(\bar{t}-t)}\,\mathbf{\Sigma}^{A}_{\mathrm{em},\alpha}(\tilde{\omega})\\
&+\int_{-\infty}^{\infty}\frac{d\omega}{2\pi}e^{-i\omega(t-\bar{t})}\,\mathbf{G}^{R}(\omega)\int_{-\infty}^{\infty}\frac{d\tilde{\omega}}{2\pi}e^{-i\tilde{\omega}(\bar{t}-t)}\,\mathbf{\Sigma}^{<}_{\mathrm{em},\alpha}(\tilde{\omega})\Bigg\}.
\end{aligned} \tag{A.26}$$

Changing the time-integration variable from $\bar{t}$ to relative time-coordinate τ as $t-\bar{t}=\tau$ we have

$$\begin{aligned} I_\alpha(t) &= -2\,\mathrm{Re}\,\mathrm{Tr}\Bigg\{\int_{-\infty}^{t} d\tau \int_{-\infty}^{\infty}\frac{d\omega}{2\pi}e^{-i\omega\tau}\,\mathbf{G}^{<}(\omega)\int_{-\infty}^{\infty}\frac{d\tilde{\omega}}{2\pi}e^{i\tilde{\omega}\tau}\,\mathbf{\Sigma}^{A}_{\alpha,\mathrm{em}}(\tilde{\omega}) \\ &\quad + \int_{-\infty}^{\infty}\frac{d\omega}{2\pi}e^{-i\omega\tau}\,\mathbf{G}^{R}(\omega)\int_{-\infty}^{\infty}\frac{d\tilde{\omega}}{2\pi}e^{i\tilde{\omega}\tau}\,\mathbf{\Sigma}^{<}_{\mathrm{em},\alpha}(\tilde{\omega})\Bigg\}. \end{aligned} \tag{A.27}$$

Let now t go to infinity and let us denote the steady state current as I^S_α. Furthermore, by rearranging the integration variables and combining τ -dependent exponentials to the right under the time-integral we get

$$\begin{aligned} I^S_\alpha &= -2\,\mathrm{Re}\,\mathrm{Tr}\Bigg\{\int_{-\infty}^{\infty}\frac{d\omega}{2\pi}\mathbf{G}^{<}(\omega)\int_{-\infty}^{\infty}\frac{d\tilde{\omega}}{2\pi}\mathbf{\Sigma}^{A}_{\mathrm{em},\alpha}(\tilde{\omega})\underbrace{\int_{-\infty}^{\infty}d\tau e^{-i(\omega-\tilde{\omega})\tau}}_{2\pi\delta(\omega-\tilde{\omega})}+ \\ &\qquad \int_{-\infty}^{\infty}\frac{d\omega}{2\pi}\mathbf{G}^{R}(\omega)\int_{-\infty}^{\infty}\frac{d\tilde{\omega}}{2\pi}\mathbf{\Sigma}^{<}_{\mathrm{em},\alpha}(\tilde{\omega})\underbrace{\int_{-\infty}^{\infty}d\tau e^{-i(\omega-\tilde{\omega})\tau}}_{2\pi\delta(\omega-\tilde{\omega})}\Bigg\}, \\ &= -2\,\mathrm{Re}\,\mathrm{Tr}\Bigg\{\int_{-\infty}^{\infty}\frac{d\omega}{2\pi}\mathbf{G}^{<}(\omega)\mathbf{\Sigma}^{A}_{\mathrm{em},\alpha}(\omega)+\mathbf{G}^{R}(\omega)\mathbf{\Sigma}^{<}_{\mathrm{em},\alpha}(\omega)\Bigg\}. \end{aligned} \tag{A.28}$$

The symmetry relation of the Green function,

$$\left[\mathbf{G}^{<}(t-t')\right]^{\dagger}=-\mathbf{G}^{<}(t'-t), \tag{A.29}$$

directly implies that

$$\Big[\mathbf{G}^{<}(\omega)\Big]^{\dagger} = -\mathbf{G}^{<}(\omega), \tag{A.30}$$

Using this with the expressions for the embedding self-energy and retarded Green function

$$\begin{aligned} \mathbf{\Sigma}^{A}_{\mathrm{em},\alpha}(\omega) &= \mathbf{\Lambda}_\alpha(\omega)+\frac{i}{2}\mathbf{\Gamma}^{\alpha}(\omega), \\ \mathbf{\Sigma}^{<}_{\mathrm{em},\alpha}(\omega) &= i f_\alpha(\omega)\mathbf{\Gamma}^{\alpha}(\omega), \\ \\ \mathrm{Re}\Big[i\mathbf{G}^{R}(\omega)\Big] &= \frac{i}{2}\Big[\mathbf{G}^{R}(\omega)-\mathbf{G}^{A}(\omega)\Big], \end{aligned} \tag{A.31}$$

where $\mathbf{\Lambda}(\omega)$ and $\mathbf{\Gamma}(\omega)$ are real matrices and $f_\alpha(\omega) = f(\omega + U_\alpha)$, we have

$$\begin{aligned}
\mathrm{Re}\,\mathrm{Tr}\left[\mathbf{G}^<(\omega)\mathbf{\Sigma}^A_{\mathrm{em},\alpha}(\omega)\right] &= \frac{1}{2}\mathrm{Tr}\left[\mathbf{G}^<(\omega)\mathbf{\Sigma}^A_{\mathrm{em},\alpha}(\omega) + \left\{\mathbf{G}^<(\omega)\mathbf{\Sigma}^A_{\mathrm{em},\alpha}(\omega)\right\}^\dagger\right], \\
&= \frac{i}{2}\mathrm{Tr}\left[\mathbf{G}^<(\omega)\mathbf{\Gamma}^\alpha(\omega)\right], \\
\mathrm{Re}\,\mathrm{Tr}\left[\mathbf{G}^R(\omega)\mathbf{\Sigma}^<_{\mathrm{em},\alpha}(\omega)\right] &= \frac{i}{2}\mathrm{Tr}\left[\left\{\mathbf{G}^R(\omega) - \mathbf{G}^A(\omega)\right\} f_\alpha(\omega)\mathbf{\Gamma}^\alpha(\omega)\right],
\end{aligned}$$

and the steady-state current through the interacting-noninteracting interface α will then become

$$I^S_\alpha = -i\,\mathrm{Tr}\left\{\int_{-\infty}^{\infty}\frac{d\omega}{2\pi}\mathbf{\Gamma}^\alpha(\omega)\left\{\mathbf{G}^<(\omega) + f_\alpha(\omega)\left[\mathbf{G}^R(\omega) - \mathbf{G}^A(\omega)\right]\right\}\right\}, \quad \text{(A.32)}$$

or equivalently

$$I^S_\alpha = -i\,\mathrm{Tr}\left\{\int_{-\infty}^{\infty}\frac{d\omega}{2\pi}\mathbf{\Gamma}^\alpha(\omega)\left\{\mathbf{G}^<(\omega) - 2\pi i f_\alpha(\omega)\mathbf{A}(\omega)\right\}\right\}. \quad \text{(A.33)}$$

To summarize, the terms appearing in the previous equations were given by:

$$\begin{aligned}
\mathbf{G}^{R(A)}(\omega) &= \frac{1}{(\omega \pm i\eta)\mathbf{1} - \mathbf{h}_C - \mathbf{\Sigma}^{R(A)}(\omega)}, \\
\mathbf{\Sigma}^{R(A)}(\omega) &= \mathbf{\Sigma}^{R(A)}_{\mathrm{MB}}(\omega) + \sum_\alpha \mathbf{\Sigma}^{R(A)}_{\mathrm{em},\alpha}(\omega), \\
\mathbf{\Sigma}^{R(A)}_{\mathrm{em},\alpha}(\omega) &= \mathbf{\Lambda}_\alpha(\omega) \mp \frac{i}{2}\mathbf{\Gamma}_\alpha(\omega), \\
\mathbf{\Lambda}_\alpha(\omega) &= \mathscr{P}\int\frac{d\omega'}{2\pi}\frac{\mathbf{\Gamma}_\alpha(\omega')}{\omega - \omega'}, \\
\mathbf{\Gamma}_\alpha(\omega) &= \mathbf{h}_{C\alpha}\mathbf{h}_{\alpha C}\,\frac{2}{|b|}\sqrt{1 - \left(\frac{\tilde{E}}{2b}\right)^2}\,\Theta(2|b| - \tilde{E}), \\
\mathbf{\Sigma}^<_{\mathrm{em},\alpha}(\omega) &= i f_\alpha(\omega)\mathbf{\Gamma}_\alpha(\omega), \\
\mathbf{\Sigma}^>_{\mathrm{em},\alpha}(\omega) &= i(f_\alpha(\omega) - 1)\mathbf{\Gamma}_\alpha(\omega),
\end{aligned}$$

where $\tilde{E} = \omega - a_\alpha - U_\alpha$ (1D).

References

[1] P. Myöhänen, A. Stan, G. Stefanucci and R. van Leeuwen. *A many-body approach to quantum transport dynamics: Initial correlations and memory effects*. Europhysics Letters **84**, 67001 (2008).

[2] P. Myöhänen, A. Stan, G. Stefanucci and R. van Leeuwen. *Kadanoff-Baym approach to quantum transport through interacting nanoscale systems: From the transient to the steady-state regime*. Phys. Rev. B **80**, 115107 (2009).

[3] P. Myöhänen, R. Tuovinen, T. Korhonen, G. Stefanucci and R. van Leeuwen. *Image charge dynamics in time-dependent quantum transport*. Phys. Rev. B **85**, 075105 (2012).

[4] P. Myöhänen, A. Stan, G. Stefanucci and R. van Leeuwen. *Kadanoff-Baym approach to time-dependent quantum transport in AC and DC fields*. J. Phys.:Conf. Ser. **220**, 012017 (2010).

[5] R. P. Feynman. *There's Plenty Of Room At The Bottom*. Caltech Engineering and Science **23:5**, 22 (1960).

[6] T. A. Fulton and G. J. Dolan. *Observation of single-electron charging effects in small tunnel junctions*. Phys. Rev. Lett. **59**, 109 (1987).

[7] Y. Meir, N. S. Wingreen and P. A. Lee. *Transport through a strongly interacting electron system: Theory of periodic conductance oscillations*. Phys. Rev. Lett. **66**, 3048 (1991).

[8] M. A. Reed, C. Zhou, C. J. Muller, T. P. Burgin and J. M. Tour. *Conductance of a Molecular Junction*. Science **278**, 252 (1997).

[9] R. H. M. Smit, Y. Noat, C. Untiedt, N. D. Lang, M. C. van Hemert and J. M. van Ruitenbeek. *Measurement of the conductance of a hydrogen molecule*. Nature **419**, 906 (2002).

[10] Y. Okawa, S. K. Mandal, C. Hu, Y. Tateyama, S. Goedecker, S. Tsukamoto, T. Hasegawa, J. K. Gimzewski and M. Aono. *Chemical Wiring and Soldering toward All-Molecule Electronic Circuitry*. J. Am. Chem. Soc. **133**, 8227 (2011).

[11] H. Haug and A.-P. Jauho. *Quantum kinetics in transport and optics of semiconductors*. Springer, Heidelberg (1998).

[12] James D. Patterson and Bernard C. Bailey. *Solid-State Physics: Introduction to the Theory*. Springer, New York (2006).

[13] W. R. Frensley. *Boundary conditions for open quantum systems driven far from equilibrium*. Rev. Mod. Phys. **62**, 745 (1990).

[14] N. C. Kluksdahl, A. M. Kriman, D. K. Ferry and C. Ringhofer. *Self-consistent study of the resonant-tunneling diode*. Phys. Rev. B **39**, 7720 (1989).

[15] K. L. Jensen and F. A. Buot. *Numerical simulation of transient response and resonant-tunneling characteristics of double-barrier semiconductor structures as a function of experimental parameters*. J. Appl. Phys. **65**, 5248 (1989).

[16] J. Lin and L. C. Chiu. *Quantum theory of electron transport in the Wigner formalism*. J. Appl. Phys. **57**, 1373 (1985).

[17] P. Havu, N. Tuomisto, R. Väänänen, M. J. Puska, and R. M. Nieminen. *Spin-dependent electron transport through a magnetic resonant tunneling diode*. Phys. Rev. B **71**, 235301 (2005).

[18] P. Bordone, M. Pascoli, R. Brunetti, A. Bertoni, C. Jacoboni and A. Abramo. *Quantum transport of electrons in open nanostructures with the Wigner-function formalism*. Phys. Rev. B **59**, 3060 (1999).

[19] Guifré Vidal. *Efficient Simulation of One-Dimensional Quantum Many-Body Systems*. Phys. Rev. Lett. **93**, 040502 (2004).

[20] U. Schollwöck. *The density-matrix renormalization group*. Rev. Mod. Phys. **77**, 259 (2005).

[21] D. Bohr and P. Schmitteckert. *Strong enhancement of transport by interaction on contact links*. Phys. Rev. B **75**, 241103 (2007).

[22] A. Branschädel, G. Schneider and P. Schmitteckert. *Conductance of correlated systems: real-time dynamics in finite systems*. arXiv:1004.4178v1 [cond-mat.str-el] (2010).

[23] P. Schmitteckert. *Nonequilibrium electron transport using the density matrix renormalization group method*. Phys. Rev. B **70**, 121302 (2004).

[24] D. Bohr. *Quantum Transport in Strongly Correlated Systems: A Density Matrix Renormalization Group Study : Ph.D. Thesis*. MIC - Department of Micro and Nanotechnology, Technical University of Denmark (2007).

[25] S. Schmitt and F. B. Anders. *Comparison between scattering-states numerical renormalization group and the Kadanoff-Baym-Keldysh approach to quantum transport: Crossover from weak to strong correlations*. Phys. Rev. B **81**, 165106 (2010).

[26] J. K. Freericks, V. M. Turkowski and V. Zlatić. *Nonequilibrium Dynamical Mean-Field Theory*. Phys. Rev. Lett. **97**, 266408 (2006).

[27] P. Hohenberg and W. Kohn. *Inhomogeneous Electron Gas*. Phys. Rev. **136**, B864 (1964).

[28] W. Kohn and L. J. Sham. *Self-Consistent Equations Including Exchange and Correlation Effects*. Phys. Rev. **140**, A1133 (1965).

[29] U. von Barth. *Basic Density-Functional Theory - an Overview*. Phys. Scr. **T109**, 9 (2004).

[30] E. Runge and E. K. U. Gross. *Density-Functional Theory for Time-Dependent Systems*. Phys. Rev. Lett. **52**, 997 (1984).

[31] M. A. L. Marques, C. A. Ullrich, F. Nogueira, A. Rubio, K. Burke and E. K. U. Gross. *Time-dependent density functional theory: lecture notes in physics*. Springer, Heidelberg (2006).

[32] S. Kurth, G. Stefanucci, C.-O. Almbladh, A. Rubio, and E. K. U. Gross. *Time-dependent quantum transport: A practical scheme using density functional theory*. Phys. Rev. B **72**, 035308 (2005).

[33] X. Zheng, F. Wang, C. Y. Yam, Y. Mo and G. Chen. *Time-dependent density-functional theory for open systems*. Phys. Rev. B **75**, 195127 (2007).

[34] X. Zheng, G. Chen, Y. Mo, S. Koo, H. Tian, C. Yam and Y. Yan. *Time-dependent density functional theory for quantum transport*. J. Chem. Phys. **133**, 114101 (2010).

[35] S. Kurth, G. Stefanucci, E. Khosravi, C. Verdozzi and E. K. U. Gross. *Dynamical Coulomb Blockade and the Derivative Discontinuity of Time-Dependent Density Functional Theory*. Phys. Rev. Lett. **104**, 236801 (2010).

[36] J. S. Evans, O. A. Vydrov and T. Van Voorhis. *Exchange and correlation in molecular wire conductance: Nonlocality is the key*. J. Chem. Phys. **131**, 034106 (2009).

[37] J. S. Evans and T. Van Voorhis. *Dynamic Current Suppression and Gate Voltage Response in Metal-Molecule-Metal Junctions*. Nano Lett. **9(7)**, 2671 (2009).

[38] L. P. Kadanoff and G. Baym. *Quantum Statistical Mechanics*. Benjamin, New York (1962).

[39] A. L. Fetter and J.D. Walecka. *Quantum Theory of Many-Particle Systems*. McGraw-Hill, New York (1971).

[40] Y. Meir and N. Wingreen. *Landauer formula for the current through an interacting electron region*. Phys. Rev. Lett. **68**, 2512 (1992).

[41] J.Taylor, H. Guo and J. Wang. *Ab initio modeling of open systems: Charge transfer, electron conduction, and molecular switching of a C60 device*. Phys. Rev. B **63**, 121104 (2001).

[42] D. M. Cardamone, C. A. Stafford and S. Mazumdar. *Controlling Quantum Transport through a Single Molecule*. Nano Lett. **6(11)**, 2422 (2006).

[43] P. Darancet, A. Ferretti, D. Mayou and V. Olevano. *Ab initio GW electron-electron interaction effects in quantum transport*. Phys. Rev. B **75**, 075102 (2007).

[44] K. S. Thygesen. *Impact of Exchange-Correlation Effects on the IV Characteristics of a Molecular Junction*. Phys. Rev. Lett. **100**, 166804 (2008).

[45] K. Thygesen and A. Rubio. *Renormalization of Molecular Quasiparticle Levels at Metal-Molecule Interfaces: Trends across Binding Regimes*. Phys. Rev. Lett. **102**, 046802 (2009).

[46] A. Rubio J. M. Garcia-Lastra, C. Rostgaard and K. S. Thygesen. *Polarization-induced renormalization of molecular levels at metallic and semiconducting surfaces*. Phys. Rev. B **80**, 245427 (2009).

[47] K. S. Thygesen and A. Rubio. *Conserving GW scheme for nonequilibrium quantum transport in molecular contacts*. Phys. Rev. B **77**, 115333 (2008).

[48] J. P. Bergfield and C. A. Stafford. *Many-body theory of electronic transport in single-molecule heterojunctions*. Phys. Rev. B **79**, 245125 (2009).

[49] H. Ness, L. K. Dash and R. W. Godby. *Generalization and applicability of the Landauer formula for nonequilibrium current in the presence of interactions*. Phys. Rev. B **82**, 085426 (2010).

[50] A-P. Jauho, N. S. Wingreen and Y. Meir. *Time-dependent transport in interacting and noninteracting resonant-tunneling systems*. Phys. Rev. B **50**, 5528 (1994).

[51] G. Stefanucci and C.-O. Almbladh. *Time-dependent partition-free approach in resonant tunneling systems*. Phys. Rev. B **69**, 195318 (2004).

[52] A.-M. Uimonen, E. Khosravi, A. Stan, G. Stefanucci, S. Kurth, R. van Leeuwen and E. K. U. Gross. *Comparative Study of Many-Body Perturbation Theory and Time Dependent Density Functional Theory in the Out-of-Equilibrium Anderson Model*. Phys. Rev. B **84**, 115103 (2011).

[53] A.-M. Uimonen, E. Khosravi, G. Stefanucci, S. Kurth, R. van Leeuwen and E. K. U. Gross. *Real-Time Switching between Multiple Steady-States in Quantum Transport*. J. Phys.:Conf Ser. **220**, 012018 (2010).

[54] E. Khosravi, A.-M. Uimonen, A. Stan, G. Stefanucci, S. Kurth, R. van Leeuwen and E. K. U. Gross. *Correlation effects in Bistability at the Nanoscale: Steady State and Beyond*. Phys. Rev. B **85**, 075103 (2012).

[55] G. Stefanucci, S. Kurth, A. Rubio and E. K. U. Gross. *Time-dependent approach to electron pumping in open quantum systems*. Phys. Rev. B **77**, 075339 (2008).

[56] G. Stefanucci. *Bound states in ab initio approaches to quantum transport: A time-dependent formulation*. Phys. Rev. B **75**, 195115 (2007).

[57] S.-H. Ke, R. Liu, W. Yang and H. U. Baranger. *Time-dependent transport through molecular junctions*. J. Chem. Phys. **132**, 234105 (2010).

[58] E. C. Cuansing and G. Liang. *Time-dependent quantum transport and power-law decay of the transient current in a nano-relay and nano-oscillator*. J. App. Phys. **110**, 083704 (2011).

[59] D. Kienle, M. Vaidyanathan and F. Léonard. *Self-consistent ac quantum transport using nonequilibrium Green functions*. Phys. Rev. B **81**, 115455 (2010).

[60] V. Moldoveanu, V. Gudmundsson and A. Manolescu. *Nonadiabatic transport in a quantum dot turnstile*. Phys. Rev. B **76**, 165308 (2007).

[61] N. S. Wingreen, A-P. Jauho, and Y. Meir. *Time-dependent transport through a mesoscopic structure*. Phys. Rev. B **48**, 8487 (1993).

[62] M. Strange, C. Rostgaard, H. Häkkinen and K. S. Thygesen. *Self-consistent GW calculations of electronic transport in thiol- and amine-linked molecular junctions*. Phys. Rev. B **83**, 115108 (2011).

[63] M. Strange and K. S. Thygesen. *Towards quantitative accuracy in first-principles transport calculations: The GW method applied to alkane/gold junctions*. Beilstein J. Nanotechnol. **2**, 746 (2011).

[64] M. Brandbyge, J.-L. Mozos, P. Ordejón, J. Taylor and K. Stokbro. *Density-functional method for nonequilibrium electron transport*. Phys. Rev. B **65**, 165401 (2002).

[65] A. R. Rocha, V. M. García-Suárez, S. Bailey, C. Lambert, J. Ferrer and S. Sanvito. *Spin and molecular electronics in atomically generated orbital landscapes*. Phys. Rev. B **73**, 085414 (2006).

[66] M. Puig von Friesen, C. Verdozzi and C.-O. Almbladh. *Successes and Failures of Kadanoff-Baym Dynamics in Hubbard Nanoclusters*. Phys. Rev. Lett. **103**, 176404 (2009).

[67] M. Puig von Friesen, C. Verdozzi and C.-O. Almbladh. *Kadanoff-Baym dynamics of Hubbard clusters: Performance of many-body schemes, correlation-induced damping and multiple steady and quasi-steady states*. Phys. Rev. B **82**, 155108 (2010).

[68] M. Puig von Friesen, C. Verdozzi and C.-O. Almbladh. *Can we always get the entanglement entropy from the Kadanoff-Baym equations? The case of the T-matrix approximation*. Europhys. Lett. **95**, 27005 (2011).

[69] N. Säkkinen, M. Manninen and R. van Leeuwen. *The Kadanoff-Baym approach to double excitations in finite systems*. New Journal of Physics **14**, 013032 (2012).

[70] K. Balzer, M. Bonitz, R. van Leeuwen, A. Stan N and E. Dahlen. *Nonequilibrium Greens function approach to strongly correlated few-electron quantum dots*. Phys. Rev. B **79**, 245306 (2009).

[71] N. E. Dahlen and R. van Leeuwen. *Solving the Kadanoff-Baym Equations for Inhomogeneous Systems: Application to Atoms and Molecules*. Phys. Rev. Lett. **98**, 153004 (2007).

[72] A. Stan, N. E. Dahlen and R. van Leeuwen. *Fully self-consistent GW calculations for atoms and molecules*. Europhysics Letters **76**, 298 (2006).

[73] A. Stan, N. E. Dahlen and R. van Leeuwen. *Levels of self-consistency in the GW approximation*. J. Chem. Phys. **130**, 114105 (2009).

[74] K. Balzer. *Solving the Two-time Kadanoff-Baym Equations. Application to Model Atoms and Molecules. Ph.D Thesis*. University of Kiel (2011).

[75] G. Stefanucci and R. van Leeuwen. *Nonequilibrium Many-Body Theory and Keldysh Formalism - A Modern Introduction*. To be published (2012).

[76] P. Danielewicz. *Quantum Theory of Nonequilibrium Processes, I.* Ann. Phys. **152** (1984).

[77] V. M. Galitskii and A. B. Migdal. *Application of quantum field theory methods to the many body problem*. Sov. Phys., JETP **7**, 96 (1958).

[78] L. Hedin. *New Method for Calculating the One-Particle Green's Function with Application to the Electron-Gas Problem*. Physical Review **139** (1965).

[79] C. Friedrich and A. Schindlmayr. *Many-Body Perturbation Theory : The GW Approximation*. Computing **31**, 335 (2006).

[80] Gordon Baym. *Self-Consistent Approximations in Many-Body Systems*. Phys. Rev. **127**, 1391 (1962).

[81] J. M. Luttinger and J. C. Ward. *Ground-State Energy of a Many-Fermion System. II*. Physical Review **118**, 1417 (1960).

[82] R. Pariser and R. G. Parr. *A Semi-Empirical Theory of the Electronic Spectra and Electronic Structure of Complex Unsaturated Molecules. I.* J. Chem. Phys. **21**, 466 (1953).

[83] J. A. Pople. *Electron Interaction in Unsaturated Hydrocarbons*. Trans. Faraday Soc. **49**, 1375 (1953).

[84] N. E. Dahlen and R. van Leeuwen. *Self-consistent solution of the Dyson equation for atoms and molecules within a conserving approximation*. J. Chem. Phys. **122** (2005).

[85] A. Stan, N. E. Dahlen and R. van Leeuwen. *Time propagation of the Kadanoff-Baym equations for inhomogeneous systems*. J. Chem. Phys **130** (2009).

[86] D. C. Langreth. *Linear and nonlinear response theory with applications*. Plenum, New York (1976).

[87] J. Guojun. *Introduction to Condensed Matter Physics, Volume 1*. World Scientific, Singapore (2005).

[88] S. Kubatkin, A. Danilov, M. Hjort, J. Cornil, J. L. Bredas, N. Stuhr-Hansen, P. Hedegård and T. Bjørnholm. *Single-electron transistor of a single organic molecule with access to several redox states*. Nature **425**, 698 (2003).

[89] E. A. Osorio, K. O'Neill, N. Stuhr-Hansen, O. F. Nielsen, T. Bjørnholm and H. S. J. van der Zant. *Addition energies and vibrational fine structure measured in electromigrated single-molecule junctions based on an oligophenylenevinylene derivative*. Adv. Mater. **19**, 281 (2007).

[90] J. B. Neaton, M. S. Hybertsen and S. G. Louie. *Renormalization of Molecular Electronic Levels at Metal-Molecule Interfaces*. Phys. Rev. Lett. **97**, 216405 (2006).

[91] K. Kaasbjerg and K. Flensberg. *Strong Polarization-Induced Reduction of Addition Energies in Single-Molecule Nanojunctions*. Nano Lett. **8**, 3809 (2008).

[92] K. Kaasbjerg and K. Flensberg. *Image charge effects in single-molecule junctions: Breaking of symmetries and negative-differential resistance in a benzene single-electron transistor*. Phys. Rev. B **84**, 115457 (2011).

[93] P. Hedegård and T. Bjørnholm. *Charge transport through image charged stabilized states in a single molecule single electron transistor device*. Nano Lett. **319**, 350 (2005).

[94] L. P. Kouwenhoven, S. Jauhar, K. McCormick, D. Dixon, P. L. McEuen, Yu. V. Nazarov, N. C. van der Vaart and C. T. Foxon. *Photon–assisted tunneling through a quantum dot*. Phys. Rev. B **50**, 2019 (1994).

[95] L. P. Kouwenhoven, S. Jauhar, J. Orenstein, P. L. McEuen, Y. Nagamune, J. Motohisa and H. Sakaki. *Observation of Photon-Assisted Tunneling through a Quantum Dot*. Phys. Rev. Lett **73**, 3443 (1994).

[96] M. Switkes, C. M. Marcus, K. Campman and A. C. Gossard. *An Adiabatic Quantum Electron Pump*. Science **283**, 1905 (1999).

[97] G. Stefanucci, E. Perfetto and M. Cini. *Time-Dependent Quantum Transport with Superconducting Leads*. J. Phys.: Conf. Ser. **220**, 012012 (2010).

[98] Ya. M. Blanter and M. Buttiker. *Shot noise in mesoscopic conductors*. Phys. Rep. **336**, 1 (2000).

[99] S. De Franceschi, S. Sasaki, J. M. Elzerman, W. G. van der Wiel, S. Tarucha, and L. P. Kouwenhoven. *Electron Cotunneling in a Semiconductor Quantum Dot*. Phys. Rev. Lett. **86**, 878 (2001).